BIOINSPIRED SCATTERING MATERIALS: LIGHT TRANSPORT IN ANISOTROPIC, DISORDERED SYSTEMS

GIOVANNI IACUCCI
ST CATHARINE'S COLLEGE

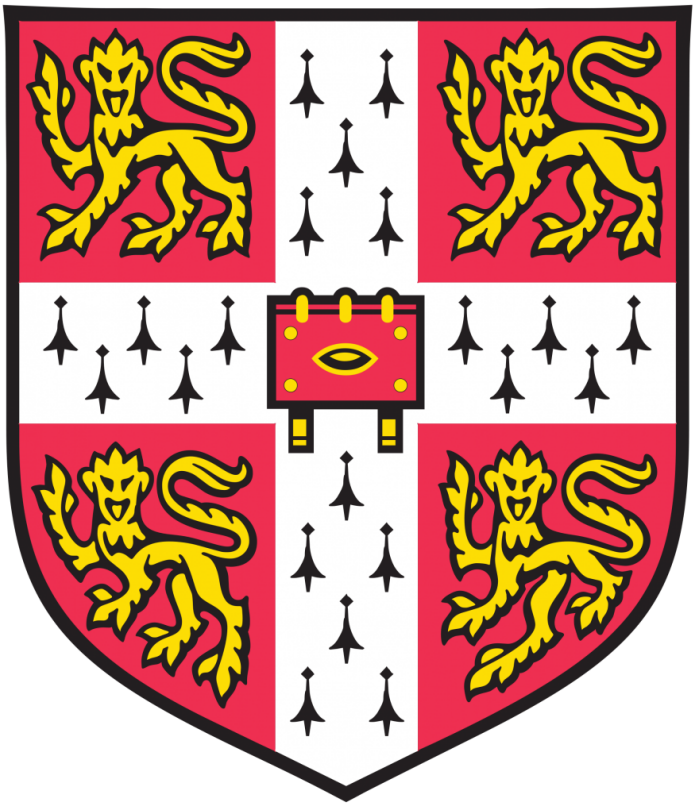

UNIVERSITY OF CAMBRIDGE
DEPARTMENT OF CHEMISTRY

This dissertation is submitted for the degree of Doctor of Philosophy

SUPERVISOR:

Dr. Silvia Vignolini

June 2020

Ad Andrea.
A Denis, attendendo giustizia.
A Giulio, Stefano, Gabbo, Federico, Carlo and to George.
To the real ones.

DECLARATION

I hereby declare that except where specific reference is made to the work of others, the contents of this dissertation are original and have not been submitted in whole or in part for consideration for any other degree or qualification in this, or any other university. This dissertation is my own work and contains nothing which is the outcome of work done in collaboration with others, except as specified in the text. This dissertation contains fewer than 60,000 words, including abstract, tables, and footnotes.

Cambridge, June 2020

Giovanni Iacucci

ABSTRACT

Bioinspired scattering materials: light transport in anisotropic, disordered systems.

Giovanni Iacucci.

The study of light propagation in disordered media has attracted the interest of many researchers for its relevance to fundamental and applied problems, ranging from imaging through turbid media to the fabrication of white paint. Scattering in a disordered system is determined by the spatial distribution and the scattering properties of its building blocks. To date, most efforts on scattering optimisation have focused on isotropic, high refractive index systems. This thesis investigates the importance of anisotropy in increasing the scattering efficiency of a system, with a particular focus on low refractive index media and their use as sustainable, white materials.

Nature provides a striking example of how to exploit anisotropy to achieve scattering optimisation: with the intra-scale chitin network of the beetle genus *Cyphochilus*. In this thesis, after showing that this network exhibits the highest scattering efficiency found in nature thus far, a systematic numerical investigation was performed to understand the importance of both single-particle and structural anisotropy in scattering optimisation. In particular, this numerical analysis unveiled that ensembles of anisotropic particles show higher reflectance compared to their isotropic counterpart, whilst using less material.

Based on these findings, the optical properties of bioinspired, scattering systems — obtained both via polymer phase separation and a combination of sequential vacuum filtration and freeze-drying — were investigated. Notably, the reported materials achieve scattering properties comparable to those found in nature, showcasing the potential of using biopolymers to produce sustainable, biocompatible white materials. In addition, the presented bioinspired systems are an interesting platform for fundamental studies, allowing to investigate light transport in anisotropic media.

CONTENTS

LIST OF FIGURES

LIST OF TABLES

LIST OF SYMBOLS AND ACRONYMS

In this thesis, scalars are indicated with a standard font (e.g., S), vectors in bold (e.g., $\mathbf{S}$) and matrices in calligraphy (e.g., $\mathcal{S}$).

Notation	Meaning
a^*, b^*	Polar coordinates of the CIELAB colour space
b	Optical thickness (in Subsection 1.3.1)
c	Aspect ratio
CBS	Coherent backscattering
CNC	Cellulose nanocrystals
CNF	Cellulose nanofibers
CNP	Cellulose nanoparticles
D	Diffusion constant
E	Enhancement of the coherent backscattering line shape
ff	Filling fraction
$F(\mathbf{k})$	Form factor
FTIR	Fourier transform infrared
g	Scattering asymmetry parameter
$G(\mathbf{k}, \mathbf{r})$	Green function
I	First component of the Stokes vector (intensity)
$\mathbf{k}$	Momentum
k	Wavenumber ($k = 2\pi/\lambda$)
L	Thickness of a sample
L^*	Axial coordinate of the CIELAB colour space
ℓ_a	Absorption mean free path
ℓ_s	Scattering mean free path
ℓ_t	Transport mean free path
ℓ_{xy}, ℓ_z	Components of the transport mean free path
$\mathcal{M}$	Mueller scattering matrix

MCC	Microcrystalline cellulose
M_w	Molecular weight (mass average molar mass)
N	Scattering order
n	Refractive index
n_e	Effective refractive index
n_p	Number density
OA	Optical anisotropy
OT	Optical thickness
$P(r)$	Step length probability distribution
$P_T(\mu)$	Angular distribution of transmitted light
$\langle P_2 \rangle$	Order parameter
PMMA	Polymethyl methacrylate
Q	Second component of the Stokes vector
Q_s	Scattering efficiency
$\mathbf{r}$	Position vector
r	Radius of a spherical particle
r_0	Radius at $c = 1$
$R(\theta)$	Polarisation-averaged Fresnel's coefficient
R	Polarisation- and angle-averaged Fresnel's coefficient
S	Scattering matrix (S-matrix)
$\mathbf{S}$	Stokes vector
$S(\mathbf{k})$	Structure factor
SEM	Scanning electron microscopy
SEC	Size exclusion chromatography
$T(L, \lambda)$	Total transmission
TEM	Transmission electron microscopy
U	Third component of the Stokes vector
V	Fourth component of the Stokes vector
w	Full widht half maximum of the coherent backscattering line shape
W	Whiteness
z_e	Extrapolation length

z_p	Penetration length
α_0	Polarisability
γ_c	Coherent contribution to the interference
γ_i	Incoherent contribution to the interference
ζ	Contrast of the two-wave interference pattern
λ	Wavelength
v_e	Energy velocity
ρ	Energy density
σ_g	Geometrical cross section
σ_s	Scattering cross section
ψ_0	Incident wave
ψ_s	Scattered wave
$\Delta\psi$	Angular distance between the first and last scattering event

LIST OF PUBLICATIONS

The work described in this thesis have been published as follows:

1. J. Syurik*, **G. Jacucci***, O. D. Onelli, H. Hölscher, and S. Vignolini. Bio-inspired Highly Scattering Networks via Polymer Phase Separation. *Advanced Functional Materials* **38** (2018).
2. **G. Jacucci**, O. D. Onelli, A. De Luca, J. Bertolotti, R. Sapienza, and Silvia Vignolini. Coherent backscattering of light by an anisotropic biological network. *Interface Focus* **9** (2019).
3. **G. Jacucci**, J. Bertolotti, S. Vignolini. Role of Anisotropy and Refractive Index in Scattering and Whiteness Optimization. *Advanced Optical Materials* **7** (2019).

In my PhD, I also contributed to the study and review of light propagation in disordered materials where the transport is not diffusive:

4. O. D. Onelli*, M. S. Toivonen*, **G. Jacucci**, V. Lovikka, O. J. Rojas, O. Ikkala, and S. Vignolini. Anomalous-Diffusion-Assisted Brightness in White Cellulose Nanofibril Membranes. *Advanced Materials* **30** (2018).
5. **G. Jacucci**, L. Schertel, Y. Zhang, H. Yang, S. Vignolini. Light management with natural materials: from whiteness to transparency. *Advanced Materials* (2020).

Finally, the concepts and methodologies developed in this thesis have been used to study the role of disorder on the optical properties of biological and artificial ordered systems:

6. D. P. Song, **G. Jacucci**, F. Dundar, A. Naik, H. F. Fei, S. Vignolini, and J. J. Watkins. Photonic Resins: Designing Optical Appearance via Block Copolymer Self-Assembly. *Macromolecules* **51** (2018).
7. K. Feller, D. Wilby, **G. Jacucci**, S. Vignolini, J. Mantell, T. J. Wardill, T. W. Cronin, N. W. Roberts. Long-Wavelength Reflecting Filters Found in the Larval Retinas of One Mantis Shrimp Family (*Nannosquillidae*). *Current Biology* **29** (2019).

8. C. L. C. Chan, M. M. Bay, **G. Jacucci**, R. Vadrucci, C. A. Williams, G. T. van de Kerkhof, R. M. Parker, K. Vynck, B. Frka-Petesic, S. Vignolini. Visual Appearance of Chiral Nematic Cellulose-Based Photonic Films: Angular and Polarization Independent Color Response with a Twist. *Advanced Materials* **31** (2019).
9. D. Wangpraseurt, S. You, F. Azam, **G. Jacucci**, O. Gaidarenko, M. Hildebrand, M. Kühl, A. G. Smith, M. P. Davey, A. Smith, D. D. Deheyn, S. Chen, S. Vignolini. Bionic 3D printed corals. *Nature Communications*, **11** (2020).
10. B. Frka-Petesic, J. A. Kelly, **G. Jacucci**, G. Guidetti, G. Kamita, N. P. Crossette, W. Y. Hamad, M. J. MacLachlan, S. Vignolini. Retrieving the Coassembly Pathway of Composite Cellulose Nanocrystal Photonic Films from their Angular Optical Response. *Advanced Materials* **32** (2020).
11. G. T. van de Kerkhof, L. Schertel, R. Poon, **G. Jacucci**, B. J. Glover, S. Vignolini. Disordered wax platelets on Tradescantia pallida leaves create golden shine. *Faraday Discussions* (2020).
12. Y. Chang, Y. Ogawa, **G. Jacucci**, O. D. Onelli, H. Tseng, S. Vignolini. Hereditary Character of Photonics Structure in Pachyrhynchus sarcitis Weevils: Color Changes via One Generation Hybridization. *Advanced Optical Materials* (2020).
13. L. Schertel, G. T. van de Kerkhof, **G. Jacucci**, L. Catón, Y. Ogawa, B. D. Wilts, C. J. Ingham, S. Vignolini, V. E. Johansen Complex photonic response reveals three-dimensional self-organization of structural coloured bacterial colonies. *Journal of the Royal Society Interface* **17** (2020).
14. R. Middleton, M. Sinnott-Armstrong, Y. Ogawa, **G. Jacucci**, E. Moyroud, P. J. Rudall, C. Prychid, M. Conejero, B. J. Glover, M. J. Donoghue, S. Vignolini. Viburnum tinus Fruits Use Lipids to Produce Metallic Blue Structural Color. *Current Biology* **30** (2020).
15. T. H. Zhao, **G. Jacucci**, X. Chen, D. P. Song, S. Vignolini, R. M. Parker. Angular Independent Photonic Pigments via the Controlled Micellization of Amphiphilic Bottlebrush Block Copolymers. *Advanced Materials* (2020).

16. **G. Jacucci**, S. Vignolini, L. Schertel. The limitations of extending nature's color palette in correlated, disordered systems. *PNAS* (2020).

    Note that the name I use in my publications (Gianni Jacucci) differs from my legal one (Giovanni Iacucci).

INTRODUCTION

The optical mechanism determining the visual appearance of non-absorbing media is *light scattering* [1–5]. This phenomenon occurs when light encounters refractive index inhomogeneities — referred to as scattering centres or scatterers — and it is responsible, for example, of the white colouration of clouds and foams [6].

In inhomogeneous materials scattering results from the interplay between (i) the *single-particle* properties, such as the geometrical characteristics and the refractive index of the scatterer; (ii) the *ensemble* properties, such as the filling fraction (i.e., the fraction of the total volume occupied by the scatterers), the average orientation of the scatterers, and the structure factor (i.e., the spatial organisation of the scatterers) [7–9].

The visual appearance of disordered systems, which is the main focus of this thesis, is directly determined by their *optical thickness* (OT). This parameter is defined as the ratio between the physical thickness of a medium and the *transport mean free path*, i.e., the average distance over which light "loses memory" of its initial direction [2–4]. Light transport can undergo different regimes when propagating in disordered media (Figure 1): from *ballistic propagation*, where most of the intensity is transmitted in the same direction as the incoming beam, to *multiple scattering*, where light is diffusely redistributed. In the ballistic regime, at low OT, light propagation is almost undisturbed, resulting in a transparent appearance resembling a homogeneous medium. In contrast, materials in the multiple scattering regime (OT > 8 [10–12]) are opaque white.

Maximising the scattering efficiency of a system, i.e., minimising the mean free path, is therefore of significant interest for the fabrication of every white product we use. The easiest, and arguably the most effective, approach to achieve a high scattering efficiency is to use high refractive index building blocks — as exploited in the industrial production of white materials. White products are obtained via empirically-optimised

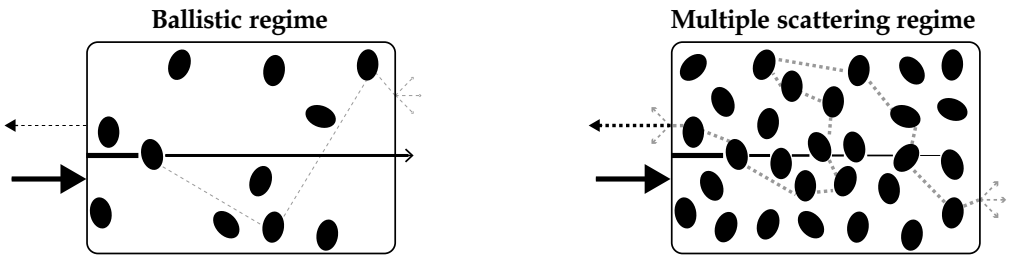

Single-particle properties: size; aspect ratio; refractive index
Ensemble properties: filling fraction; structure factor; average orientation
Legend: —— ballistic beam; ····· specular reflection; ····· scattered light

Figure 1 | Illustration of light propagation regimes in disordered media. For simplicity, the transition between different regimes is depicted by varying the filling fraction of the system. Ballistic beam, specular reflection and scattered light are represented by solid black, dotted black and dotted grey lines, respectively. Line thickness qualitatively represents the difference in intensity between ballistic and scattered light in every regime.

ensembles of titanium dioxide ($n \simeq 2.6$ [13]) spherical particles [14]. However, the intensive use of titanium dioxide has recently raised safety concerns [15, 16], highlighting the need for a biocompatible replacement.

The main challenge in replacing high refractive index materials is represented by the low refractive index of biocompatible alternatives ($n \simeq 1.5$ [17, 18]). This limitation forced biological systems to elaborate scattering designs beyond isotropic — both in terms of single-particle and ensemble properties — media. A prime example is the anisotropic arrangement of chitinous filaments in the scales of the *Cyphochilus* beetle affording brilliant whiteness [19–22].

Inspired by nature, this thesis investigates the importance of anisotropy in improving the scattering efficiency of low refractive index systems. The overall objective of this work is to identify the design principles enabling the replacement of commercially available white products with natural resources.

The work presented in this thesis is organised as follows:

- Part I , Theoretical framework and methodologies: in Chapter 1, the fundamental concepts of light propagation in disordered media are introduced. The diffusion approximation for the light intensity, and its breakdowns, are discussed. Chapter 2 presents the

experimental and numerical techniques necessary to characterise and understand scattering in anisotropic systems.

- Part II , Understanding nature: describes the biological inspiration of this work and provides a detailed understanding of the design principles behind its photonic structure. Chapter 3 reports a quantitative description of the light transport properties of the *Cyphochilus* beetle. In Chapter 4, numerical simulations are exploited to understand the role of anisotropy in scattering optimisation.
- Part III , From nature to applications: presents the first examples of bioinspired, scattering materials. In Chapter 5, a phase separation technique is exploited to produce polymeric networks showing the highest scattering efficiency reported for low refractive index materials thus far. Chapter 6 showcases the possibility of manufacturing scattering materials made solely of biopolymers. In particular, a fabrication technique which allows tailoring the building blocks and the morphology — and therefore the scattering — of cellulosic materials is presented.

The results delivered by this thesis, and the perspectives they envision, are discussed in summary and future perspectives.

Part I

THEORETICAL FRAMEWORK AND METHODOLOGIES

1

LIGHT PROPAGATION IN DISORDERED MEDIA

This chapter introduces the theoretical background of wave transport in disordered media. By describing the photon propagation as a random walk, it is possible to develop a statistical model for multiple scattering. In this approach, which goes under the name of *diffusion approximation*, light propagation is determined by the transport *mean free path*. This quantity — which depends on the single-particle (*form factor*) and ensemble properties (*structure factor*) of the scatterers — represents the length that light has to travel in a material before its propagation direction is randomised. The mean free path is inversely proportional to the scattering strength, i.e., the amount of light diffusely reflected by a system. This theoretical description has broad applicability but also limitations. In particular, the diffusion approximation does not account for the wave nature of photons and, therefore, interference effects. Interference can be observed experimentally and provides essential information about the scattering properties of a material.

The following text is organised into three parts. Section 1.1, introduces the main concepts of light scattering by a single particle. Then, in Section 1.2, the diffusion approximation for multiple light scattering in disordered systems is presented. Finally, Section 1.3 discusses the limitations of the diffusion approach. In particular, it describes the coherent backscattering phenomenon: an interference effect where the diffusion approximation breaks down.

1.1 SINGLE LIGHT SCATTERING

When light encounters modulations of the optical properties, e.g., the refractive index, its propagation direction deviates from a straight trajectory [1–5]. This phenomenon — which goes under the name of scattering and also includes diffraction, reflection and refraction which

are historically, and for simplicity, treated with different formalisms [5] — can be described as:

$$\psi_s(\mathbf{r}) = \mathcal{S}\psi_0(\mathbf{r}), \tag{1}$$

where $\mathcal{S}$ is the so-called *scattering matrix* (or S-matrix) [5, 23–26] and ψ_0 and ψ_s are the incident and scattered wave, respectively. The elements of the scattering matrix are a function of the incident wave (its direction, polarisation and wavelength) and the scatterer (its size, shape and refractive index).

To gain information on how the intensity is scattered, it is convenient to introduce the so-called Stokes vector [27]:

$$\mathbf{S} = \begin{pmatrix} I \\ Q \\ U \\ V \end{pmatrix}. \tag{2}$$

The different components of the Stokes vector are a set of parameters which fully describe the state of electromagnetic radiation and are referred to as the Stokes parameters. In particular, the first Stokes parameter (I) represents the intensity while Q, U, and V describe the polarisation state.

The relation between the incident ($\mathbf{S_0}$) and scattered ($\mathbf{S_s}$) Stokes vectors is:

$$\mathbf{S}_s = \mathcal{M}\mathbf{S}_0, \tag{3}$$

where $\mathcal{M}$ is the 4x4 *Mueller scattering matrix* [28]. The general relation between the S-matrix and the Mueller scattering matrix can be found in different textbooks, e.g., Reference [5].

It is particularly interesting to describe the case of a spherical scatterer. In this geometry, symmetry reduces the number of independent elements for the $\mathcal{S}$ and $\mathcal{M}$ matrices:

$$\mathcal{S} = \begin{pmatrix} S_2 & 0 \\ 0 & S_1 \end{pmatrix}, \tag{4}$$

$$\mathcal{M} = \begin{pmatrix} M_{11} & M_{12} & 0 & 0 \\ M_{12} & M_{11} & 0 & 0 \\ 0 & 0 & M_{33} & M_{34} \\ 0 & 0 & -M_{34} & M_{33} \end{pmatrix}, \tag{5}$$

and the relationship between their elements is:

$$\begin{aligned} M_{11} &= \tfrac{1}{2k^2r_1^2}\left(|S_2|^2 + |S_1|^2\right), \quad M_{12} = \tfrac{1}{2k^2r_1^2}\left(|S_2|^2 - |S_1|^2\right), \\ M_{33} &= \tfrac{1}{2k^2r_1^2}\left(S_2^*S_1 + S_2S_1^*\right), \quad M_{34} = \tfrac{i}{2k^2r_1^2}\left(S_1S_2^* - S_2S_1^*\right), \end{aligned} \tag{6}$$

where k and r_1 are the wavevector and the distance from the center of the sphere, respectively. Using now Equation 3 and assuming an unpolarised (natural) incident light (meaning $Q_0 = U_0 = V_0$) results in:

$$I_s = M_{11}I_0 = \left(|S_2|^2 + |S_1|^2\right) I_0 = \frac{d\sigma_s}{d\Omega} I_0. \tag{7}$$

The explicit form of S_2 and S_1 for a spherical scatterer can be found, for example, in Reference [5].

In Equation 7, the *diffential scattering cross-section* was defined as:

$$\frac{d\sigma_s}{d\Omega} = \frac{I_s}{I_0} = |S_2|^2 + |S_1|^2. \tag{8}$$

The differential scattering cross section describes the angular distribution of the scattered light. It is convenient to rewrite its definition as:

$$\sigma_s = \int \frac{d\sigma_s}{d\Omega} d\Omega = \int F(\theta, \phi) d\Omega, \tag{9}$$

where $F(\theta, \phi)$ is referred to as *form factor*. The integral of Equation 8 over a solid angle is defined as the *scattering cross section*:

$$\sigma_s = \int \frac{d\sigma_s}{d\Omega} d\Omega, \tag{10}$$

The scattering cross section has the units of an area and quantifies the strength of the interaction, i.e., the amount of light scattered by the particle.

Figure 2 | Single scattering regimes. Examples of the three different types of scattering by particles with different dimensions. Mie scattering is the most general case, from which both Rayleigh and ray optics can be obtained asymptotically.

Equations 8 and 10 introduced the two fundamental parameters to describe single light scattering. An analytical solution of the scattering problem is, however, not always possible.

Historically, light scattering is categorised as a function of the *size parameter* r/λ, where r and λ are the radius of the scatterer and the wavelength of light, respectively. In particular, three different scattering regimes can be defined (Figure 2): *Rayleigh scattering* ($r << \lambda$), *ray optics* ($r >> \lambda$) and *Mie scattering* ($r \simeq \lambda$). It is important to note that Mie scattering is the most general of these regimes from which the Rayleigh and ray scattering can be derived as asymptotic limits [5]. However, both Rayleigh and ray scattering can result extremely useful as they provide a first understanding of many phenomena.

Lord Rayleigh was the first scientist to study light scattering by small particles ($r << \lambda$). He observed, with elegant reasoning of dimensional analysis, that the scattering cross section of a small particle must be proportional to the fourth power of the wavelength [29]:

$$\sigma_s(\lambda)^{\text{Rayleigh}} = \frac{8\pi^3}{3}\frac{|\alpha_0|^2}{\lambda^4} \tag{11}$$

where α_0 is the polarisability of the particle [5]. The λ^{-4} dependency causes wavelengths in the blue region of the visible spectrum to be scattered more than the red hues, accounting for the blue sky and the typical red colour of the sunset.

In the opposite regime, where $r >> \lambda$, ray optics can be used to describe the propagation of light intensity. This approximation describes a light beam as a large number of rays. When encountering an interface, these rays are scattering according to Fresnel's equations and the geometrical constrictions of Snell's law [5]. Geometrical optics provides a first

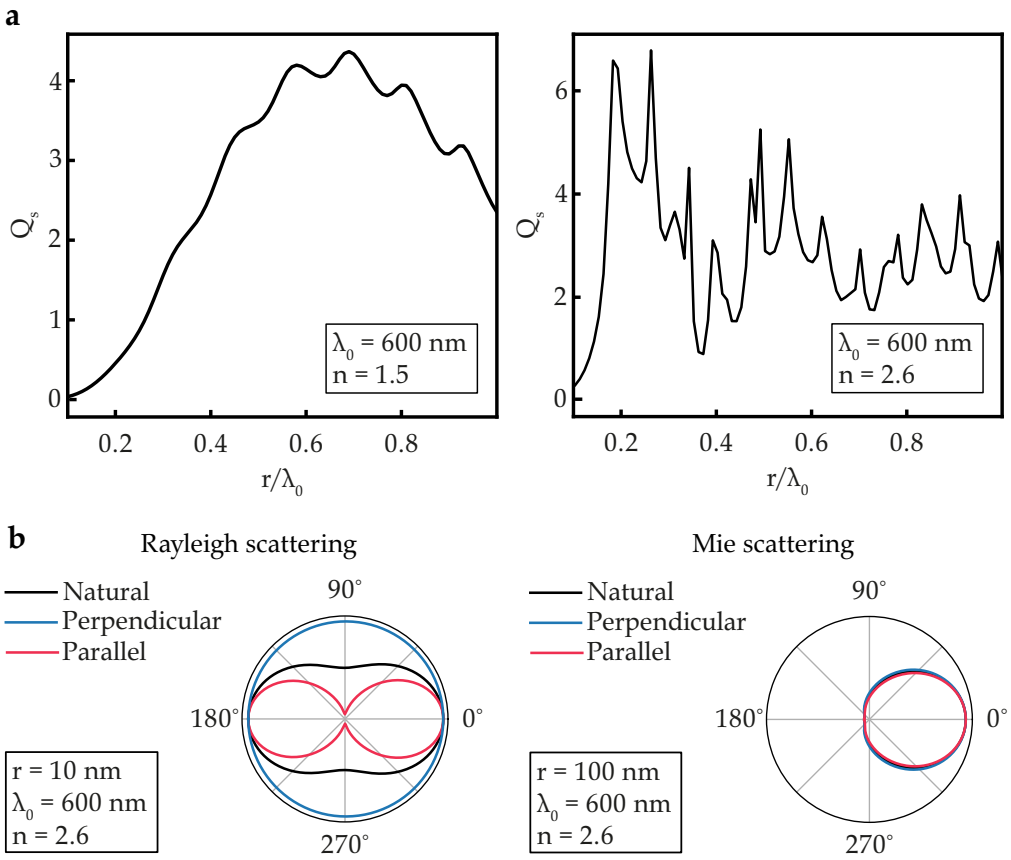

Figure 3 | Single scattering parameters. a) Scattering efficiency in function of the size parameter (r/λ_0). The Mie resonances get narrower and more intense when the refractive index (n) increases. **b)** Differential scattering cross for Rayleigh and Mie scatterers, left and right panel, respectively. The calculations in a) and b) were performed using the formulae reported in Reference [5].

understanding of many phenomena, for example, the scattering by raindrops which causes the rainbow.

This thesis focuses on materials whose building blocks have dimensions comparable to the wavelength of visible light, and therefore subject to Mie scattering. In particular, Mie scattering owns its name to Gustav Mie, who was one of the first scientists to obtain an analytical solution for the scattering of a plane wave from a sphere [30]. A typical example of Mie scattering, and whose mechanism is discussed in depth in Section 1.2, is the white colour of clouds.

Peter Debye, and Ludvig Lorenz independently found the same solution.

While the Rayleigh and the ray (geometrical) regimes have an easy mathematical description, the Mie problem is analytically solvable only for simple geometries [31]. A complete and comprehensive derivation of the Mie solution for both spheres and cylinders can be found in various textbooks, e.g., References [1, 5]. Conversely to the monotonic behaviour

as a function of the wavelength of Rayleigh scatterers (Equation 11), the scattering cross section of Mie particles exhibits many resonances (Figure 3a) — which are often referred to as *Mie resonances*. In particular, Figure 3a shows the so-called *scattering efficiency* (Q_s), which is defined as follows:

$$Q_s = \frac{\sigma_s}{\sigma_g}, \tag{12}$$

where σ_g is the geometrical cross section ($\sigma_g = \pi r^2$ for spherical particles). Another characteristic of Mie scattering is reported in Figure 3b, where the differential scattering cross section is depicted. In contrast to the Rayleigh case, where scattering is almost isotropic, in the Mie scattering regime, the differential scattering cross section strongly depends on the angle.

The next section will discuss the importance of both the scattering cross section and the differential scattering cross section on the multiple scattering.

1.2 MULTIPLE LIGHT SCATTERING

Light propagation in assembled materials cannot always be solved analytically — even assuming the knowledge of the scattering cross sections and positions of every scatterer. In ordered materials, the high symmetry in the positions of the scatterers simplifies the problem, which is well described by Bragg's law [32]. The absence of long-range order complicates the study of light propagation in disordered media. In the following, a statistical model of wave transport in disordered systems is presented.

1.2.1 *Diffusion approximation*

A key quantity to derive a statistical model of light propagation in a disordered medium is the energy density $\rho(\mathbf{r}, t)$, i.e., the probability to

find a given amount of energy at the position $\mathbf{x}$ (of coordinates $\mathbf{r}$) at the time t. In particular, the energy density can be written as:

$$\rho(\mathbf{r}, t+\delta t) = \int \rho(\mathbf{r}_1, t)\, P(\mathbf{r}-\mathbf{r}_1, \delta t|\mathbf{r}_1, t)\, d\mathbf{r}_1, \tag{13}$$

where $P(\mathbf{r}-\mathbf{r}_1, \delta t|\mathbf{r}_1, t)$ is the conditional probability of a photon to be scattered from $\mathbf{x_1}$ to $\mathbf{x}$ in a time interval δt.

The conditional probability accounts for the superpositions of many scattering events. To calculate P it is necessary to make some assumptions on the multiple scattering process. The first assumption is that each light step, i.e., the distance between two scattering events, is independent of the sequence of steps that preceded it. This memoryless theoretical framework is called *random walk* (Figure 4a) [33]. The second assumption is that the scattering is homogeneous, meaning that the scattering probability does not vary throughout the system, i.e., the distribution of the step lengths has finite moments. This assumption implies that the step length probability for a photon follows a Poisson distribution [33]:

More precisely, the memoryless class of stochastic phenomena is known as Markovian. The random walk is an example of Markovian processes.

$$P(r) \simeq exp(-\frac{r}{\ell_s}), \tag{14}$$

where ℓ_s is the average distance of free propagation between two scattering events and is often referred to as *scattering mean free path* (Figure 4b).

Based on these two assumptions, $P(\mathbf{r}-\mathbf{r}_0, \delta t|\mathbf{r}_0, t)$ can be estimated by means of the Central Limit Theorem (CLT) [34]. The CLT states that the distribution of the sum of a large number of independent random variables (in this case the scattering steps) with finite moments is Gaussian. Applying the CLT to Equation 13 results in [35]:

$$\rho(\mathbf{r}, t+\delta t) = \int \rho(\mathbf{r}_1, t)\, \frac{1}{\sqrt{4\pi D\delta t}} e^{\frac{|\mathbf{r}-\mathbf{r}_1|^2}{4D\delta t}}\, d\mathbf{r}_1, \tag{15}$$

where D is proportional to the square of the variance of the Gaussian distribution. The result of the integral in Equation 15 is [35]:

$$\rho(\mathbf{r}, t+\delta t) = \rho(\mathbf{r}, t) + D\delta t\nabla^2\rho(\mathbf{r}, t) \rightarrow \frac{\partial}{\partial t}\rho(\mathbf{r}, t) = D\nabla^2\rho(\mathbf{r}, t), \tag{16}$$

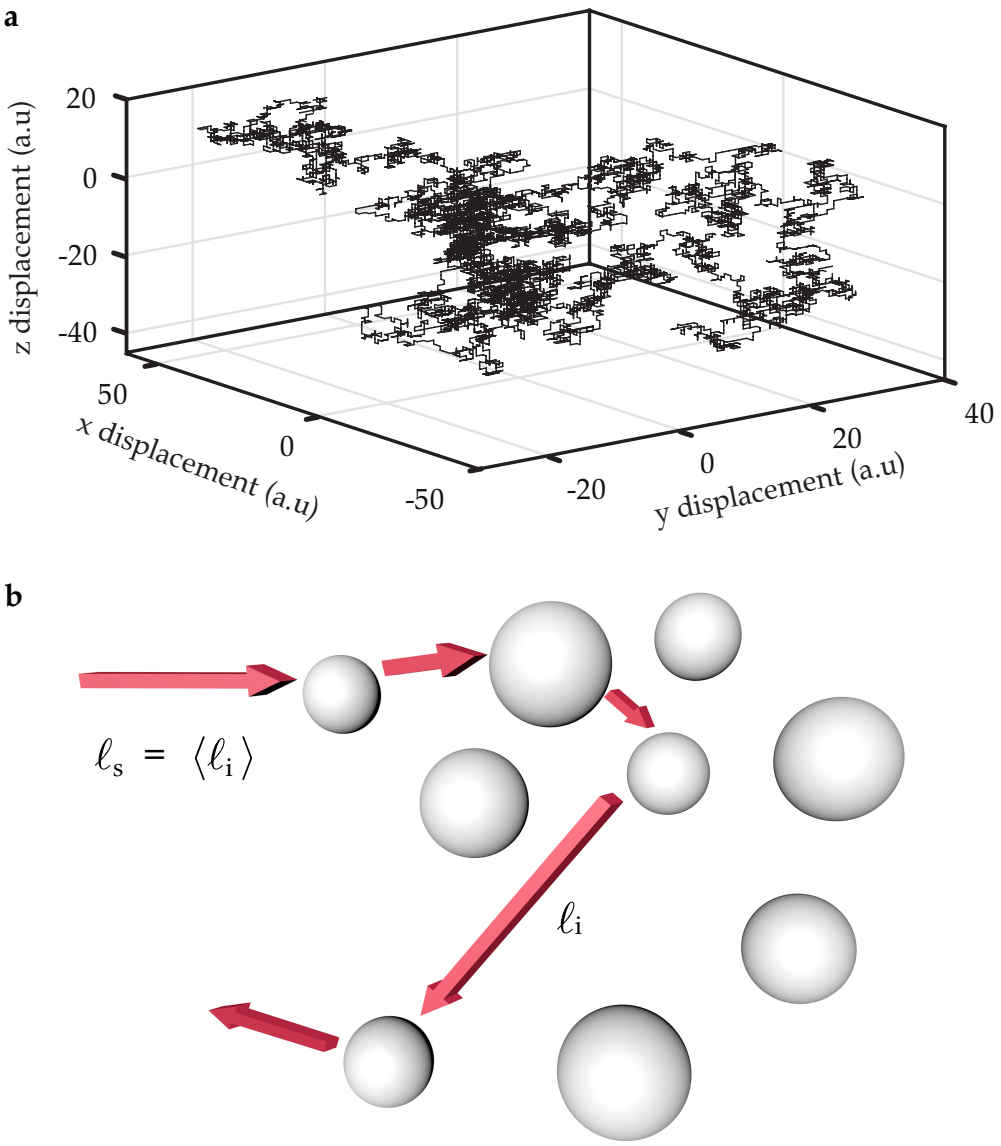

Figure 4 | Statistical description of light propagation in disordered media. a) Simulation of a three-dimensional random walk. Each step (10^4 total) corresponds to a displacement of r (sampled from Equation 14) from the position of the previous scattering event. **b)** Schematic illustration of light propagation in a disordered medium. For simplicity, the scatterers are represented as spheres and the light path with an arrow. The scattering mean free path (ℓ_s) is defined as the average distance between two scattering events.

which represents the *diffusion equation* for the energy probability. The diffusion equation can then be generalised as:

$$\frac{\partial}{\partial t}\rho(\mathbf{r},t) = D\nabla^2\rho(\mathbf{r},t) + S(\mathbf{r},t) - \frac{v_e}{\ell_a}, \tag{17}$$

where $S(\mathbf{r},t)$ is the source term, v_e is the energy velocity and ℓ_a is the *absorption mean free path*.

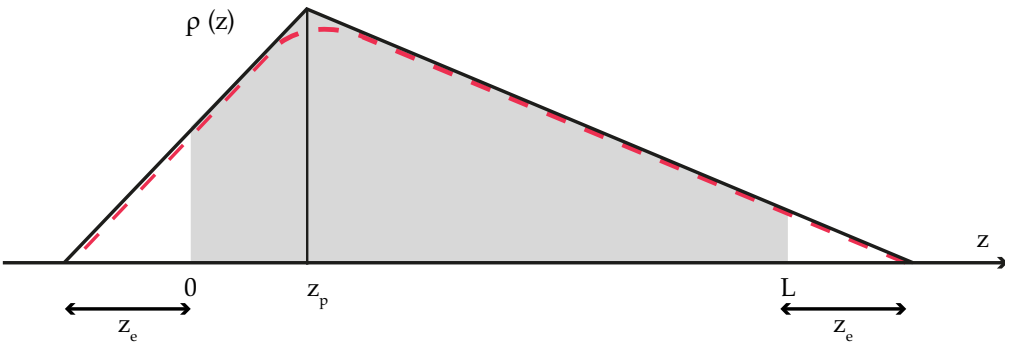

Figure 5 | Energy density distribution in a disordered material. The black and red lines represent the solution of the diffusion equation in a slab geometry using a delta and an exponential source (placed in z_p), respectively. The grey area represents the region where the sample is present. The energy extrapolates to zero outside the slab, at a distance z_e from its surfaces.

This thesis focuses on stationary properties of disordered media; therefore, Equation 17 simplifies to:

$$D\nabla^2\rho(\mathbf{r},t) + S(\mathbf{r},t) - \frac{v_e}{\ell_a} = 0. \tag{18}$$

To solve Equation 18 is necessary to define the boundary conditions and the source term. A convenient geometry to solve the diffusion equation is the slab geometry, i.e., the dimensions of the system in the direction perpendicular to the incoming light are considered infinite. In this configuration, that well describes the systems presented in this thesis, one could think to use as boundaries conditions that the energy density is zero at $z = 0$ and $z = L$, where L is the thickness of the slab (Figure 5). However, such conditions would imply that no energy could enter or exit the system [36, 37].

As shown in References [36, 37], the correct Dirichlet boundary conditions are:

$$\rho(z) = 0 \quad \text{at} \begin{cases} z = -z_e \\ z = L + z_e \end{cases} \tag{19}$$

where z_e is the extrapolation length, i.e., the positions outside the slab where the light intensity extrapolates to zero (Figure 5).

Regarding the source term, Equation 18 accounts only for diffused light and therefore, a plane wave is not suitable. Two diffusive sources are: (i) a point-like source $S(z) = S(0) \cdot \delta(z - z_p)$; (ii) an exponentially decaying source $S(z) = S(0) \cdot \exp(-z/z_p)$. Note that both (i) and (ii) are located

in z_p, which is the so-called *penetration length* (Figure 5). This parameter represents the distance light propagates ballistically in the sample before being scattered for the first time, and its usually to $z_p = \ell_s$.

The solution of Equation 18 using the boundary conditions in Equation 19 and a point-like source is:

$$\rho(z) = \rho(z_p) \begin{cases} \sinh[\alpha(z_e + z)] / \sinh[\alpha(z_p + z_e)] & z < z_p \\ \sinh[\alpha(L + z_e - z)] / \sinh[\alpha(L + z_p + z_e)] & z > z_p \end{cases} \tag{20}$$

where

$$\begin{aligned} \rho(z_p) &= \frac{S(0)}{\alpha D} \frac{\sinh[\alpha(z_p + z_e)] \sinh[\alpha(L + z_e - z_p)]}{\sinh[\alpha(L + 2z_e)]}, \\ z_e &= \frac{1}{2\alpha} \ln\left[\frac{1 + \alpha z_0}{1 - \alpha z_0}\right], \\ z_0 &= \frac{2}{3}\ell_s \left(\frac{1 + R}{1 - R}\right), \\ \alpha &= \frac{1}{\ell_a}. \end{aligned} \tag{21}$$

In Equation 21 the parameter R represents the angle- and polarisation-averaged reflection coefficient [36]:

$$R = \frac{3\int_{-\pi/2}^{0} R(\theta)\sin(\theta)\cos^2(\theta)d\theta + 2\int_{0}^{\pi/2} R(\theta)\sin(\theta)\cos(\theta)d\theta}{3\int_{-\pi/2}^{0} R(\theta)\sin(\theta)\cos^2(\theta)d\theta - 2\int_{0}^{\pi/2} R(\theta)\sin(\theta)\cos(\theta)d\theta + 2}, \tag{22}$$

where $R(\theta)$ is the polarisation-averaged Fresnel's coefficient [38].

The reflection coefficient depends on the effective refractive index (n_e) of the disordered medium, which was estimated by the Maxwell-Garnett's theory [39]:

$$n_e = \frac{1 + 2ff(\frac{n^2-1}{n^2+2})}{1 - ff(\frac{n^2-1}{n^2+2})}, \tag{23}$$

where n is the refractive index of the scatterers, which are assumed to be in air, and ff is the volume fraction.

Figure 5 shows the solutions to Equation 18 using both a point-like and an exponentially decaying source. To link the solution presented in

Equation 20 to experimental measurables, the total transmission of light (T) can be estimated (cf. Chapter 2). T is defined as the transmission integrated over the transmission angles, and it can be obtained by dividing the total flux at $z = L$ by the incident flux $S(0)$ [37]:

$$T(L,\lambda) = \frac{1-R}{\alpha}\frac{\sinh\left[\alpha\left(z_p + z_e\right)\right]\sinh\left[\alpha z_e\right)]}{\sinh\left[\alpha\left(L + 2z_e\right)\right]}, \tag{24}$$

that in the case of negligible absorption ($\alpha \to 0$) simplifies to:

$$T(L,\lambda) = \frac{2z_e}{L + 2z_e}. \tag{25}$$

Note that Equation 25 is independent of the source used to solve Equation 18, as the two coincides in the asymptotic limit $L >> \ell_s$ [35].

From Equation 20, and following the details presented in References [40, 41], it is possible to obtain an analytical expression of the angular distribution of transmitted light $P_T(\mu)$:

$$P_T(\mu) = \mu\frac{\overline{z_e} + \mu}{\overline{z_e}/2 + 1/3}, \tag{26}$$

where $\mu = \cos(\theta)$, with θ the transmission angle and $\overline{z_e} = z_e/\ell_s$. $P_t(\mu)$ can be measuared experimetally, as shown in Chapter 2.

Therefore, using Equation 25 together with Equation 22 or Equation 26 provides a closed system of equations to estimate the mean free path experimentally. However, it is important to remind that the results presented thus far relies on two assumptions:

1. the scattering steps are independent
2. the distributions of the scattering steps has finite moments

In this framework, the characteristic length of the diffusion process is the scattering mean free path. This quantity was defined in Equation 14, and it depends on the properties of the scatterers as:

$$\ell_s = \frac{1}{n_p \sigma_s} \tag{27}$$

where n_p is the number density of the scatterers and σ_s their scattering cross section (assuming that the scatterers are identical).

The assumption of independent scattering steps breaks down when the dimension of the scatterers is comparable to the wavelength of light. Mie scatters exhibit an asymmetric differential scattering cross section (Figure 3), which results in a correlation between scattering events. This effect can be accounted for by redefining the characteristic length of the diffusive propagation as:

$$\ell_t = \frac{\ell_s}{1-g}, \tag{28}$$

where

$$g = \langle \cos\theta \rangle = \frac{\int \cos\theta \sigma_s \, d\Omega}{\int \sigma_s \, d\Omega}. \tag{29}$$

ℓ_t is the so-called *transport mean free path*, or mean free path, and its reciprocal is often referred to as *scattering efficiency*. g is the *scattering asymmetry* parameter. In Rayleigh scatterers $g = 0$ while typically for Mie scatterers $g > 1$, resulting in $\ell_t > \ell_s$. However, a scattering asymmetry smaller than one was demonstrated by exploiting the Kerker conditions [42].

The scattering cross section in Equation 29 is a single scattering property (Equation 9). In the diffusive regime, the scattering cross section can be generalised to account for collective scattering effect [7, 43]:

$$\sigma_s = \int F(\theta, \phi) S(\theta, \phi) \, d\Omega, \tag{30}$$

where $S(\theta, \phi)$ is called *structure factor*. The structure factor is proportional to the Fourier transform of the position of the scatterers:

$$S(\mathbf{k}) = \frac{1}{N} \left\langle \sum_{i,j=1}^{N} e^{-i\mathbf{k}\cdot(\mathbf{r}_i - \mathbf{r}_j)} \right\rangle. \tag{31}$$

The structure factor can, in principle, be calculated from the Ornstein–Zernike equation [44], which is an integral equation for the correlation function. The Ornstein–Zernike equation has an analytical solution for the random packing of hard spheres which goes under the name of Percus-Yevick closure relation [45]. A semi-analytical solution can be obtained for hard disks (2D) following the derivation of Baus

and Colot [46]. Reference [46] also provides an analytical solution for one-dimensional systems made of hard semi-infinite rods.

Equation 30 shows that is the interplay between the form and the structure factor that determines the scattering properties of a disordered medium. In a purely random system, i.e., where there is no correlation between the position of the scatterers ($S(\mathbf{k}) = 1$), the scattering is solely determined by the form factor. In this case, when the scatterers are polydisperse, the system does not show any resonant response in function of the wavelength. If the scatterers are monodispersed, a resonant behaviour, resembling the single scattering Mie resonances, is observed. However, real systems are random only if very dilute. Otherwise, the contribution of the structure factor needs to be accounted as it can modify the frequency and intensity of the Mie resonances [47–49]. It is important to note that, in the diffusive regime, monodispersed systems look white, even though they exhibit resonant scattering (cf. Reference [50] and Appendix c). The visual appearance is dominated by the broadband multiple scattering background of which the resonances represent only a small modulation.

While the independent scattering assumption can be relaxed by redefining the characteristic length of the random walk, the diffusion approximation breaks down if the assumption related to the moments of the scattering steps distribution is not valid. The next section describes different situations in which the diffusion model cannot be used to study light propagation in disordered media.

1.3 LIMITS OF THE DIFFUSION APPROXIMATION

The assumption regarding the moments of the distribution of scattering steps is satisfied if the scattering is homogeneous throughout the system. It, therefore, breaks down if the ballistic component of the incoming beam is not completely converted in diffused light by scattering. Numerical studies demonstrated that the predictions of the diffusion equation are correct only for $\mathrm{OT} = \ell_t/L > 8$ [10–12]. For $\mathrm{OT} < 8$, the diffusion model has to be replaced with the more general radiative transfer equation [51].

A distribution is stable if summing infinite of its copies results in the same distribution

Another scenario where the diffusion approximation breaks down is when the scattering steps belong to a scale-invariant *Lévy distribution*. A Lévy distribution is a family of stable distributions of which only the Gaussian has a characteristic length. The other types of Lévy distribution are scale-invariant, meaning that they do not change if observed at different length scales. If the step distribution is a scale-invariant Lévy, the photon random walk is described by the so-called *anomalous diffusion* [35, 52–55]. In this regime, it is not possible to define a mean free path and the optical properties scale differently with the thickness than in Equation 25. Even if the microscopics details of the transport are different from Subsection 1.2.1, a system in the anomalous diffusion regime also shows a macroscopic white appearance [54–56].

The assumption of homogeneous scattering is not valid when the system is anisotropic [57] — with an anisotropy that can be in the form factor, namely in the refractive index or shape of the scatterers, or in the structure factor. A more general version of Equation 18, where a diffusion tensor replaces the diffusion coefficient, was proposed to describe anisotropic diffusion [51, 58–61]. However, the validity of this approach and the relation of the diffusion tensor with the microscopic scattering properties is still an argument of debate [57, 62, 63]. Therefore, to study the optical properties of anisotropic disordered media, it is necessary to exploit numerical methods (cf. Part II). The diffusion approximation is still valid for systems where the anisotropy is small, e.g., in liquid crystals [64, 65], or to investigate the optical properties in the direction of the incoming light (cf. Part III). Indeed, it can be shown that the transport properties along its thickness determine the amount of light diffusely reflected by an anisotropic, slab-geometry system [57, 63, 66]

In addition to the limitations related to the nature of the step length distribution, the diffusion approximation does not take into account the wave nature of photons. Therefore, it disregards interference effects.

1.3.1 *Coherent backscattering phenomenon*

Interference effects can be observed when a coherent source illuminates a disordered system. In this case, the intensity profile of scattered

light assumes a complex pattern of dark and bright spots which is known as *speckles*. The speckle pattern is the result of the interference between photons that travelled different paths inside the material, and it provides important information about the position and the dynamics of the scattering centres [67, 68].

Due to the disordered organisation of the scatterers, the speckles vanish if averaged over many sample configurations, e.g., if the system is a liquid. However, the interference between *counter-propagating waves*, i.e., waves that have travelled the same path but in opposite directions, survives averaging. The superposition of the interference patterns from different counter-propagating, or reciprocal, waves gives rise to the *coherent backscattering* effect [69–71]. The coherent backscattering pattern shows up as an intensity distribution whose maximum corresponds with the backscattering direction and then decreases following a conical shape.

A qualitative way to understand this phenomenon is to consider a two-wave interference pattern, which can be expressed as:

$$I(\theta, \phi) = I_0(1 + \zeta \cos(\mathbf{d} \cdot \Delta\mathbf{k})), \tag{32}$$

where I_0 and ζ are the total intensity neglecting interferences and the contrast of the interference, respectively. The incident and scattered k-vector $\mathbf{k_i}$ and $\mathbf{k_f}$ are defined as:

$$\begin{aligned} \mathbf{k_i} &= (0, 0, k), \\ \mathbf{k_f} &= (-k\sin\theta\cos\phi, -k\sin\theta\sin\phi, -k\cos\theta). \end{aligned} \tag{33}$$

In the study of the coherent backscattering effect, the two interfering waves considered are counter-propagating (Figure 6). Given a wave, the existence, and their equality in amplitude, of its reciprocal one, is guaranteed by the reciprocity theorem [1]. The reciprocity theorem states that source and detector can always be inverted. The validity of the theorem is based on the time-reversal symmetry of Maxwell equations. This hypothesis breaks down, for example, in the presence of non-linear materials or applied magnetic fields [72]. In particular, from the reciprocity theorem follows that $\zeta = 1$.

A two-wave interference profile has a sinusoidal dependency as a function of the angle, with a maximum at the backscattering direction

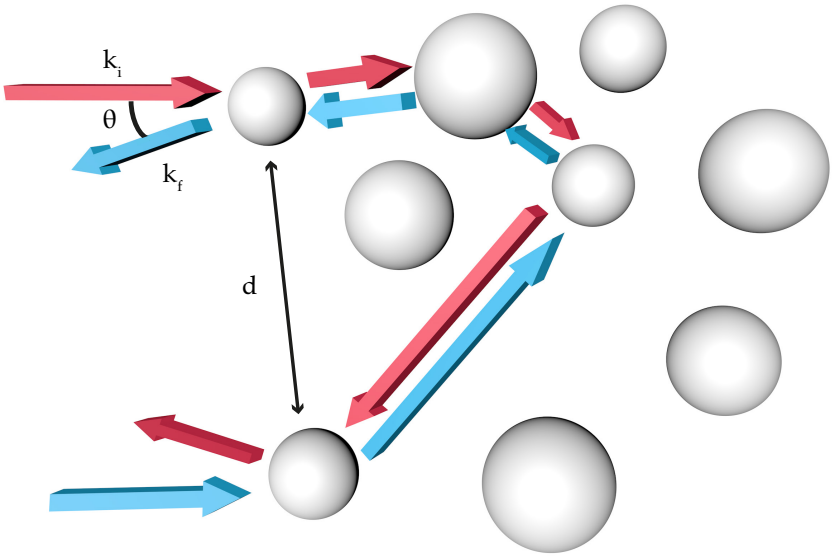

Figure 6 | Schematic illustration of two counterpropagating waves. For simplicity, the scatterers are represented as spheres and the two light paths with red and cyan arrows.

$\theta = 0$. The periodicity of the sinusoidal modulation is inversely proportional to the distance between the first and the last scatterer (d in Figure 6):

$$\Delta\psi = \frac{1}{\mathbf{d} \cdot \Delta\mathbf{k}}, \tag{34}$$

and which can be simplified in the small θ limit into:

$$\Delta\psi \simeq \frac{\lambda}{2\pi|\mathbf{r_N} - \mathbf{r_1}|}, \tag{35}$$

where $\mathbf{r_1}$ and $\mathbf{r_N}$ are the coordinates of the first and last scattering events, respectively.

The coherent backscattering signal originates from the superposition of all these fringes. In particular, the cusp top of the intensity distribution is determined by the photons which travelled a long path inside the material, i.e., to high scattering orders (Figure 7). If $|\mathbf{r_N} - \mathbf{r_1}|$ is replaced in Equation 35 by the mean separation distance between the first and last scatterers, which is of the order of the transport mean free path (ℓ_t), the phase difference between the reciprocal paths becomes:

$$\Delta\psi \simeq \frac{\lambda}{2\pi\ell_t}. \tag{36}$$

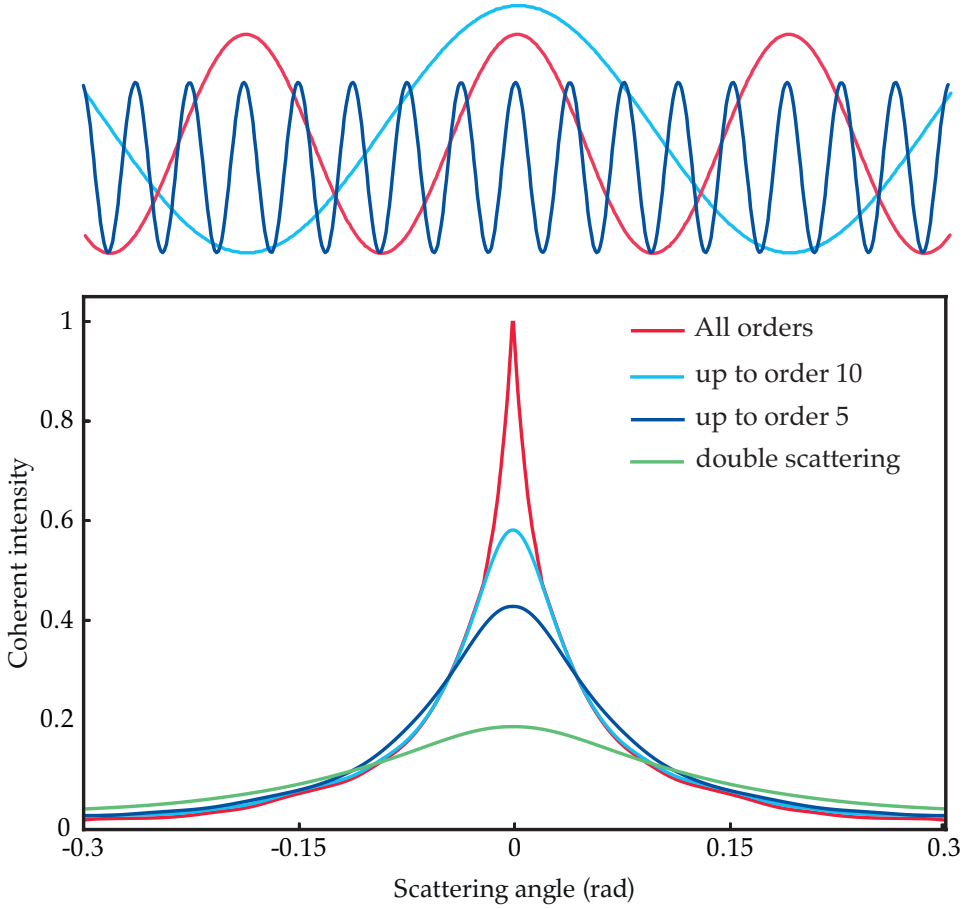

Figure 7 | Origin of the coherent backscattering effect. The coherent backscattering arises from the superposition of many two-wave interference patterns which are all in phase at $\theta = 0$ (top panel). The interference at small angles is determined by the photons which travelled a long path inside the system, i.e., to high scattering orders. The coherent backscattering profiles were obtained with Monte Carlo simulations for scalar waves (cf. Chapter 2).

Equation 36 gives a qualitative idea of the link between the interference pattern and the parameter that characterises the scattering strength of a medium, i.e., the transport mean free path. In order to better understand this connection, it is necessary to find the analytical expression of the backscattering cone.

The backscattered intensity is the result of two types of contribution: the coherent one, discussed above, and the incoherent diffuse background [69–71]. An analytical expression for these contributions can be obtained starting from the radiative transfer equation — details in, for example, Reference [51].

A convenient way to express the incoherent (γ_l) and coherent (γ_c) contributions is in their integral form:

$$\begin{aligned}\gamma_l^{(N)} =& \frac{4\pi n_p^N}{A}\int e^{-z_1/\ell_t}\left(\frac{d\sigma}{d\Omega}\right)_1\left(16\pi^2 G\left(k,\mathbf{r}_{12}\right)G^*\left(k,\mathbf{r}_{12}\right)\right)\left(\frac{d\sigma}{d\Omega}\right)_2\cdots \\ &\cdots\left(\frac{d\sigma}{d\Omega}\right)_{N-1}\left(16\pi^2 G\left(k,\mathbf{r}_{N-1,N}\right)G^*\left(k,\mathbf{r}_{N-1,N}\right)\right)\left(\frac{d\sigma}{d\Omega}\right)_N \\ & e^{-z_N/\ell_t}\,d\mathbf{r}_1\,d\mathbf{r}_1\ldots d\mathbf{r}_N\end{aligned}, \tag{37}$$

$$\begin{aligned}\gamma_C^{(N)} =& \frac{4\pi n_p^N}{A}\int e^{-z_1/\ell_t}\left(\frac{d\sigma}{d\Omega}\right)_1\left(16\pi^2 G\left(k,\mathbf{r}_{12}\right)G^*\left(k,\mathbf{r}_{12}\right)\right)\left(\frac{d\sigma}{d\Omega}\right)_2\cdots \\ &\cdots\left(\frac{d\sigma}{d\Omega}\right)_{N-1}\left(16\pi^2 G\left(k,\mathbf{r}_{N-1,N}\right)G^*\left(k,\mathbf{r}_{N-1,N}\right)\right)\left(\frac{d\sigma}{d\Omega}\right)_N \\ & e^{-z_N/\ell_t}\cos\left[\left(\mathbf{k}_{in}+\mathbf{k}_{out}\right)\cdot\left(\mathbf{r}_N-\mathbf{r}_1\right)\right]d\mathbf{r}_1\,d\mathbf{r}_1\ldots d\mathbf{r}_N\end{aligned}, \tag{38}$$

where n_p, A, N and G are the scatterers density, the illuminated area, the scattering order and the amplitude Green function, respectively.

Equations 37 and 38 can be interpreted in terms of a random walk. In particular, the scattering events are represented by the terms $(d\sigma/d\Omega)_i$ while $G\left(k,\mathbf{r}_{12}\right)G^*\left(k,\mathbf{r}_{12}\right)$ describes the propagation of a photon between two scattering events. The exponential terms $exp(-z_1/\ell_t)$ and $exp(-z_N/\ell_t)$ represent the loss of intensity before the first and last scattering events (where z is the direction of the incoming light), respectively. The interference pattern originates, as qualitatively discussed in Equation 34, by the $\cos\left[\left(\mathbf{k}_{in}+\mathbf{k}_{out}\right)\cdot\left(\mathbf{r}_N-\mathbf{r}_1\right)\right]$ term in Equation 38.

The analytical solution of Equations 37 and 38 for isotropic media is [73]:

$$\begin{aligned}\gamma_l = \frac{3\mu}{1-\alpha^2}\Bigg[&\frac{1}{\mu}\left(e^{-\nu b}-1\right)+\frac{1+\alpha-(1+\alpha)\,e^{(-2\alpha u)}}{4\alpha\,(1+\alpha)}\left(1-e^{-\nu b}\right) \\ &+\frac{1+\alpha-(1-\alpha)\,e^{(-2\alpha u)}}{4\alpha\,(1-\alpha)}e^{2\alpha u}\left(e^{b(\alpha-1)}-1\right)\Bigg],\end{aligned} \tag{39}$$

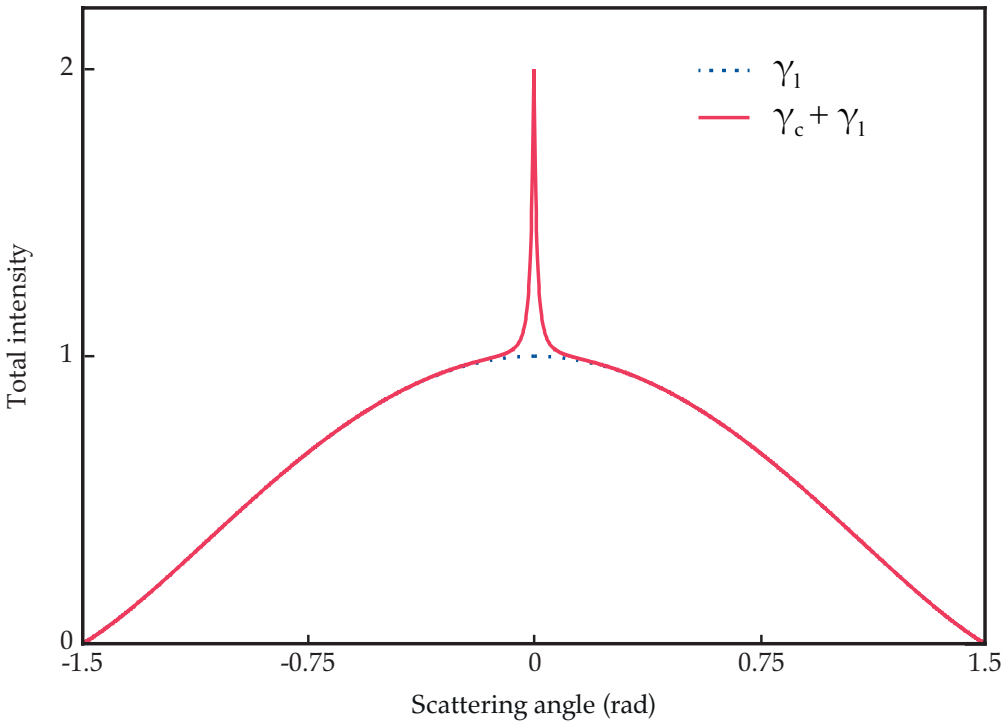

Figure 8 | Angular dependency of the bistatic coefficients. The difference between the two curves, obtained using the semi-infinite theory, arises in an angular range around the backscattering direction. The width of this angular region depends on the scattering strength of the disordered material. At the exact backscattering direction, the coherent signal, red curve, reaches an intensity that is two times that of the incoherent one, blue curve.

$$
\begin{aligned}
\gamma_c = \frac{3e^{-\nu b}}{2\alpha\nu\sinh(\alpha B)} \Bigg[& \left(\frac{1}{(\nu-\alpha)^2+u^2} \{\nu - (\nu-\alpha)\cosh(2\alpha\tau_0)\} \right. \\
& \left. + \frac{1}{(\nu+\alpha)^2+u^2} \{\nu - (\nu+\alpha)\cosh(2\alpha\tau_0)\} \right) \cos(ub) \\
& + \left(\frac{u}{(\nu+\alpha)^2+u^2} - \frac{u}{(\nu-\alpha)^2+u^2} \right) \sinh(2\alpha\tau_0)\sin(ub) \\
& + \frac{1}{(\nu-\alpha)^2+u^2} \{(\nu-\alpha)\cosh[(\nu-\alpha)b - 2\alpha\tau_0] - (\nu)\cosh[(\nu-\alpha)b]\} \\
& + \frac{1}{(\nu+\alpha)^2+u^2} \{(\nu+\alpha)\cosh[(\nu+\alpha)b + 2c\tau_0] - (\nu)\cosh[(\nu+\alpha)b]\} \Bigg],
\end{aligned}
\tag{40}
$$

where $\mu = \cos(\theta)$, $\nu = \frac{1}{2}(1 + \frac{1}{\mu})$, $u = k\ell_t(1-\mu)$, $\alpha = k\ell_t \sin(\theta)$, $B = b + 2z_e$. The parameters k, ℓ_t, and b are the wave vector, the isotropic transport mean free path, and the optical thickness, respectively. For

semi-infinite media, i.e., $b \to \infty$, Equation 40 reduces to [73]:

$$\gamma_{c,semi} = \frac{3\left[\alpha + \nu\left(1 - e^{-2z\alpha}\right)\right]}{2\alpha\mu\nu\left[(\alpha+\nu)^2 + u^2\right]}. \tag{41}$$

The coherent backscattering signal, Equations 40 and 41, has a full width half maximum that is:

$$w \simeq \frac{z_e}{k\ell_t}, \tag{42}$$

in agreement with what qualitative discussed in Equation 36. In the semi-infinite case, the incoherent component follows Lambert's cosine law for ideal diffusers [74]. The angular trend of the bistatic coefficients is shown in Figure 8.

The normalised backscattered intensity $I(\theta)$ can be written as [75]:

$$I(\theta) = \frac{\gamma_c(\theta) + \gamma_l(\theta) + \gamma_s + \gamma_{stray}}{\gamma_l(\theta) + \gamma_s + \gamma_{stray}}, \tag{43}$$

where γ_s and γ_{stray} are the bistatic coefficients for the single scattering and the stray light, respectively. The backscattering enhancement (E) is the value of Equation 43 at $\theta = 0$. Considering a semi-infinite system where the single scattering is filtered out and the stray light is blocked, then:

$$E_{semi} = \frac{\gamma_{c,semi}(0) + \gamma_{l,semi}(0)}{\gamma_{l,semi}(0)} = 2. \tag{44}$$

As shown in Figure 7, the coherent interference profile at small angles is mainly determined by high scattering orders, i.e., to photons that have propagated a long distance in the medium before being reflected. In systems with a finite size, the average distance travelled in the thickness direction is $\sqrt{N}\ell_t$, implying that the maximum scattering order supported by the system is $N \simeq OT^2$. Therefore, if the OT is not large, the value of enhancement decreases compared to Equation 44 and the interference profile shows a rounded top and not a cusp. Similarly, the presence of absorption changes the cone profile, as the amplitude of the long paths is more attenuated than that of short ones. Another effect that results in a rounding of the cone shape is related to recurrent scattering events. In fact, in media where the scattering efficiency is

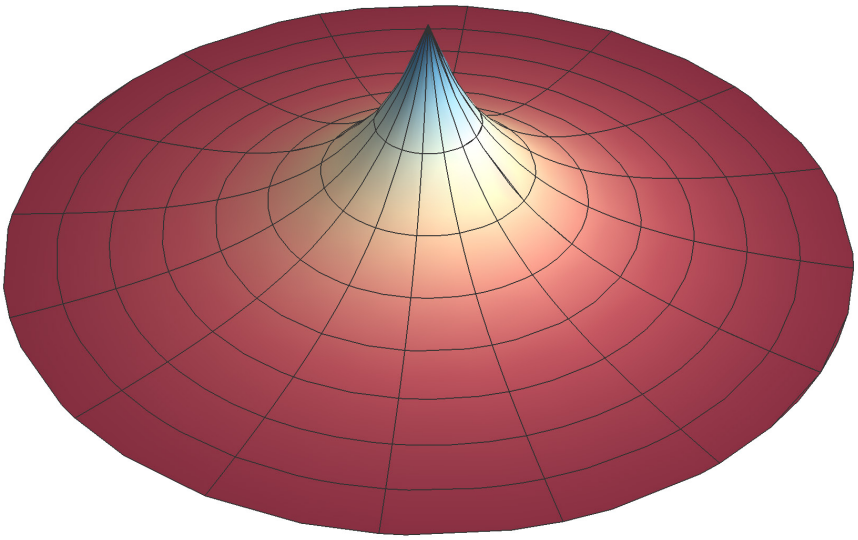

Figure 9 | Theoretical shape of the coherent backscattering cone in three dimensions. In isotropic systems, the width of the coherent backscattering is independent of the direction. The three-dimensional shape was obtained by rotating Equation 41 around an axis of revolution that passes through $\theta = 0$.

high enough, it is possible to have closed-loop photon paths [76–78]. For these paths, the first and the last scatterers coincide, giving rise to an angular independent coherent contribution that lowers the enhancement factor. Note that the rounding of the cone due to the recurrent scattering is indistinguishable from that caused by the presence of absorption or to the finite size of the system [79–81].

The three-dimensional shape of the coherent contribution (γ_c) to the backscattering interference profile — determined by the revolution of Equation 41, as γ_c does not depend on ϕ — is a cone (Figure 9). In the case of isotropic material, the cone has the same width along different directions. To describe the coherent backscattering in anisotropic systems is necessary to exploit numerical methods. Monte Carlo simulations showed that the presence of anisotropy in the plane perpendicular to the incoming light gives rise to an anisotropic cone width [51]. The ratio of the different width of the cone provides a direct estimate of anisotropy of the mean free path [51]. Chapter 4, using a Monte Carlo approach presented in Chapter 2, investigates how the coherent backscattering is affected when the anisotropy is along the direction of the incoming light.

2

METHODS

This chapter presents the methods used in this thesis to characterise light propagation in both biological and artificial disordered systems. The text is organised as follows: Section 2.1 covers the experimental techniques adopted to quantify the scattering strength of a system, exploiting both the diffusion approximation and non-diffusive phenomena; Section 2.2 presents the numerical methods exploited to describe light propagation in anisotropic systems, both to analyse experimental results and to understand the role of anisotropy in scattering optimisation.

2.1 EXPERIMENTAL METHODS

2.1.1 *Coherent backscattering setup*

A coherent backscattering (CBS) setup measures the angular distribution of the coherently backscattered light. This experimental technique provides a direct estimate of the strength of a system (cf. Chapter 1). The characterisation of strongly scattering materials requires the detector to move over a broad angular range — as the angular width of the coherent backscattering line shape is inversely proportional to the mean free path (cf. Equation 42, Subsection 1.3.1).

A schematic of the setup used to measure the CBS effect is shown in Figure 10. A collimated laser diode (Thorlabs CPS635R, a peak wavelength of 635 nm and an output power of 1.2 mW) was used as the light source. The scattered signal was focused, using a parabolic mirror, on a 100 µm core fibre (Thorlabs FC-UV100-2-SR) mounted on a motorised stage (Newport ESP301, an accuracy of $\pm$ 0.0115°) and connected to a cooled spectrometer (Avantes AvaSpec-ULS2048x64TEC-EVO).

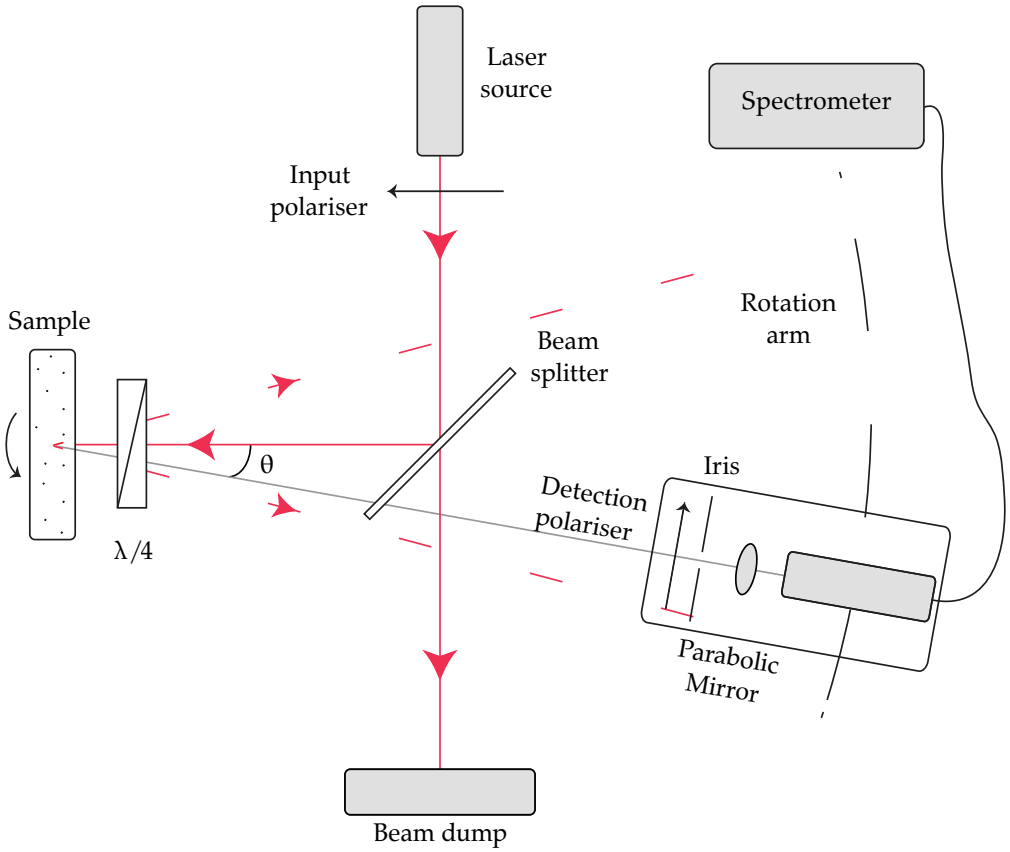

Figure 10 | Schematics of the CBS setup. The red dashed lines define the cone of backscattered intensity, while the black dashed arch represents the detection range. The sample was mounted on a rotation mount, whose axis was perpendicular to the propagation direction of the laser beam, to average over different disorder realisations.

Two factors limited the angular range of the setup:

- The range of the detector arm movement was limited by the physical space occupied by the source, on one side, and of the beam dump, on the other one. With such restrictions, the maximum angular range was $\pm 50°$.
- The dimensions of the quarter-wave plate (Thorlabs WPQ20ME-633), which shadows the sample at large illumination angles. Although the quarter-wave plate is $\simeq 5\,\mathrm{cm}$ in diameter, and it was mounted as close as possible to the sample ($\simeq 1\,\mathrm{mm}$), its rotating holder limited the angular range due to its physical dimension.

This second restriction reduced the detection range of the setup to about $\pm 40°$. The detection optics limits the angular resolution of the CBS setup. A $100\,\mu\mathrm{m}$ core fibre, with its tip at $30\,\mathrm{cm}$ distance from the sample allowed a resolution of $0.015°$.

As introduced in Chapter 1, the coherent backscattering signal is the result of constructive interference between scattered light (cf. Subsection 1.3.1). To see this effect, the speckle pattern, which occurs due to the high spatial coherence of the light source, has to be averaged out [82]. This was achieved by placing the sample on a rotation mount whose axis coincides with the propagation direction of the incoming light. This averaging procedure precludes the possibility of investigating a potential in-plane (*xy*) anisotropy.

The enhancement factor of the coherent signal is defined as the ratio between the intensity at the exact backscattering angle and the incoherent background (cf. Subsection 1.3.1). To maximise the enhancement, it is, therefore, necessary to screen the setup from stray light by enclosing it in a black box. A beam dump was then used to avoid the contribution of the reflection of the incident laser beam from the enclosing box. The enhancement factor is equal to 2 in the absence of single scattering events, which do not have a reciprocal counterpart and therefore contribute only to the incoherent background. A quarter-wave plate was used to filter out the contribution of single scattering events, by transforming the polarisation of the incident light from linear to circular. Single scattering changes light polarisation from right- to left-handed, and vice versa. This change in circular polarisation was converted back to linear by the quarter-wave plate but rotated by 90° from the input polarisation. A second linear polariser, part of the detection optics, can thus block it, allowing to filter the single-scattered light. This polarisation selectivity does not stop the rest of the signal — multiple scattering scrambles the starting polarisation [4], so that only a small part of it is filtered. This investigation method is often referred to as *helicity conserving* channel (HC) [83]. Another way to filter the single-scattered light is to remove the quarter-wave plate and place the detection polariser with the optical axis orthogonal to the starting one — single scattering preserves linear polarisation. This channel of acquisition is called *linear non-conserving* (LNC). The LNC channel stops the single-scattered light as efficiently as the HC one. However, its theoretical enhancement factor is only 1.3 as opposed to 2. A scalar theory cannot explain this dramatic difference (e.g., the one described in Subsection 1.3.1). Instead, it requires a vectorial theory accounting

A zero-order quarter-wave plate ($\lambda/4$) was used in the CBS setup — as it assures a better angular tolerance than a multi-order one.

for light polarisation [84, 85]. As described in Reference [83], the LNC signal is then used to normalise the HC signal.

Another factor to take into account in the realisation of a backscattering setup is the effect of internal reflections [36, 86, 87]. This effect is a consequence of the refractive index mismatch between the sample and the external medium. The light reflected at the sample-medium interface can be discriminated in two contributions:

- the part reflected in an area of the sample illuminated by the incident beam, which has an active role in the formation of the backscattering signal. This contribution modifies the path-length distribution inside the sample, introducing artificially long path and causing a narrowing of the cone (cf. Subsection 1.3.1). This artefact can be removed in two different methods: (i) using Equation 21 to calculate the value of the extrapolation length (which depends on the refractive index contrast at the boundary of the medium); (ii) index matching the sample. In Section 3.2, the former approach was adopted.
- the remaining light, which, due to the absence of a corresponding reverse path, does not contribute to the coherent signal. This incoherent contribution affects the backscattering cone by lowering the enhancement factor. An iris was placed between the beam splitter and the acquisition fibre (Figure 10), allowing only the scattered light from the illuminated region of the sample to reach the detector.

2.1.2 *Integrating sphere*

The scattering strength of a system can be determined by measuring the total transmission as a function of the thickness (cf. Equation 25, Chapter 1). A widely used instrument to measure the total transmission is the integrating sphere. This instrument consists of a hollow sphere whose internal surfaces are coated with a material with high, broadband Lambertian reflectance.

The Spectralon, SRM-990, used in this thesis has a reflectance $> 99\%$.

The experimental setup used in Chapter 5 is illustrated in Figure 11. A light source (Ocean Optics HPX-2000) was coupled into an optical fibre (Thorlabs FC-UV100-2-SR). The transmitted light was collected by

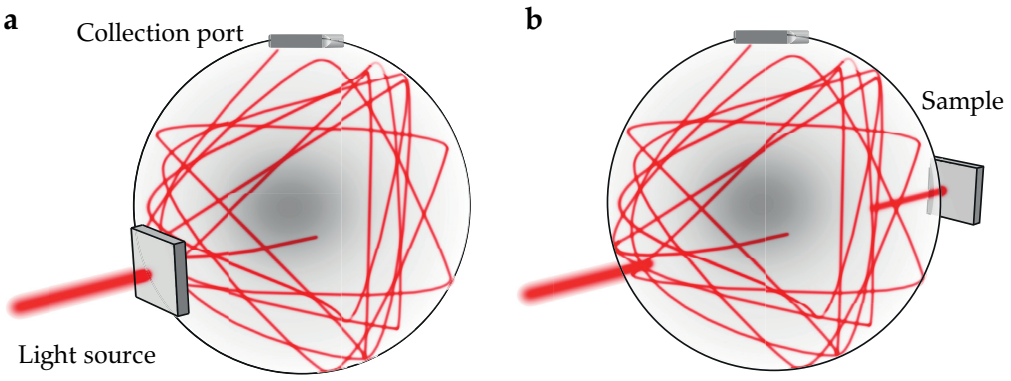

Figure 11 | Schematics of the integrating sphere setup. Total transmission and total reflection setups are represented in **a)** and **b)**, respectively. The signal, reflected by the coating of the inner surfaces, is acquired from the collection port located in the upper hemisphere of the instrument.

the integrating sphere (Labsphere) and then acquired by a 600 µm core fibre (Thorlabs FC-UV600-2-SR) connected to a spectrometer (Avantes HS2048).

As shown in Figure 11, the integrating sphere also allows measuring the total reflection (R) of a system. Combining total reflection and transmission measurements is of particular interest for absorbing systems; indeed, the absorbance (A) can be retrieved from the simple relation $1 = R + T + A$.

The acquired signal was normalised to the intensity of the incident light for both total transmission and reflection. All measurements were recorded using unpolarised light and with an integration time equal to 2 s. Ten spectra were taken for each sample and averaged to reduce the signal-to-noise ratio.

2.1.3 *Goniometry*

Subsection 2.1.2 described how to quantify the scattering efficiency of a system. To further characterise a disordered material, it is important to compare how it angularly re-distributes scattered light compared to an ideal, Lambertian diffuser [74]. The angular distribution of scattered light by a Lambertian diffuser has a cosine dependence on the scattering angle, implying that the appearance of the diffuser does not depend on the observation angle. This property is therefore very desirable for many applications, e.g., paints and cosmetics. Moreover, as discussed in

Chapter 1 (cf. Equation 26), the angular distribution of reflected light can be used to estimate the extrapolation length experimentally, that is necessary to quantify the mean free path rigorously.

The angular distribution of reflected/transmitted light shown in Chapter 5 was determined using a goniometer. In particular, the experimental setup is a simplified configuration of that shown in Figure 10. More in detail, being interested in an incoherent signal, the laser source was replaced by a Xenon lamp (Ocean Optics HPX-2000) coupled into an optical fibre (Thorlabs FC-UV100-2-SR) and directly shone onto the sample. The polarisation optics in Figure 10 was simplified to a linear, cross-polarisers configuration. This configuration allows to filter out the substrate contribution without affecting the signal from the sample — due to the randomisation in the polarisation introduced by multiple scattering [4]. Filtering out the substrate contribution is justified by Lambert's theory [74], where the distribution of reflected intensity arises exclusively from the photons scattered multiple times in the sample.

The illumination angle was fixed at normal incidence, and the angular distribution of intensity was acquired by rotating the detector arm around the sample with a resolution of 1°. To detect the signal, a 600 µm core fibre (Thorlabs FC-UV600-2-SR) connected to a spectrometer (Avantes HS2048) was used. The spectra were averaged over ten acquisitions to reduce the signal-to-noise ratio.

2.2 NUMERICAL METHODS

2.2.1 *Monte Carlo simulations of anisotropic multiple light scattering*

Monte Carlo methods are a class of numerical algorithms using random numbers to solve a specific problem. In particular, Monte Carlo techniques find extensive use in numerical integration — because a definite, multidimensional integral can be solved by evaluating the integrand over a set of random sampled points [88]. The equations describing multiple scattering can be formulated in the integral form (cf. Equations 37 and 38 in Chapter 1), therefore making Monte Carlo simulations well suited for describing light propagation in disordered

media. In particular, Monte Carlo simulations have been extensively used both to investigate theoretical aspects of anisotropic diffusion [63, 89–93], and to accurately describe experimental results regarding light propagation in anisotropic media [64, 94, 95].

The algorithm used in Chapter 3 to simulate photons propagation in the *Cyphochilus*' scales is constructed as following (cf. Appendix a) :

- The photon penetrates the material ballistically until it reaches the first scatterer, whose position is determined according to a negative exponential distribution.
- The position of the next scattering event is determined by a random step, whose direction is sampled on the surface of a unit sphere. The cartesian components of the random step were inverse-sampled from two different negative exponential distributions — with mean ℓ_{xy} and ℓ_z for the in-plane and out-of-plane components, respectively.
- Step 2 is repeated until the photon reaches one of the two interfaces of the material ($z = 0$ and $z = thickness$). Here, if the photon is reflected back in the material, the random walk continues as indicated in step 2 otherwise its contribution to the CBS is computed.
- The procedure is repeated for a new photon until the maximum number of photons is reached.

The anisotropy of the system, introduced in step 2, is modelled as an anisotropic propagator between two scattering events. Each of the scattering centres is, for simplicity, considered as a Rayleigh scatterer with an isotropic angular cross section.

The angular component of each of the random steps was sampled from a distribution of points uniformly distributed on the surface of a unit sphere applying the following variable transformation [96, 97]:

$$\begin{aligned} x &= \sqrt{1-u^2}\cos\theta, \\ y &= \sqrt{1-u^2}\sin\theta, \\ z &= u, \end{aligned} \tag{45}$$

where $u = \cos(\phi)$, $\theta = [0, 2\pi)$ and $u = [-1, 1)$. This step is crucial, because selecting θ and ϕ from uniform distribution ($\theta = [0, 2\pi)$ and

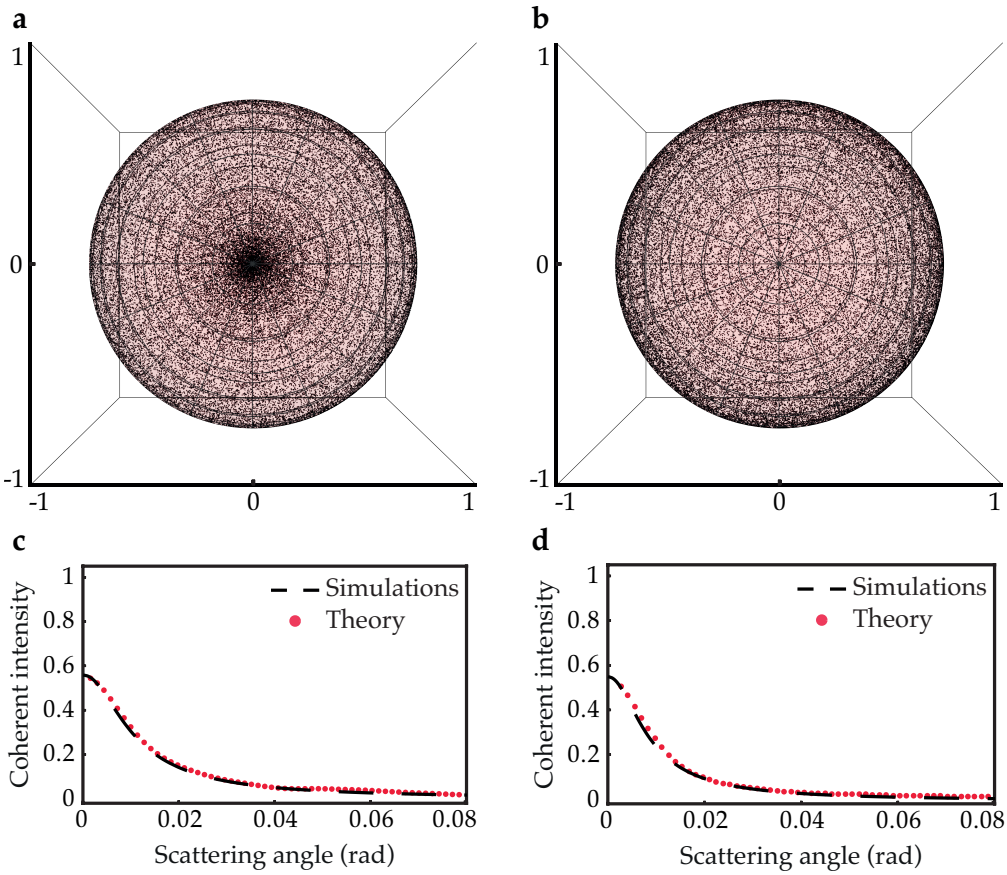

Figure 12 | Uniform point sampling on a unit sphere. a) Angular distribution of points by sampling θ and ϕ from uniform distributions. The points distribution results to be not uniform. **b)** Angular distribution of points by sampling θ and ϕ as described in the MC code. **c)** Comparison of the MC simulations with the isotropic theory without considering internal reflections. Parameters used: optical thickness $= 4$, mean free path = 5µm. **d)** Comparison of the MC simulations with the isotropic theory. Parameters used: optical thickness $= 4$, mean free path $= 5\mu m$, $R = 0.32$ (i.e., $z_e = 1.29$).

$\phi = [0, \pi)$) results in over-sampling over the poles of the unit sphere, as shown in Figure 12a-b. This is a consequence of the dependency of the area element on ϕ ($d\Omega = sin\phi d\theta d\phi$), and would have affected the CBS line shape by biasing the random walk.

The collection of the initial and final positions of the walkers that escaped the material from the same face they entered it — i.e., reflected photons — was then used to reconstruct the CBS line shape (γ_c in Appendix a). Summing up the contribution of each photon, weighted by $exp(-c/\gamma_z) * (1 - R_{avg})$ (where γ_z is the z-component of the mean free path), is equivalent to compute the integral formulation of the coherent bistatic coefficient introduced in Equations 37 and 38 (cf. Chapter 1). The effect of residual absorption on the CBS line shape is not considered, due

to the negligible absorption of chitin for visible wavelengths [17]. The accuracy of the Monte Carlo simulations was verified in Figure 12c-d against the isotropic theory (Equation 40).

2.2.2 *Generation of 2D, disordered structures*

Chapter 4 presents a numerical investigation to understand the importance of anisotropy in scattering optimisation. Two different algorithms were developed to disentangle the role of structural (i.e., in the position of the scatterers) and form (i.e., in the shape of the scatterers) anisotropy:

1. An inverse-design approach was exploited to generate disordered structures with tailored structural correlations. This algorithm consists of two main parts:
    - First, hard (non-overlapping) particles were added using a random sequential approach until the desired filling fraction was reached;
    - Second, the difference between the targeted S(q) and the one of the structure was minimised. In detail, the positions of the particles were gradually changed following a gradient descending minimisation protocol.
2. In the case of an anisotropic form factor, the open-source Python package *Shapely* was used to assure that the particles were not overlapping [98].

2.2.3 *Finite difference time domain (FDTD)*

The simulations presented in Chapters 4 and 6 were performed using LUMERICAL 8.18 (Lumerical Solutions Inc., Vancouver, BC, Canada), a commercial-grade software using the finite-difference time-domain (FDTD) numerical method. This technique solves Maxwell's equation by calculating derivates via finite differences on a space and time grid [99].

A schematic of the simulation setup employed in this work is presented

These boundary conditions well represent slab geometry systems and films.

in Figure 13. Periodic boundaries conditions in the Y direction, i.e., perpendicular to the light beam, and perfect matching layer (PML) boundaries in the X direction were used in all the calculations. The excitation source was set as a plane wave. The simulations were performed in a purely 2D geometry and their numerical stability/convergence was ensured by choosing an adequate simulation time and boundary conditions — assuring that the electric field in the structure decayed before the end of the calculation and that all the excitation light was either reflected or transmitted.

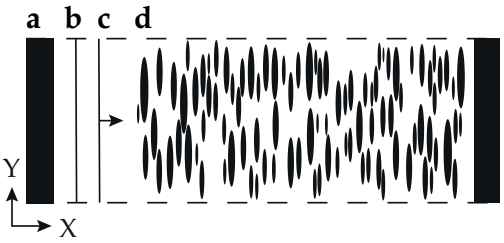

Figure 13 | Schematics of the simulation setup. a) PML boundary conditions, **b)** reflection monitor, **c)** plane wave source, **d)** periodic boundary conditions.

Each of the presented curves was obtained averaging the optical simulations of seven different realisations of ensembles of particles with identical parameters. These different realisations can be obtained by fixing the values of *indexMin* and *indexMan* of the code presented in Appendix b.

Part II

UNDERSTANDING NATURE

3

COHERENT BACKSCATTERING BY AN ANISOTROPIC, BIOLOGICAL NETWORK

Declaration: The work presented in this chapter was published in: G. Jacucci, O. D. Onelli, A. De Luca, J. Bertolotti, R. Sapienza, and S. Vignolini. *Coherent backscattering of light by an anisotropic biological network*, Journal of the Royal Society Interface Focus **9** (2018) [100].

Chapter 1 illustrated that an object is opaque white when the light incident on it undergoes multiple scattering events before exiting the medium, i.e., when the object is optically thick. Commonly, the mean free path is of the order of tens of micrometres in low refractive index, white materials. Therefore, opacity is only achieved for thicknesses of the order of hundreds of micrometres.

Nature, however, provides a striking example of brilliant, white appearance obtained in sub-ten micrometre thickness: the disordered network inside the scales covering the exoskeletons of the *Cyphochilus* beetles. This anisotropic, fibrillar network is particularly interesting for the study of disordered systems as it exhibits the lowest mean free path observed in biological materials thus far.

This chapter reports a technique to determine the mean free path components, and therefore its anisotropy, without varying the thickness or the orientation of a system. This is achieved by combining a coherent backscattering measurement with anisotropic Monte Carlo simulations, introduced in Subsection 2.1.1 and Subsection 2.2.1, respectively. This approach provides a more accurate estimate of the scattering properties of the *Cyphochilus* beetle than the results reported in the literature — overcoming the strong thickness dependency of the previously employed experimental techniques.

The following text is divided in two parts: Section 3.1 describes the morphological and optical properties of the *Cyphochilus* beetle;

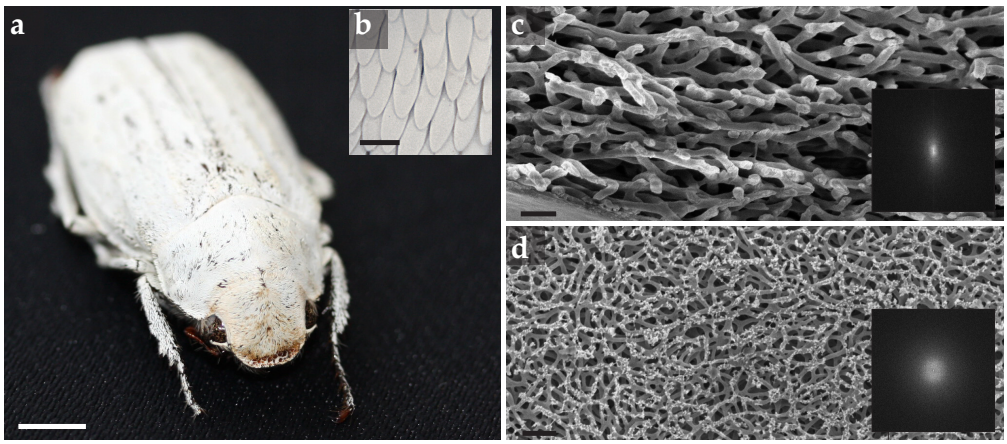

Figure 14 | Images of a white beetle at different magnifications. a) photograph of a specimen of *Cyphochilus* genus beetle ; **b)** micrograph of the organisation of the scales; **c-d)** SEM images of a *Cyphochilus*' scale from a cross section and top view, respectively. Insets show the fast Fourier transforms of the SEM images, which show the orientational anisotropy of the network. Scale bar: 1 cm for a, 300 µm for b, 1 µm for c, 2 µm for d. SEM images courtesy of Dr. Olimpia Onelli.

Section 3.2 presents the combination of experimental and numerical techniques used to determine its scattering efficiency.

3.1 THE *cyphochilus* BEETLE — A BIOLOGICAL EXAMPLE OF HIGHLY-SCATTERING MATERIAL

The optical properties of the beetle genus *Cyphochilus* were first studied in 2007 by Vukusic et al. [19]. The exoskeleton of this white beetle is covered by a single layer of scales, Figure 14a-b, whose dimensions are about 7 µm in thickness, 250 µm in length, and 100 µm in width [101]. As shown in Figure 14c-d, each scale contains a disordered network of fibres with an anisotropic alignment, i.e., mainly oriented parallel to the surface of the scales. The average radius and length of the fibres are (115 ± 80)nm and (1105 ± 360)nm, respectively [22].

The filling fraction of the network was first estimated, by analysing cross-sectional SEM images, to be around 60 % [21]. However, using two-dimensional images overestimates the real filling fraction, as it accounts for the contribution of fibres on different planes than the cross-sectional cut. Recently, thanks to the three-dimensional reconstruction performed by Wilts et al. [22], a more accurate value of filling fraction has been reported to be 45 %.

In the recent years, the scales of the *Cyphochilus* captured scientists' great attention due to their high scattering efficiency. Figure 15 shows the reflectance of different materials compared to a commercial white diffuser. Surprisingly, the scales of the white beetle reflect 30% more than the filter paper (Whatman No. 1), whilst having a similar refractive index and being about ten times thinner. Furthermore, it is worth noting that refractive index of the network was estimated to be $n \simeq 1.55$. This value was obtained on an etched scale using refractive index matching oils. Although the fibres in Figure 14 are historically referred to as made of chitin [19, 21, 22], a detailed chemical analysis of this anisotropic network is still missing.

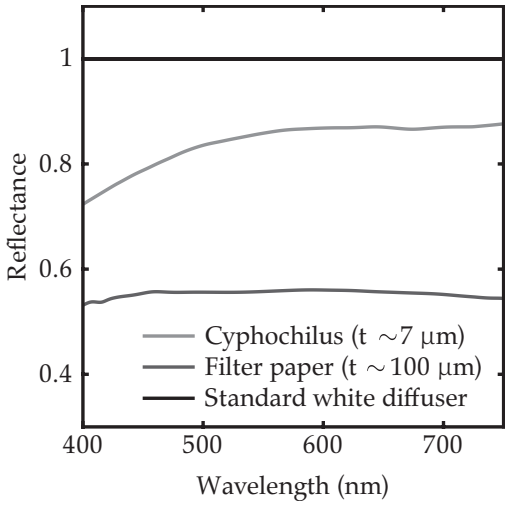

Figure 15 | Reflectance of different low refractive index materials compared to a commercial white diffuser. The value associated to the *Cyphochilus* beetle is significantly higher than that of the filter paper, which is about ten times thicker. The reflectance spectra were acquired with an optical microscope (Zeiss, Axio Scope A1) and using a 50x objective (Zeiss, LD EC Epiplan-Neofluar, NA = 0.85).

The striking scattering strength of the *Cyphochilus*' scales initiated a lengthy debate on the experimental characterisation and theoretical understanding of light transport in this disordered, anisotropic system. In this thesis, both aspects will be discussed and clarified, in Section 3.2 and Chapter 4, respectively.

3.2 QUANTIFYING ANISOTROPIC MEAN FREE PATH VIA MONTE CARLO ANALYSIS OF COHERENT BACKSCATTERING

As discussed in Chapter 1, the scattering efficiency of a system can be quantified in terms of its mean free path. In the recent years, a number of different techniques have been used to characterise anisotropic media; for example, spatially resolved reflectance [90, 94], imaging diffuse transmission [21, 61, 62], spatio-temporal visualisation of transmitted light [102] , and coherent backscattering [64, 95, 103, 104].

The mean free path inside the beetle scales was first estimated by Burresi et al. to be between 0.9 and 1.6 µm [20]. This value, which was measured in the direction perpendicular to the scales' surface, is smaller than the in-plane component [21]. The anisotropy in the mean free path is a consequence of the structural anisotropy in the scales of the beetle and suggests that the network is optimised to increase scattering along the direction perpendicular to the scale's surface. Indeed, the reflectance by an anisotropic system is determined by the transport properties along the direction of propagation of the incoming light (cf. Chapter 1) [57, 66].

The accuracy in determining the in-plane and out-of-plane components of the mean free path in the *Cyphochilus*' scales has been limited by the strong thickness dependency of the experimental techniques used, namely photon lifetime [20] and total transmission [21] measurements. The thickness varies from scale to scale, preventing to obtain an accurate value of mean free path. To further understand the exceptional optical properties of the *Cyphochilus* beetle, the CBS phenomenon was exploited. Indeed, the CBS provides a thickness-independent value for the in-plane mean free path (cf. Chapter 1).

The measured CBS signal is reported in Figure 16. The experimental data show a maximum lower than the theoretical value for semi-infinite media of 1 and a rounded top. This deviation is a consequence of the small thickness of the scales and can be described by the isotropic theory for finite media (Equations 40 and 41). As discussed in Chapter 1, the reduction of the theoretical maximum in finite media is caused by the suppression of long light paths, which are responsible for the formation of the cusp of the CBS profile for semi-infinite media [2] . To accurately determine the mean free path, the effect of the internal reflections at the scale interface on the light path distribution inside the network was accounted in the extrapolation length. Using a filling fraction of $(45 \pm 6)\%$ [22], and by means of Equations 21 to 23, resulted in $n_e = (1.22 \pm 0.03)$, $R = (0.32 \pm 0.04)$, and $z_e = (1.29 \pm 0.11)$. Finally, using the extrapolation length found from the expression above, $\ell_t = (1.4 \pm 0.1)$ µm was obtained from the fit shown in Figure 16.

In the literature, the isotropic theory has been used to obtain information about media where the anisotropy is in the plane perpendicular (xy) to the incoming beam (z-direction) [64, 65]. This type of anisotropy gives

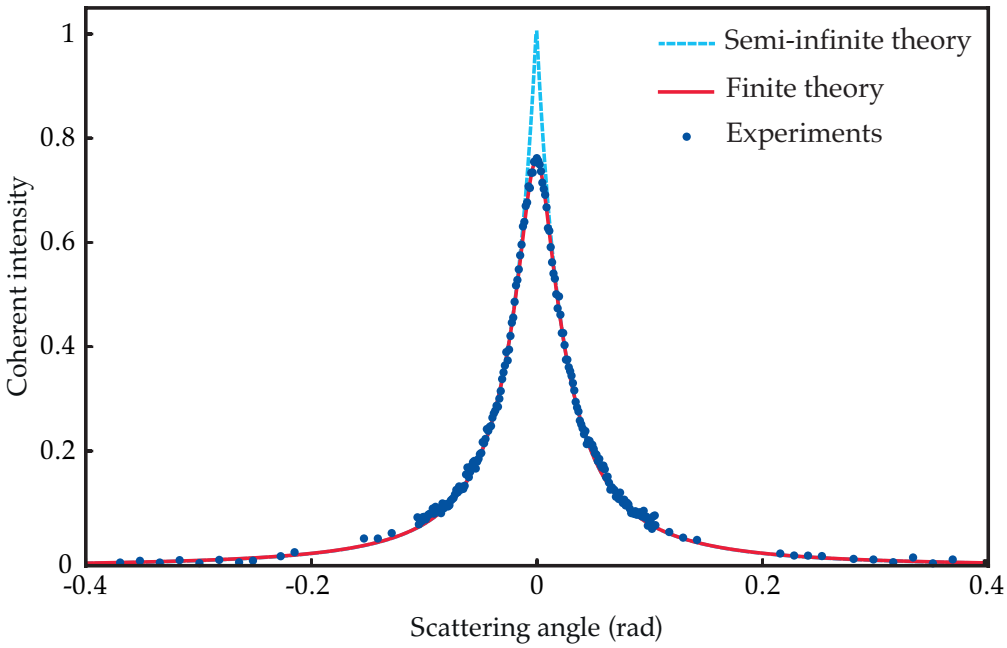

Figure 16 | Fit of the coherent backscattering line shape using the isotropic theory. Theoretical fit of the experimental data (blue dots) using the isotropic theory for semi-infinite (light blue, dashed line) and finite (red, solid line) media. Both curves were normalised to the maximum value of the semi-infinite theory. The experimental points were obtained by normalising the signal measured in the HC configuration to that acquired in the LNC setup (Subsection 2.1.1).

rise to a CBS cone whose line shape differs when acquired along the x and y directions (cf. Chapter 1). In the case of the *Cyphochilus* beetle, the anisotropy is in the xz- and yz-plane (defining z as perpendicular to the surface of the scales) [21, 22] and therefore the resulting CBS profile is isotropic (for light incoming along the z direction). Due to the small thickness of the scales ($\simeq 7\,\mu m$), the probing direction of the incoming beam cannot be changed.

As the anisotropy cannot be investigated directly, anisotropic Monte Carlo simulations for scalar waves were performed to gain insight on the light transport inside the scales (cf. Subsection 2.2.1). The only parameters required for the Monte Carlo simulations are the random steps distribution, the scales thickness and the reflection coefficient at the scale interface (R).

A schematic of the parameters of the simulation is illustrated in Figure 17a. Figure 17b-c show how the CBS line shape is affected both by changing the in-plane (ℓ_{xy}) and out-of-plane (ℓ_z) components of the transport mean free path. In particular, ℓ_{xy} determines the width of the CBS profile, while the optical thickness, defined as $OT = L/\ell_z$ (where

L is the thickness of the medium), specifies the enhancement of the coherent signal.

These results can be qualitatively explained by the fact that the CBS depends only on the distance between the positions of the first scattering event (when the photon enters the medium) and the last (when the photon exits the medium). When a large number of photons is considered, these two positions have on average the same z coordinate (which is of the order of ℓ_z), and therefore their distance can be considered to be z-independent. However, as discussed previously for the isotropic theory, when the optical thickness of the medium is small (i.e., when long light paths are not allowed by the finite thickness of the medium) the top of the CBS is rounded. The limited influence of the optical thickness on the width of the CBS line shape allows the obtainment of a precise value of ℓ_{xy} without requiring samples with different thicknesses.

By fitting the experimental data with the Monte Carlo simulations, it is possible to disentangle the contribution of ℓ_{xy} and ℓ_z to the CBS line shape. In particular, the fit provided a $\ell_{xy} = (1.4 \pm 0.1)$ µm and an optical thickness $OT = (6.7 \pm 0.1)$. The data were fitted by minimising the χ^2. The errors in ℓ_{xy} and OT were estimated by performing simulations were the two parameters were gradually changed, up to the point where the value of χ^2 was 25% larger than the minimum. This procedure was then repeated for taking into account the uncertainty in the determination of reflection coefficient (R).

The measured optical thickness is in good agreement with the total transmission (T) data reported in the literature [20, 21]. Using $T = (0.29 \pm 0.02)$ [20, 21], in Equation 25 and the extrapolation length previously calculated resulted in $OT_{lit} = (6.3 \pm 1.2)$, consistent with the CBS data. From the measured OT and assuming $L = (7 \pm 1)$ µm, where L and its error represent the mean and 1σ of the distribution reported in Reference [21], $\ell_z = (1.0 \pm 0.2)$ µm was obtained. The error in ℓ_z, which is mainly determined by the uncertainty in the thickness of the sample, can be affected by systematic errors given by surface roughness and curvature [4, 105, 106].

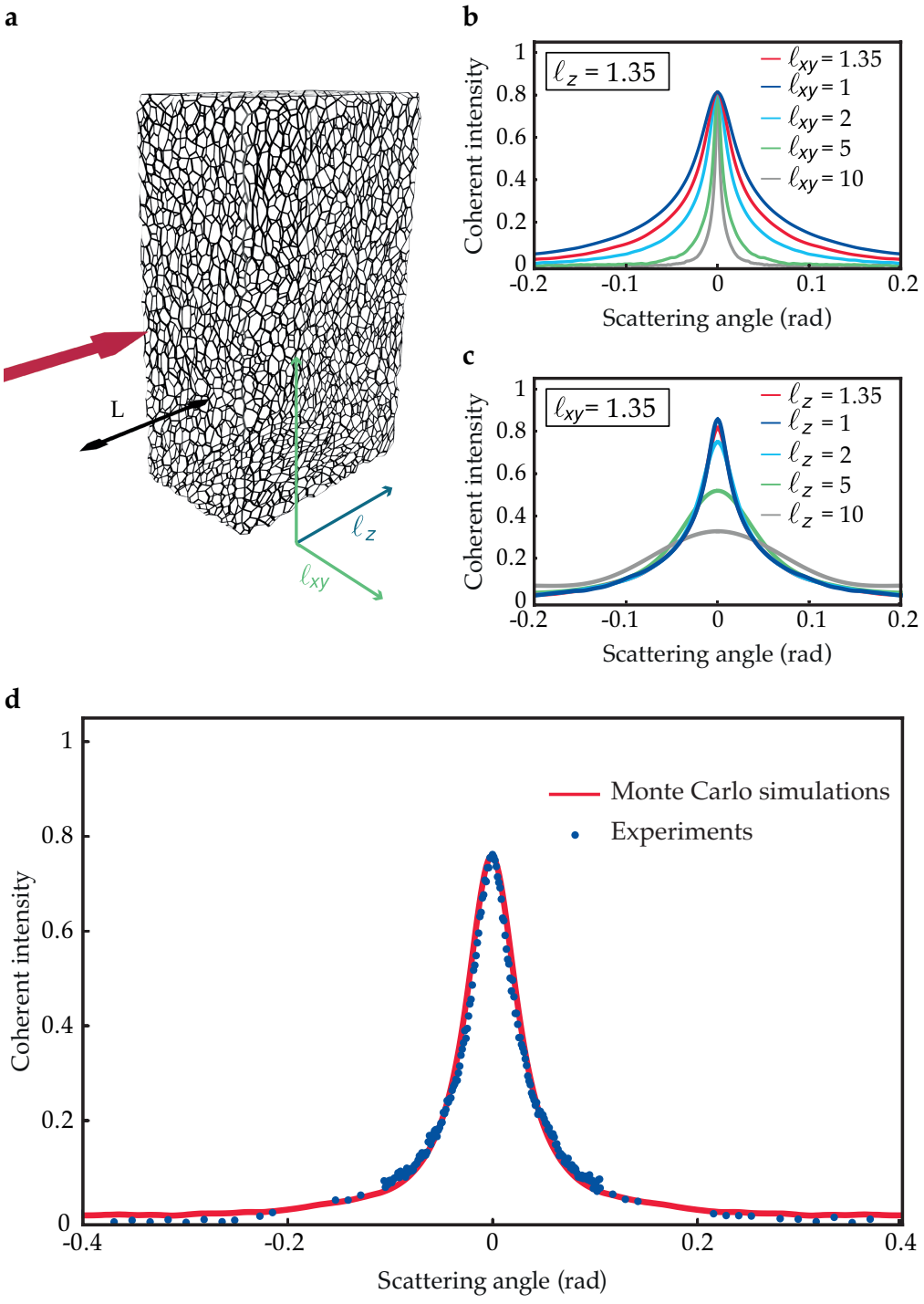

Figure 17 | Monte Carlo simulation of the CBS line shape by an anisotropic medium a) Illustration of the simulation parameters. **b-c)** Varying the in-plane components and the out-of-plane one of the mean free path. For both simulations, the thickness of the slab (L) was fixed at 15 µm. **d)** Fit of the experimental data with the anisotropic simulation. All the simulation were performed using 1 million photons. The simulated curves were normalised to the maximum value of a simulation with OT = 1000.

Comparing ℓ_z with ℓ_{xy}, the measured optical anisotropy (OA) is:

$$\mathrm{OA} = \frac{\ell_{xy} - \ell_z}{\ell_{xy}} = (0.27 \pm 0.13). \tag{46}$$

This experimental result is in agreement with the 3D reconstruction of the anisotropic network reported in Reference [22], which predicts $\mathrm{OA} \simeq 0.35$.

3.3 CONCLUSIONS

This chapter reported important results in the understanding of light propagation in the disordered network inside the *Cyphochilus*' scales. It was demonstrated that the mean free path and the optical anisotropy in the scales of the beetle can be determined by combining a coherent backscattering measurement with anisotropic Monte Carlo simulations. Exploiting the coherent backscattering phenomenon provides an accurate evaluation of the in-plane transport mean free path without requiring samples with different thicknesses, in contrast with other static and easily accessible techniques. Moreover, the presented methodology estimates the anisotropy of a system without the need to change its orientation or its thickness — therefore allowing to measure the optical anisotropy of the Cyphochilus' scales accurately.

4

LIGHT PROPAGATION IN ANISOTROPIC, DISORDERED MEDIA: A NUMERICAL STUDY

Declaration: The work presented in this chapter was published in: G. Jacucci, J. Bertolotti, and S. Vignolini. *Role of anisotropy and refractive index in scattering and whiteness optimization*, Advanced Optical Materials 7 (2019) [107].

Does the anisotropy observed in Chapter 3 play a role in scattering optimisation, or is it a coincidence of the biological process behind the formation of the *Cyphochilus*' scales?

This chapter presents a numerical model to investigate the role of anisotropy in scattering optimisation. The effect of structural and single-particle anisotropies on the opacity of materials are discussed and the criteria to improve scattering over an ample parameter space, including filling fraction and refractive index, are identified.

The following text is divided into two sections: Section 4.1, where the importance of different kinds and degrees of anisotropy on the opacity of a system is investigated; Section 4.2, where ensembles of particles with optimised anisotropy are compared in terms of their scattering strength and whiteness.

4.1 STRUCTURE AND FORM ANISOTROPY

The scattering strength of a system depends on (i) single-particle properties as size, shape, and refractive index, (ii) ensemble properties as filling fraction and structural correlations (cf. Chapter 1). An inverse design algorithm was developed to disentangle the effect of anisotropy on single-particle (form factor, Equation 9) and ensemble properties (structure factor, Equation 31). This numerical algorithm generates systems with tailored form and structure factor (details are reported

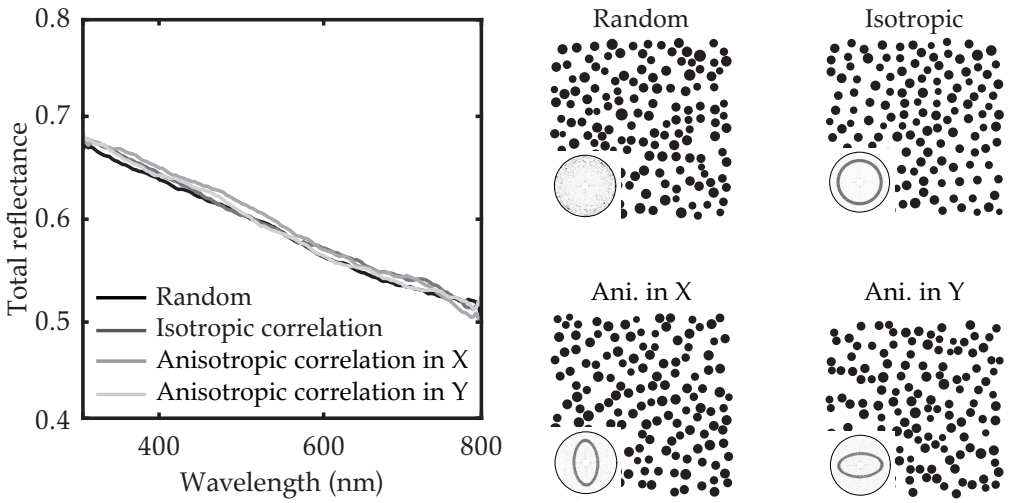

Figure 18 | Simulated optical response for systems with different structural anisotropy. The structure factor relative to each ensemble of particles is shown as an inset. An anisotropic $S(\mathbf{k})$ does not affect the broadband reflectivity of a system. All the simulated structures have a thickness of $10\,\mu m$, $ff = 0.3$, building blocks with $n = 1.55$, $r = 250\,nm$ and 20% polydispersity. This radius represents the optimal one for isotropic, $c = 1$, scatterers (cf. Table 6). The total reflectance was acquired over all reflection angles.

In this thesis random indicates an ensemble of particles whose $S(\mathbf{k})$ results from the random sequential addition of hard disks. The other systems are generated via an inverse design approach (cf. Subsection 2.2.2).

in Subsection 2.2.2 and Appendix b). In particular, to establish a comparison over a large parameter space whilst avoiding computational burden, two-dimensional, disordered media were investigated.

Figure 18 shows the effect of an anisotropic structure factor on the scattering strength of a system. More in detail, ensembles of isotropic particles with the same filling fraction, but different structure factor were compared. The size of the particles was sampled from a Gaussian distribution with mean $r = 250\,nm$, which is the optimal value for isotropic particles with a refractive index of $n = 1.55$ (Table 6, Appendix c). The size distribution has a polydispersity of 20%, defined as the ratio between the standard deviation and the mean of the Gaussian distribution. The presence of polydispersity does not affect the whiteness of a system and better describes experimental systems (cf. Appendix c.1, Appendix c).

The simulations provided in Figure 18 deliver two important results: First, for $n = 1.55$, increasing the structural correlation of a system (i.e., from random to isotropic) did not improve the scattering strength. Second, introducing anisotropy in the structure factor did not alter the optical response of an ensemble of isotropic scatterers.

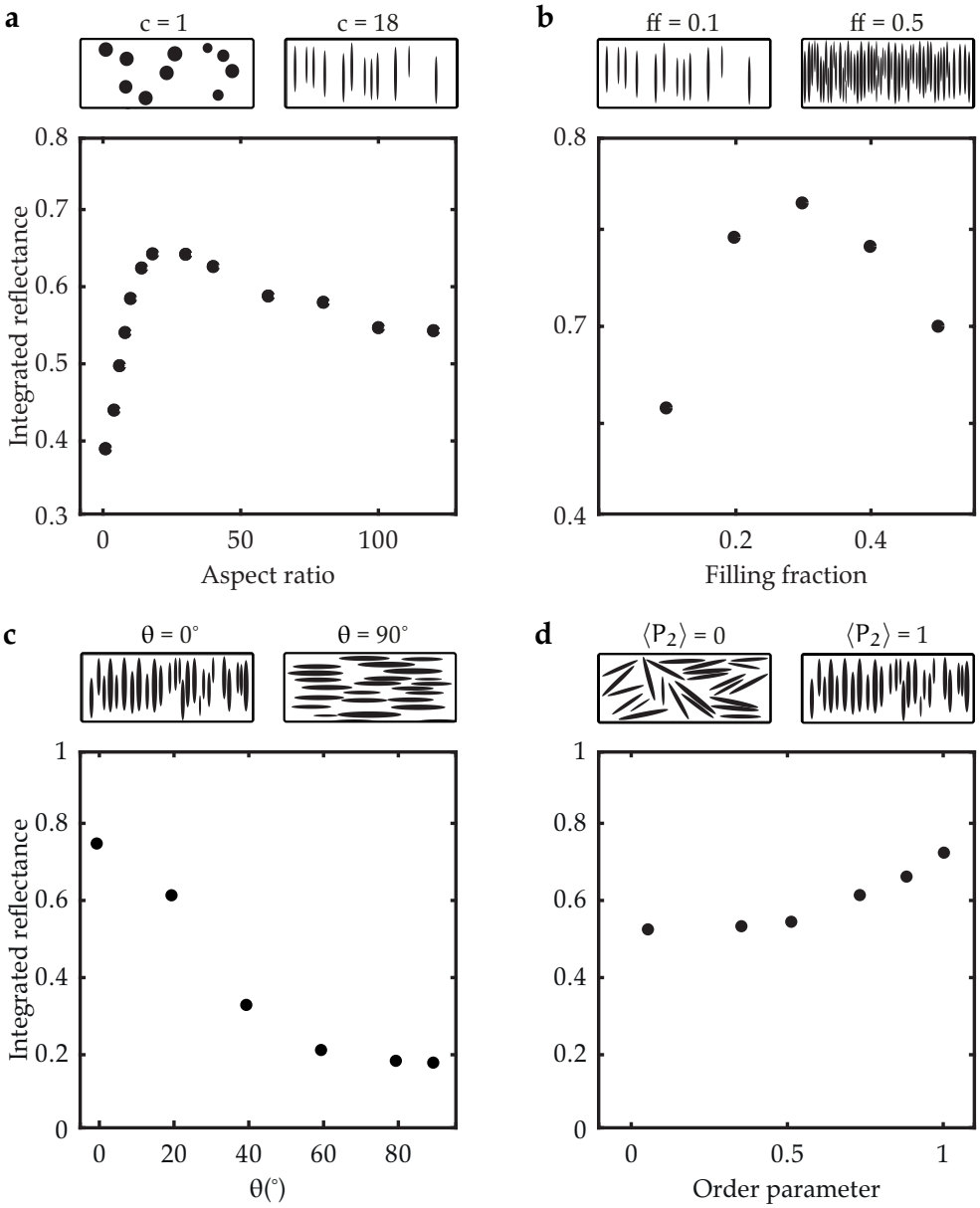

Figure 19 | Numerical procedure to determine the single-particle and orientational parameters which maximise scattering. a&b) Simulated optical response for systems with different form anisotropy. Integrated reflectance over the visible range as a function of the: a) aspect ratio of the particles for systems with $ff = 0.1$; b) filling fraction of ensembles of scatters with $c = 18$. **c&d)** Simulated optical response for systems with different kinds and degrees of orientational, form anisotropy. Integrated reflectance over the visible range as a function of the: c) angle between the director and the direction perpendicular to the incoming beam (θ); d) order parameter ($\langle P_2 \rangle$). The amount of light reflected is maximised for ensembles of anisotropic particles oriented perpendicular to the incoming beam ($\theta = 0$) and with maximum orientational anisotropy ($\langle P_2 \rangle = 1$). All the structures have a thickness of $10\,\mu m$ and building blocks with $n = 1.55$, $r = 250\,nm$ and 20% polydispersity.

In contrast, a change in the form factor of the particles drastically affects the response of a system (Figure 19 and Table 6, Appendix c). First,

particles with a different aspect ratio (c) but the same area (parametrised via r_0, i.e., the radius at $c = 1$) and same orientation (perpendicular to the incoming beam) were considered to identify the optimal shape of the scatterers. Figure 19a shows that tuning the aspect ratio of the particles leads to a marked change in the scattering efficiency of a medium, with a maximum at $c = 18$ for $r_0 = 150\,nm$. Second, after identifying which aspect ratio maximises the reflectance, the number of particles in the system was varied to optimise the filling fraction (Figure 19b).

The use of anisotropic particles adds an extra parameter in determining the optical properties: their degree of alignment. This additional degree of freedom was accounted for by defining the director $\mathbf{n}$ — in analogy to the literature of liquid crystals [108] — as the average orientation of the particles, i.e., θ. The degree of alignment can be consequently determined through the order parameter ($\langle P_2 \rangle$) [108]:

$$\langle P_2 \rangle = \left\langle \frac{3\cos^2\phi - 1}{2} \right\rangle, \tag{47}$$

where ϕ is the angle between the long axis of a given particle and $\mathbf{n}$ and $\langle ... \rangle$ denotes ensemble average. Following this definition, $\langle P_2 \rangle = 1$ describes and ensembles of particles perfectly aligned along $\mathbf{n}$ (maximum anisotropy) and $\langle P_2 \rangle = 0$ a completely random orientation (isotropic).

Figure 19c&d summarise the role of the alignment of the particles on the scattering properties of a system. Figure 19c compares particles with $\langle P_2 \rangle = 1$ but different orientation of the director. The reflectance is maximised when the director is aligned perpendicular to the incoming light ($\theta = 0$). Moreover, maximising the degree of orientational anisotropy improves the scattering efficiency of a system (Figure 19d).

In this regard, it is important to note that the simulations presented in this chapter are two-dimensional. Therefore, the polarisation is in the plane of incidence (Figure 13). In isotropic, disordered systems the incident light is quickly depolarised due to multiple scattering [4]. However, in three-dimensional ensembles of anisotropic scatterers with orientational alignment, the polarisation might be more resilient to multiple scattering. In this case, it might be necessary to consider an extra parameter in the scattering optimisation problem.

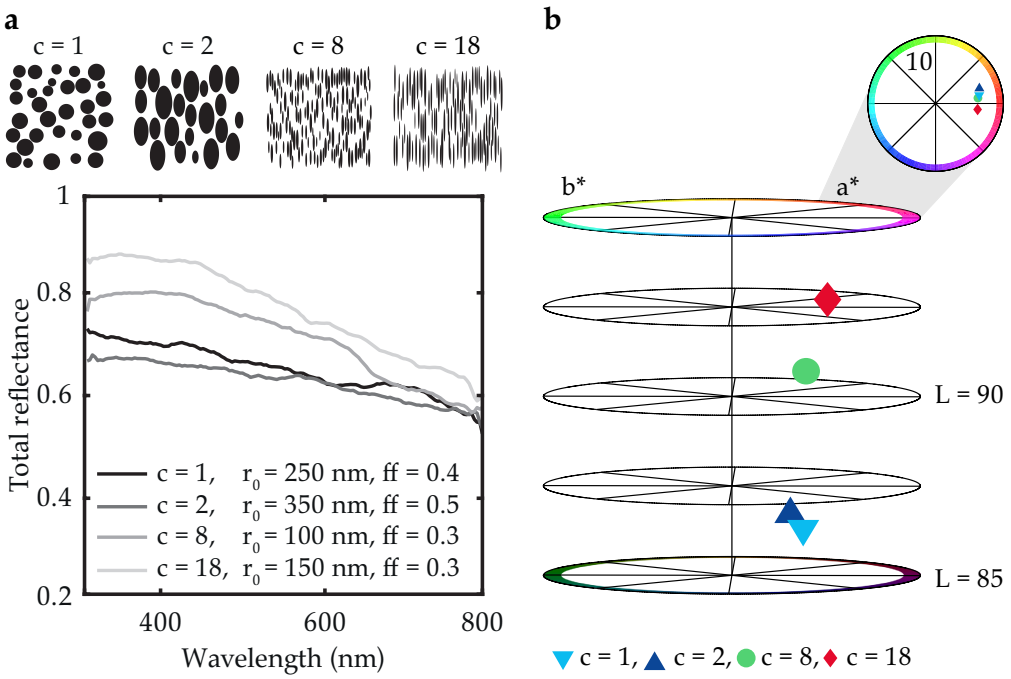

Figure 20 | Scattering and whiteness maximisation for low refractive index media. **a)** Simulated optical response of structures with the best filling fraction (ff) and aspect ratio for different size of the particles (r_0). r_0 corresponds to the radius of the particles at $c = 1$. The best reflectance was obtained for anisotropic scatterers ($c = 18$) and a low filling fraction ($ff = 0.3$). All the structures had a thickness of 10 µm and a 20% polydispersity in the size distribution of their building blocks, whose refractive index is $n = 1.55$. The total reflectance was acquired over all reflection angles. **b)** Polar plot showing the CIELAB colour space coordinates (cf. Appendix c) of the spectra in a).

4.2 LIGHT SCATTERING OPTIMISATION

4.2.1 *Low refractive index systems*

The results illustrated in Figure 19 refer to particles having $r_0 = 150\,nm$ and $n = 1.55$. The same procedure was applied for scatterers with different sizes, and their optimised values of aspect ratio and filling fraction are reported in Figure 20. The details of the optimisation procedure can be found in Table 6, Appendix c.

Notably, ensembles of low refractive index, anisotropic particles ($c = 18$) exhibit a marked broadband increase in scattering efficiency — they reflect almost 20% more of the incident light compared to optimised, isotropic systems. In addition, anisotropic systems require 25% less material to maximise scattering, from $ff = 0.4$ to $ff = 0.3$.

n	$r_0(nm)$	c	ff	W
1.55	100	8	0.3	88
1.55	150	18	0.3	90
1.55	250	1	0.4	85
1.55	350	2	0.5	85
2.60	50	500	0.2	91
2.60	100	1	0.3	90

Table 1 | Whiteness value for low and high refractive index media. Parameters which maximise whiteness (W, Equation 48) for ensembles of particles with different sizes (r_0, i.e., the radius at $c = 1$), refractive index (n), but same thickness ($t = 10\,\mu m$). Anisotropic, low refractive index, particles show a whiteness comparable to that of high refractive index systems.

The optimal value of aspect ratio obtained in Figure 20 is in good agreement with the one reported for the *Cyphochilus* beetle, where $c \simeq 10$ [22]. However, it is important to note that Reference [22] does not claim that the size of the fibrils in the biological network is optimised. Moreover, recent three-dimensional modelling confirmed that $ff = 0.3$ represents the optimal filling fraction for anisotropic, low refractive index networks [9, 109].

To evaluate the efficiency of the anisotropic systems in making visually white materials, Table 1 reports the whiteness values for the spectra in Figure 20a. The whiteness is determined not only by the amount of light reflected by a system but also by its spectral dependency. In detail, to quantify this parameter, the reflectance spectra were converted in CIELAB colourspace coordinates (cf. Appendix c). Figure 20b shows the colour space representation of the spectra in Figure 20a. According to Table 1, ensembles of low refractive index, anisotropic particles outperform their isotropic counterparts in terms of whiteness.

4.2.2 *High refractive index systems*

The role of the refractive index on the scattering properties of anisotropic systems was investigated by repeating the procedure presented in Section 4.1 and Subsection 4.2.1 for $n = 2.60$. This value of refractive corresponds to the rutile phase of TiO_2 [13], currently the favoured product in the industrial fabrication of white materials.

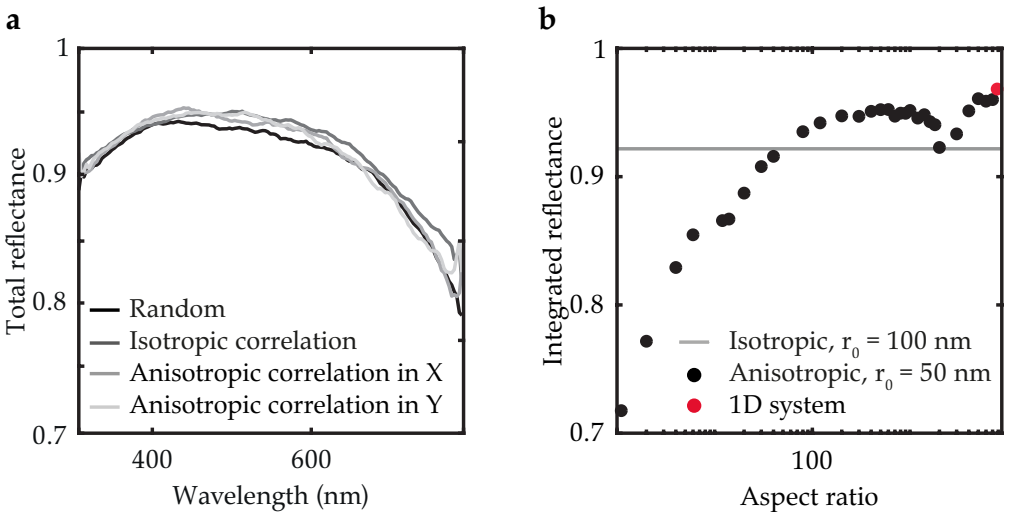

Figure 21 | Numerical procedure to determine the structural and single-particle parameters maximising scattering for high refractive index systems. a) Simulated optical response for systems with different structural anisotropy. The systems had $ff = 0.25$, building blocks with $n = 2.60$ and radius sampled from a Gaussian distribution with mean $r = 100\,nm$ and 20% polydispersity. This radius represents the optimal one for isotropic, $c = 1$, scatterers (cf. Table 7). **b)** Integrated reflectance over the visible range as a function of the aspect ratio of the particles for systems with $ff = 0.1$. Anisotropic systems outperform the scattering efficiency of ensembles of optimised isotropic particles only for aspect ratios larger than 40. At large aspect ratios, the systems approach the one-dimensional limit and a further increase in the integrated reflectance is observed. All the structures had a thickness of $10\,\mu m$ and scatterers oriented perpendicular to the incoming light ($\langle P_2 \rangle = 1$). The total reflectance was acquired over all reflection angles.

Figure 21a shows that similar to what is reported in Reference [110], a small increase in the reflectance is observed in high refractive index systems with structural correlation. As in the case of low refractive index media (Figure 18), introducing an anisotropic $S(\mathbf{q})$ did not affect the optical properties.

Interestingly, for high refractive index, anisotropic systems outperform ensembles of optimised isotropic particles only for aspect ratios larger than 40 (Figure 21b). Moreover, Figure 21b shows that after exhibiting a steady growth as a function of the aspect ratio, between $c \simeq 400$ and $c \simeq 1400$ the integrated reflectance shows a less marked dependence on c, with a maximum value at $c \simeq 500$.

At even higher aspect ratios the systems approach the one-dimensional limit (i.e., particles as long as the lateral dimension of the material) where a further increase in the integrated reflectance is expected — 1D, disordered systems are able to act as perfect mirrors [111, 112].

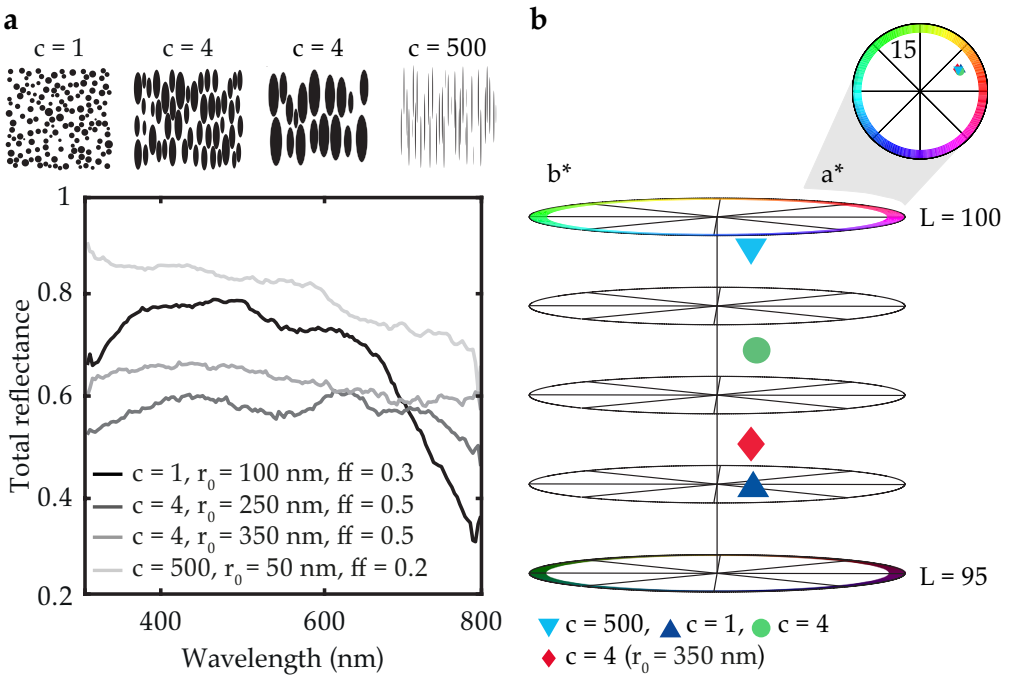

Figure 22 | Scattering and whiteness maximisation for high refractive index media. **a)** Simulated optical response of structures with the best filling fraction (ff) and aspect ratio (c) for different size of the particles (r_0). The best reflectance was obtained for anisotropic scatterers ($c = 500$) and a filling fraction $ff = 0.2$. All the structures had a thickness of $10\,\mu m$. The total reflectance was acquired over all reflection angles. **b)** Polar plot showing the CIELAB colour space coordinates (cf. Appendix c) of the spectra in a).

Similarly to what shown in Figure 20 for $n = 1.55$, Figure 22 compares the results of the optimisation procedure for different size of high refractive index scatterers (details in Table 7, Appendix c). The predicted optimal values of radius ($r_0 = 100\,nm$) and filling fraction ($ff = 0.3$) for isotropic systems with $n = 2.60$ are in agreement with those reported in theoretical and experimental studies regarding TiO_2 particles [110, 113–116].

Table 1 reports the whiteness values of the spectra in Figure 22. Although increasing the refractive index leads to an increase in reflectance, the whiteness is almost unaffected. Indeed, media with $n = 2.60$ exhibit a more saturated response, i.e., larger values of a^* and b^* (cf. inset of Figure 22b). Therefore, low refractive index systems achieve a whiteness comparable to that of high refractive media whilst having a smaller brightness (i.e., smaller L^*).

4.3 CONCLUSIONS

In this chapter, numerical simulations have been exploited to study light propagation in anisotropic media. The use of an inverse design algorithm allowed to disentangle the role of different types and degrees of anisotropy in the optical properties of a system. This chapter showed that anisotropic particles, aligned perpendicular to the exciting light ($\theta = 0$, $\langle P_2 \rangle = 1$), increase the scattering efficiency of disordered systems, disregarding of their structural correlations and refractive index. In particular, ensembles of anisotropic, low refractive index, particles outperform those of their isotropic counterparts both in terms of reflectance (with 20% increase over the visible range) and whiteness (90 against 84). This value of whiteness is comparable to the one for high refractive index systems ($n = 2.60$). Besides, for low refractive index media, introducing anisotropic scattering elements decreases the amount of material required to maximise scattering of 25%; $ff = 0.3$ compared to $ff = 0.4$ in the isotropic case.

In conclusion, these results suggest an explanation for why nature exploits anisotropic systems to achieve lightweight, highly-scattering structures. Moreover, they demonstrate the importance of anisotropy in maximising the optical response of low refractive index media. The understanding provided by the theoretical investigation of this chapter unveils novel concepts to fabricate materials with whiteness as high as the industrially available high refractive index nanoparticles while being sustainable and biocompatible.

Part III

FROM NATURE TO APPLICATIONS

5

BIOINSPIRED SCATTERING NETWORKS

Declaration: The work presented in this chapter was published in: J. Syurik *, G. Jacucci *, O. D. Onelli, Hendrik Hölscher, and S. Vignolini. *Bio-inspired highly scattering networks via polymer phase separation*, Advanced Functional Materials **28** (2018) [117].

Part II identified the key parameters to obtain a high scattering efficiency in low refractive index systems. Based on these results, this chapter reports an experimental approach to produce bioinspired, white materials. In particular, a phase separation technique is exploited to fabricate porous, polymeric films. Through changing the starting conditions of this self-assembly process, it is possible to tune the morphology of the final system and therefore control its scattering properties.

This chapter is divided into two sections: Section 5.1 where details of the fabrication procedure are reported; Section 5.2 where the scattering properties of the bioinspired networks are characterised.

5.1 POLYMER PHASE SEPARATION

Porous, white films were obtained from polymethyl methacrylate (PMMA) by phase separation in solution. This process has two possible pathways: nucleation and growth and spinodal decomposition [118]. The nucleation and growth process drives to the formation of identically sized pores, whereas spinodal decomposition usually leads to a channel-like structure. Phase separation is a scalable process which is widely used in the production of aerogel materials and membranes [119, 120]. This process is claimed to be behind the formation of the chitin network in the Cyphochilus' scales [109]. However, its application to maximise scattering has been overlooked.

The sample fabrication presented in this subsection was performed by Dr Julia Syurik (Karlsruhe Institute of Technology)

In short, a three-component solution of PMMA (0.6 *wt*%) and water (0.2 *wt*%) in acetone was first prepared (Figure 23). Then, upon solvent (aceton)/nonsolvent (water) evaporation, the solution was demixed into two phases: (i) a polymer-rich phase forming a random network; (ii) a liquid phase, which evaporates at a slower rate leading to the formation of nanoscale pores. This simple assembly process strongly relies on the evaporation kinetics and hence on the composition of the starting solution. Only a small per cent variation in the water content or the molecular weight of the polymer chains greatly affects the assembly. Therefore, to tune the self-assembly, PMMA with a different mass average molar mass (M_w) were prepared via sonication treatment, starting from commercial PMMA with an initial $M_w = 1.86\,\mathrm{MDa}$. The values of M_w were estimated at different stages of sonication using size exclusion chromatography (SEC). As expected [121], M_w gradually decrease with the sonication time — from 1.86 to 0.099 MDa after 7 hours of sonication [117]. The sonicated solutions were used to cast free-standing films, between 10 and 85 µm thick. Acetone is moderately hygroscopic [122], and therefore can potentially attract water in the solution in linear dependence with the duration of the sonication. However, no significant difference in the water content for the non-sonicated and sonicated solutions was revealed via Fourier transform infrared (FTIR) spectroscopy, allowing to estimate the water content in all the solutions to be below 0.2 *wt*% prior to casting [117].

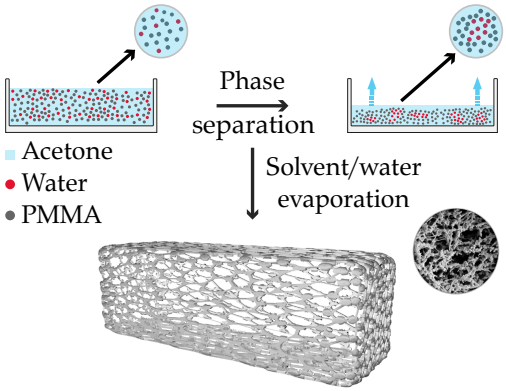

Figure 23 | Fabrication of bioinspired, white films via phase separation. A three-component solution of PMMA and water in acetone is cast under controlled environmental conditions and allowed to evaporate. The solution precipitates into two phases after the quick evaporation of the acetone: (i) a polymer-rich phase, forming the random network; (ii) a liquid water phase. Next, water evaporates, leading to the final porous polymer structure. The round insets show a magnification of the self-assembly steps and an SEM image of the polymer network, respectively.

SEC and FTIR measurements were performed by Dr Julia Syurik (Karlsruhe Institute of Technology). Details can be found in Reference [117].

The scanning electron microscopy (SEM) images reported in Figure 24 reveal the effect of the sonication time on the morphology of the

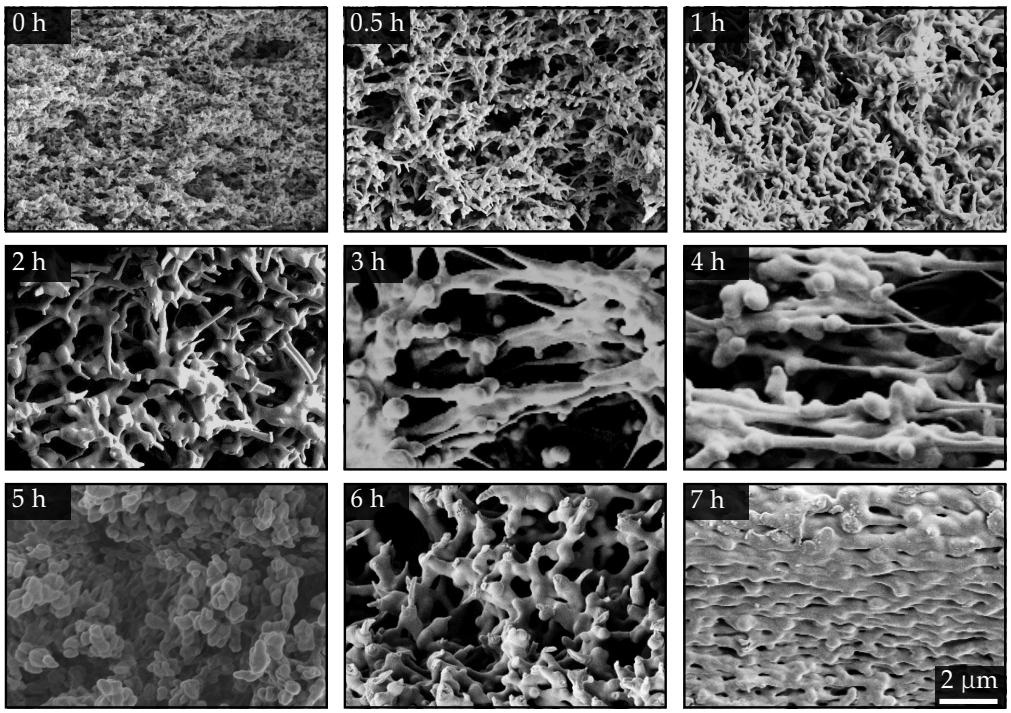

Figure 24 | Effect of the polymer molecular weight on the phase separation. Typical SEM images of the cross-section of porous films obtained by varying the sonication time between 0 and 7 hours. Increasing the sonication time decreases the molecular weight and drastically affects the morphology of the final system. Scale bar: 2 μm for all SEMs.

films. The films obtained from non-sonicated PMMA solution showed a fibrillar network with very low porosity (filling fraction $\simeq$ 75%) and with fibrils below 100 nm in length and 20 nm in width. Increasing the sonication time led to a higher porosity as well as to larger struts, both in length and width. After 1 hour of sonication, the length of the fibrils constituting the network ranged from 500 to 1200 nm in length and between 120 and 300 nm in width. When extending the sonication time to 4 hours, the struts became more elongated with a length of $\simeq$ 4 μm and a thickness of about 300 nm. Lengthening the sonication time even further revealed an opposite trend: the fibrils become smaller and thicker. Finally, the film produced from PMMA sonicated for 7 hours showed a similar morphology to the non-sonicated films, with a PMMA fraction of $\simeq$ 65%.

The morphological data reported in this paragraph were qualitatively estimated from the SEM images.

The change of morphology can be intuitively explained considering that PMMA forms a kinetically stable aqueous bi-phasic system which does not collapse upon complete evaporation of the solvents (i.e., leading to the desired porosity) only for specific values of viscosity, and therefore for a specific interval of molecular weights.

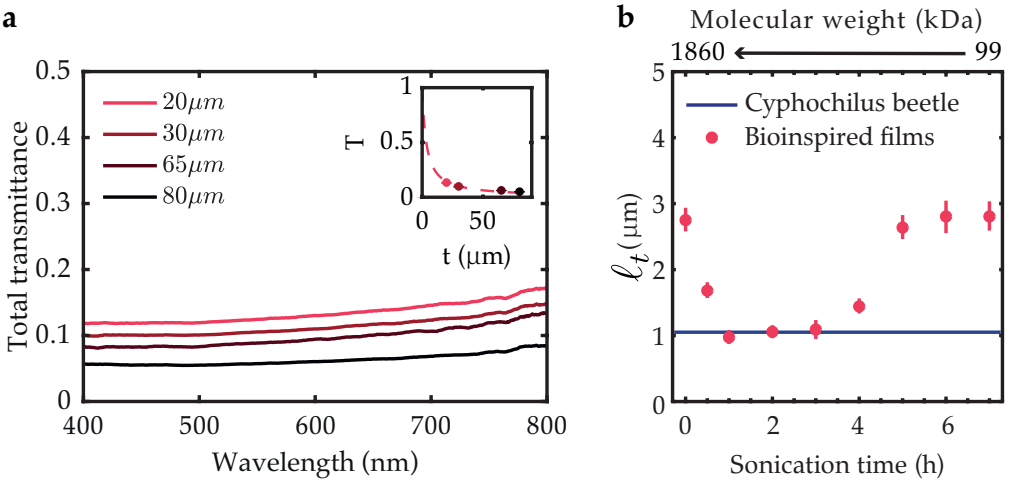

Figure 25 | Scattering strength of bioinspired films. a) Total transmittance as a function of the film thickness after 3 hours of sonication. The inset shows the theoretical fit (dotted line, Equation 25) from which the mean free path (ℓ_t) was extrapolated. **b)** ℓ_t for films obtained after different sonication times (bottom axis), i.e. different molecular weights of the polymer (top axis). The error bars represent the confidence interval of the fit and account for the uncertainty in the extrapolation length. ℓ_t is estimated at 600 nm (wavelength of the impinging light). The mean free path for the *Cyphochilus* is the one reported in Chapter 3.

5.2 OPTICAL CHARACTERISATION

The thickness of the bioinspired films was measured using an incremental probe (MT60 M, Heidenhain) and validated via SEM.

Figure 25 compares the different morphologies presented in Figure 24 in terms of their scattering efficiency. The transport mean free path (ℓ_t, cf. Chapter 1) for different sonication stages was estimated by measuring the total transmission in a series of films with the same morphology but different thickness (Subsection 2.1.2). In detail, ℓ_t was obtained from fitting the transmission behaviour as a function of the thickness using Equation 25, as shown in Figure 25a.

The extrapolation length was determined by fitting the angular distribution of the transmitted light (Figure 26a) with Equation 26 [41]. The fit shown in Figure 26b led to $z_e = (1.5 \pm 0.2)\,\ell_t$. This value of extrapolation length corresponds to a filling fraction comprised between 0.4 and 0.65 — calculated using Equations 21 to 23 — in good agreement with what estimated from Figure 24.

The data reported in Figure 25b are obtained for wavelengths around 600 nm. However, these are representative of the scattering behaviour over the whole visible range as the spectral response of the transmission as a function of the thickness has only a weak, non-resonant, dispersion. The smallest ℓ_t are observed in networks obtained after sonication times

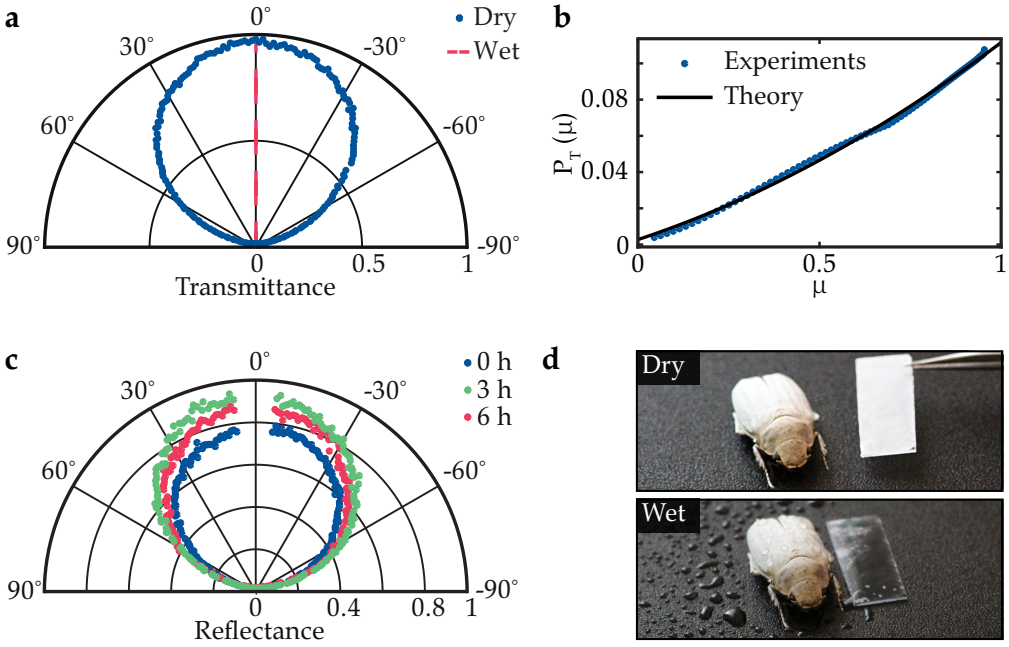

Figure 26 | Angular resolved response and switchable appearance of bioinspired films. a) Angular distribution of the transmitted intensity ($\lambda = 400\,\mathrm{nm}$) through a PMMA film before and after wetting, blue and red circles, respectively. The sample switched from a scattering behaviour to a ballistic regime. Both datasets were normalised against their maxima. **b)** Fit of the angular distribution of transmitted light normalised against the incoming light ($P_T(\mu)$) as a function of the cosine of the transmitted angle (μ). The solid black line represents the theoretical prediction of Equation 26. **c)** Angular distribution of the reflected intensity ($\lambda = 400\,\mathrm{nm}$) by PMMA films at different sonication times and $t = 30\,\mu\mathrm{m}$. The angular range close to the specular angle is left blank due to the mechanical limitations of the experimental setup (cf. Subsection 2.1.3). **d)** Similarly to the *Cyphochilus* beetle, microstructured PMMA films exhibit a bright white appearance achieved by efficient multiple scattering. When wet, water penetrates the polymer film, which turns transparent. In contrast, the beetle retains its whiteness as a continuous surface layer encasing the scales prevents water to index match the scattering network [19]. The film shown is $4\,\mu\mathrm{m}$ thick, and it was cast on a transparent PMMA substrate.

between 1 and 3 hours. Notably, bioinspired networks achieve ℓ_t as small as $\simeq 1\,\mu\mathrm{m}$ — one order of magnitude smaller than that of commercial white paper [20, 123], and comparable to the *Cyphochilus* (cf. Chapter 3) [20, 21].

Although a quantitative comparison between the different morphologies would require further investigation of the three-dimensional structure of the bioinspired networks, the observed trend in the scattering strength can be qualitatively understood in terms of the effect of the molecular weight on the filling fraction of the films (Figure 24).

The scattering properties of the bioinspired materials were further characterised by measuring the angular distribution of the reflected light

(Subsection 2.1.3). Figure 26c shows that the light scattered from the films follows a Lambertian profile, implying that their white appearance does not depend on the observation angle.

Finally, due to their low refractive index and porosity, the produced free-standing films can be easily index-matched with water and other conventional solvents — providing a switchable response which transitions from white to transparent upon wetting (Figure 26a&d). This property adds extra functionality compared to traditional white coatings made of high refractive index components.

5.3 CONCLUSIONS

This chapter presented a scalable route to fabricate highly scattering materials by tuning the morphology of a low refractive index medium. In detail, porous polymeric networks were obtained via phase separation. The scattering strength of these networks was maximised by varying the molecular weight of the polymer. Even though further control over the self-assembly could be obtained by adjusting the amount of water in the initial suspension, already transport mean free paths comparable to that of the *Cyphochilus* were achieved. Moreover, using conventional liquids, it is possible to index-match the bioinspired films providing a fully reversible change of appearance: from white to transparent and vice versa. The combination of a scalable manufacturing technique with the optical functionality of the materials is extremely appealing for the application of these films as functional coatings. In conclusion, this chapter showcases the first example of artificial, low refractive index materials with a scattering strength comparable to that of the biological inspiration presented in Chapter 3.

6

CELLULOSE-BASED WHITE MATERIALS

The polymeric films introduced in Chapter 5 represented the first example of artificial, highly-scattering systems solely made of low refractive index materials. However, despite showing outstanding optical properties, they do not meet the current demand for the production of sustainable and biodegradable white materials. Moreover, the intrinsic complexity and instability of the self-assembly process do not allow to engineer the morphology of the final system.

This chapter, based on the predictions made in Chapter 4, presents an experimental approach where the sizes of the scatterers and the morphology of their assembly can be independently tuned.

The following text is divided into two sections: Section 6.1 describes the experimental procedure to produce cellulose nanoparticles with different dimensions and how to control their assembly; Section 6.2 characterises the scattering properties of the cellulose-based materials.

6.1 CELLULOSE BUILDING BLOCKS FOR LIGHT SCATTERING

Cellulose nanoparticles (CNPs) with various dimensions were obtained by adjusting the hydrolysis conditions and the starting cellulose material. Three types of CNPs were fabricated, namely CNPs-L (large width), CNPs-M (medium width) and CNPs-S (small width).

The sample fabrication presented in this subsection was performed by Dr Han Yang (University of Cambridge)

In detail, CNPs-L and CNPs-M were prepared from microcrystalline cellulose (MCC, produced by SERVA Electrophoresis) hydrolysed with sulfuric acid (50 *wt*%) for 5 hours at 50°C and sulfuric acid (55 *wt*%) for 5 hours at 60°C, respectively. CNPs-S were prepared from the hydrolysis of cellulose filter paper (Whatman No. 1) with sulfuric acid (55 *wt*%) at 50°C for half an hour. All the three types of CNPs were rod-like particles, and their width and length distribution are summarised in Table 2.

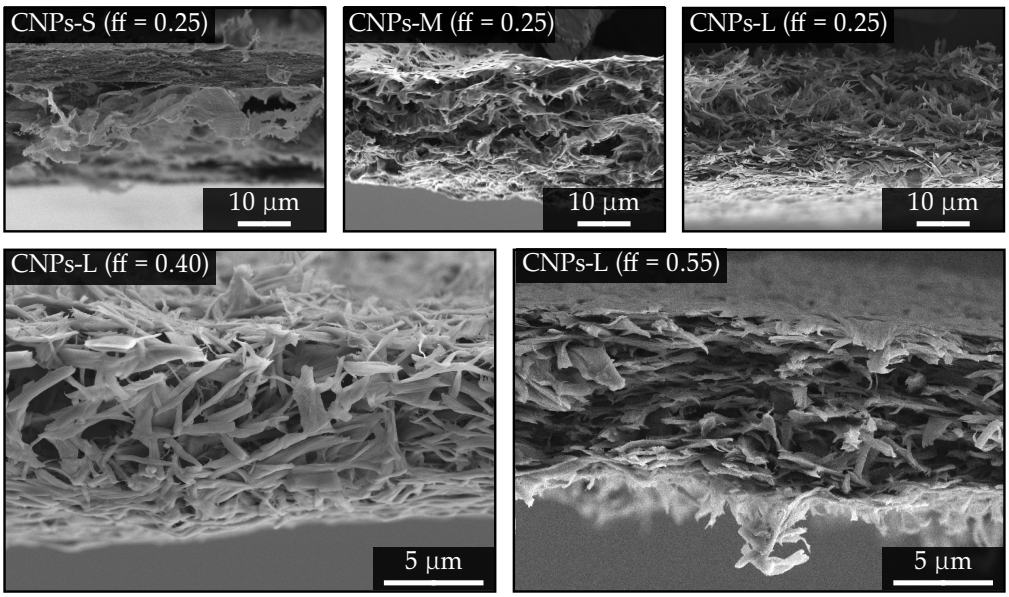

Figure 27 | Morphology of different cellulose-based materials. Typical SEM images of the cross-section of porous films obtained by the assembly of CNPs. Top row: films made using CNPs of various sizes as building blocks. Bottom row: films made of CNPs-L with same thickness but a different filling fraction.

Unlike the other two major types of cellulose nanoparticles [18], cellulose nanocrystals (CNCs) [124] and cellulose nanofibers (CNFs) [56], CNPs have a much larger width ($\simeq$ 100 nm, Table 2). Therefore, CNPs can be used to investigate scattering optimisation in a section of the parameter space not accessible by other types of cellulose particles.

	Length(µm)	Width(µm)
CNPs-S	0.23 ± 0.32	0.04 ± 0.01
CNPs-M	1.94 ± 0.68	0.21 ± 0.06
CNPs-L	2.70 ± 0.77	0.52 ± 0.02
CNCs [124]	$\simeq 0.1$	$\simeq 0.005$
CNFs [56]	$\simeq 10$	$\simeq 0.02$

Table 2 | Dimensions of different cellulose particles. CNPs have a diameter much larger than the other two major types of cellulose nanoparticles. The dimensions of the particles were estimated by transmission electron microscopy (TEM) images.

After obtaining building blocks with the desired dimensions, scattering films were prepared from the CNPs suspension by vacuum filtration followed by freeze-drying. As shown in Figure 27, CNPs form a three-dimensional, disordered network where the particles are connected by hydrogen bonding.

Notably, the fabrication process illustrated in this section is more straightforward and less toxic compared with solvent exchange methods used for the fabrication of CNFs membranes [56, 125]. Furthermore,

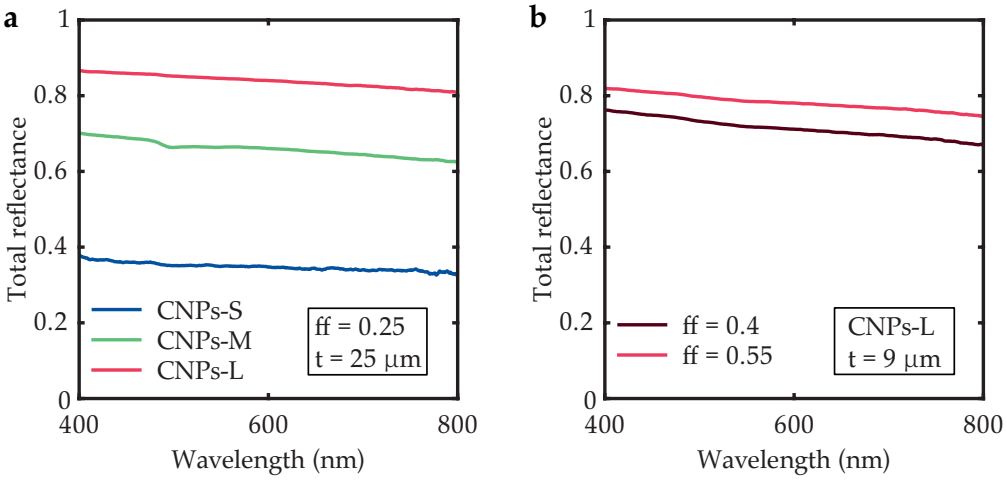

Figure 28 | Optical properties of cellulose-based scattering materials a) Dependence of the total reflectance on the size of the building blocks: CNPs-L films show a scattering efficiency significantly higher than materials made from smaller particles. All films have a comparable thickness and filling fraction, $\simeq 25\,\mu m$ and $ff \simeq 0.25$. **b)** Dependence of the total reflectance on the filling fraction: increasing the filling fraction from $\simeq 0.4$ to $\simeq 0.55$ leads to an increase in the scattering strength of CNPs-L systems. Both films have a thickness of $\simeq 9\,\mu m$.

tuning the filling fraction and thickness of a film was obtained by changing the initial amount of CNPs and the duration of the vacuum process.

6.2 OPTICAL CHARACTERISATION

The experimental approach presented in Section 6.1 was used to independently change the important scattering parameters of cellulose-based systems, and therefore maximise their scattering efficiency.

Films made of the different CNPs introduced in Table 2 were prepared to investigate the effect of the dimensions of the particles on scattering optimisation. Figure 28a shows the optical response of systems with comparable values of thickness and filling fraction ($\simeq 25\,\mu m$ and $\simeq$ 25%, respectively) but made of building blocks with different sizes. The reflectance is maximised for ensembles of CNPs-L, which show a reflectance significantly higher than that of CNPs-M and CNPs-S.

Once having identified the building block maximising scattering, the effect of the filling fraction was investigated on CNPs-L materials. Figure 28b shows the optical response of films with a comparable thickness ($9\,\mu m$) but different filling fractions, $ff \simeq 0.4$ and $ff \simeq 0.55$,

	ff	$\ell_t(\mu m)$	$t(\mu m)$	W
CNPs-S	$\simeq 0.25$	$\simeq 20$	$\simeq 25$	66
CNPs-M	$\simeq 0.25$	$\simeq 7$	$\simeq 25$	83
CNPs-L	$\simeq 0.25$	$\simeq 2.5$	$\simeq 25$	89
CNPs-L	$\simeq 0.40$	1.6 ± 0.1	$\simeq 9$	84
CNPs-L	$\simeq 0.55$	$\simeq 1$	$\simeq 9$	88
CNFs [56]	\	\	$\simeq 9$	86

Table 3 | Whiteness and transport mean free path for cellulose-based materials. CNPs-L systems have the highest scattering efficiency, showing the shortest ℓ_t, and whiteness that outperforms CNFs materials.

respectively. For CNPs-L increasing the filling fraction leads to an increase in reflectance.

The produced CNPs-based films are further compared in Table 3 in terms of their mean free path (cf. Chapter 1) and whiteness (cf. Appendix c). CNPs-L films with $ff \simeq 0.55$ exhibit a transport mean free path of $\ell_t \simeq 0.9$ — comparable to that of the PMMA films presented in Chapter 5 and to the *Cyphochilus* beetle (cf. Chapter 3). The mean free path reported in Table 3 for CNPs-L with $ff \simeq 0.40$ was obtained from measuring the total transmission on a series of samples with different thicknesses (cf. Subsection 2.1.2 and Chapter 5). For the other systems, the reported transport mean free paths represent a qualitative estimate obtained from a single film and using Equation 25. In both cases, the extrapolation length (z_e in Equation 25) was quantified using Equations 21 to 23 and the experimental filling fractions.

Moreover, Table 3 shows that CNPs-L films have a whiteness value — calculated following the procedure discussed in Chapter 4 and Appendix c — as high as 92. This result outperforms the state of the art of cellulose-based scattering materials, i.e., CNFs systems [56]. Note that Table 3 does not report a value of mean free path for the CNFs-based white membranes. Indeed, the fibrillar systems in Reference [56] are characterised by a light transport regime which is not diffusive (cf. anomalous diffusion, Section 1.3) and where a mean free path cannot be defined.

Numerical simulations were employed to provide a qualitative understanding of the scattering properties of different CNPs systems. First, the single-scattering properties of the different cellulose building

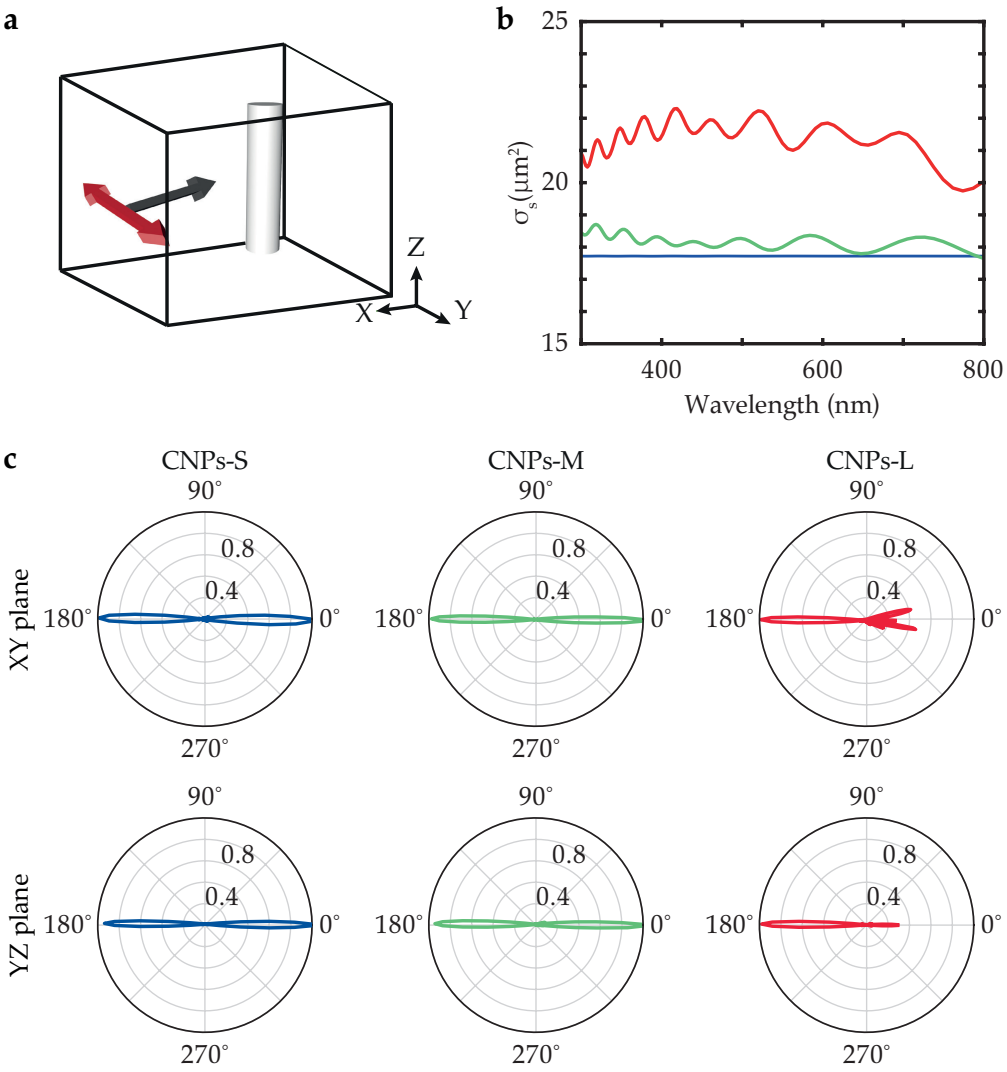

Figure 29 | Numerical, three-dimensional, simulations of the single-particle properties of CNPs. a) Schematics of the simulation setup used to calculate the scattering from CNPs, which were approximated as rods with values of diameter and length from Table 2. The incoming light and its polarisation are represented with black and red arrows, respectively. The scattered intensity was acquired in all directions. **b&c)** Scattering cross section (σ_s) and angular distribution of the scattered light (differential scattering cross section) for the three different types of CNPs, respectively. The scattering cross section was calculated as the ratio between the power of the incident source and that of the scattered radiation. The results presented in **b&c)** were obtained averaging over two orthogonal polarisations.

blocks are presented in Figure 29. Figure 29b shows that CNPs-L particles exhibit the largest scattering cross section (cf. Equation 10), i.e., the ratio between the power of the incident source and that of the scattered radiation.

However, this result does not allow to infer on the response of CNPs assemblies. Indeed, as discussed in Chapter 1, the multiple scattering response is also determined by the differential scattering cross section

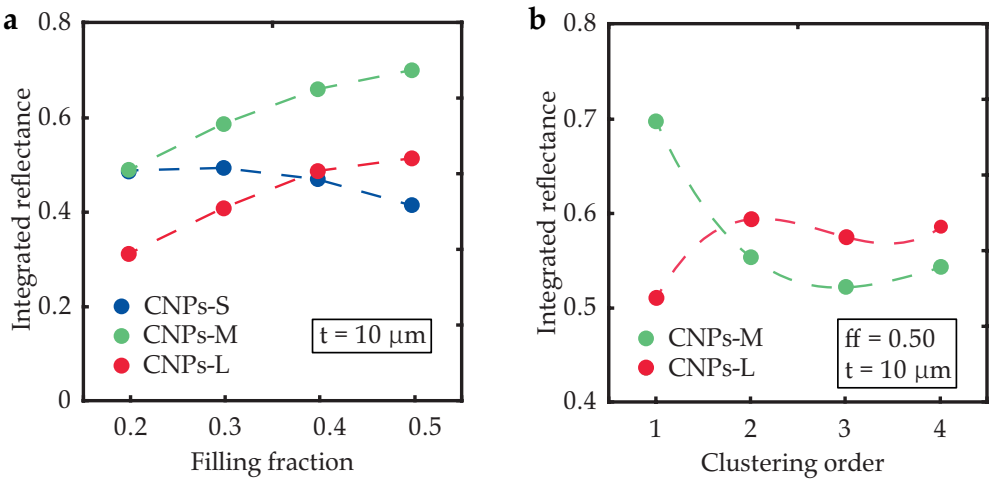

Figure 30 | Numerical, two-dimensional, simulations of the optical properties of CNPs-based systems. a) Simulated optical response for the ensemble of CNPs-L, M, S with different filling fractions. **b)** Simulated optical response for the ensemble of CNPs-M (d = 210 nm) and CNPs-L (d = 520 nm) with different clustering order. All simulated systems have a thickness of 10 µm.

(cf. Equation 8). This parameter is shown in Figure 29c for the different building blocks. CNPs-L show an angular distribution of the scattered light which is asymmetric — in contrast with CNPs-S and CNPs-M, where the scattering is symmetric (resembling Rayleigh scatterers, Figure 3).

As the validity of Equation 28 — which links the single-scattering properties with the transport mean free path — in anisotropic systems is debatable [57, 62, 63], the multiple scattering response of the films shown in Figure 28 was investigated using the algorithm presented in Subsection 2.2.2.

Figure 30a compares the simulated total reflectance averaged over the visible range for ensembles of different CNPs particles as a function of the filling fraction. The numerical results confirm what is reported in Figure 28b: for materials made of CNPs-L particles, increasing the filling fraction leads to an increase of reflectance.

Figure 30a predicts the highest scattering efficiency for CNPs-M systems, in contradiction to the experimental results in Figure 28a. This difference can be understood by taking a closer look at the morphology of the CNPs films (Figure 27). In both CNPs-S and CNPs-M films, it is possible to observe flakes made of packing of few nanoparticles. This effect is evident for CNPs-S, where the resulting films show layered structures on top of the network instead of individual connections. The origin of

these different morphologies arises during the freezing step: ice crystals formed in the wet films pushed CNPs-S (or CNPs-M) into the inter-crystalline domain boundaries, which leads to the formation of clusters [126]. In CNPs-L films, the absence of flakes and layers can be explained by the relatively large size of the nanoparticles, leading to the creation of pores which are large enough to accommodate the ice crystals — thus the ice crystals would not push CNPs-L together.

Clusters of CNPs along their short axis were used as building blocks to simulate the presence of flakes (Figure 30b). The cluster order quantifies the number of starting building blocks comprised in every flake. Note that the layered structure observed in CNPs-S films cannot be described by a finite clustering order. For CNPs-M, increasing the clustering order leads to a reduction of reflectance, justifying the experimental results presented in Figure 28a.

Moreover, this result shows that by fine-tuning the size of the CNPs and avoiding the formation of clusters in the film could further increase the optical properties reported in Figure 28.

6.3 CONCLUSIONS

This chapter presented an experimental method to manufacture a novel type of cellulose building blocks for the fabrication of bioinspired, highly-scattering films. In detail, rod-shaped, cellulose nanoparticles (CNPs) of different dimensions were obtained by adjusting both the starting cellulose material and the acid hydrolysis conditions. These nanoparticles were assembled into films whose filling fraction and thickness were controlled via filtration and freeze-drying. A mean free path of $\simeq 1\ \mu m$ was achieved by tuning the dimensions and the assembly of the CNPs. In conclusions, CNPs-based systems, due to their high scattering strength and biocompatible nature, represent a promising route for the fabrication of sustainable, white materials.

SUMMARY AND FUTURE PERSPECTIVES

This thesis demonstrated that anisotropy allows for improvements in the scattering efficiency of low refractive index media. These results introduce novel concepts in the study of disordered systems and the production of white materials. In particular, they showcase how to exploit natural resources to replace commercially available white enhancers made from inorganic high refractive materials, which have recently raised safety concerns.

SUMMARY

After introducing in Part I the concepts and tools necessary to investigate disordered media, Part II showed how nature exploits anisotropy to optimise whiteness in biological systems. In particular, after quantifying the scattering efficiency of the beetle genus *Cyphochilus*, a numerical model was developed to understand the design principles behind its outstanding optical properties. The presented model demonstrated that using anisotropic building blocks, with a certain degree of alignment, significantly increases the whiteness of low refractive index media.

In Part III, this knowledge was exploited for the manufacturing of bioinspired, white materials. First, a polymer phase separation technique was used to fabricate anisotropic scattering networks made solely of polymethyl methacrylate (PMMA). Through tuning the fabrication parameters, materials with scattering properties comparable to *Cyphochilus* were obtained. Second, as a further step towards fully sustainable and biocompatible products, similar results were obtained using cellulose as a constituent material. To achieve high scattering strength in cellulosic systems, a method to fabricate a novel kind of building blocks, i.e., cellulose nanoparticles (CNPs), was developed. In particular, this method allows for the tuning of the dimensions of the CNPs and to assemble them in films with a controlled filling fraction.

FUTURE PERSPECTIVES

The results reported in this thesis unveil new directions for both applications and fundamental studies of light propagation in disordered media.

From an applications perspective, this work can substantially impact the pigment industry by allowing the removal of inorganic particles (titania) from everyday goods. A necessary step towards the use of bioinspired products is the self-assembly of such anisotropic building blocks in spherical supraparticles. White, structurally-coloured pigments could be achieved by combining the methodologies presented in Part III with droplet-based microfluidics [127]. Exploiting a confined geometry will allow for better control of the self-assembly dynamics compared to the planar case; therefore enabling the attainment of particles whose building blocks have different degrees of orientational order. According to the theoretical predictions in Chapter 4, controlling the orientational order will increase the scattering performances reported in Part III. Moreover, the whiteness of structurally-coloured pigments could be further improved by fine-tuning their filling fraction and the dimensions of the building blocks. The generalisation of the algorithm presented in Chapter 4 to three dimensions will allow the quantitative prediction — and therefore the engineering — of the optical response of bioinspired materials. Finally, chemical methods could be exploited to functionalise the biopolymer building blocks in order to form hydrophobic pigments. This step would enable the use of structurally-coloured particles in water formulations, as commonly required for cosmetics and paints.

From a fundamental perspective, the study of anisotropic media brings new challenges and opportunities to the field of disordered photonics. Anisotropic systems possess an extra degree of freedom compared to their isotropic counterparts: the degree of alignment. Tuning the alignment of anisotropic, disordered systems could allow the control of light propagation and explore the transition between different scattering regimes. Moreover, the behaviour of polarisation in three-dimensional, disordered systems in the presence of anisotropy could deviate from the isotropic case, where light is rapidly depolarised in the multiple scattering regime [4]. Finally, combining anisotropy and multiple scattering could be of further interest in the study of light

transport phenomena beyond diffusion, such as anomalous diffusion [52–55] or Anderson localisation [76–78].

Part IV

APPENDICES

a

MONTE CARLO CODE FOR ANISOTROPIC MULTIPLE LIGHT SCATTERING

This *Mathematica* code has been used to generate the numerical results in Section 3.2. Any changes to the code will be uploaded to the following repository.

Definition of the simulation parameters:

```
ClearAll["Global`*"];
nWalkers = 1; (*N\[Degree] of photons used*)
lowerCut = 1;
thickness = 7;(*Sample thickness*)
γ = 1.4; (*XY components of the TMFP*)

a = 0.725; (*Anisotropy parameter*)
γz = γ*a; (*Z component of the TMFP*)

scatteringorder = (thickness/γz)^2;(*Parameter that you can tune to understand the influence
      of the scattering order on the interference*)

indexWalker = 0;
indexReflected = 0;
indexTransmitted = 0;
indexOut = 0;
indexSingle = 0;
indexBouncedR = 0;
indexBouncedT = 0;
listα = Table[0, {nWalkers}];
listα2 = Table[0, {nWalkers}];
listr = Table[0, {nWalkers}];
listz = Table[0, {nWalkers}];
values = Join[Range[-10, -10, 1], Range[1, 1, 1]];
```

Calculation of R for internal reflections:

```
nc = 1.55; (*Chitin refractive index*)
α = (nc^2 - 1)/(nc^2 + 2);
n[f_] = √((1 + 2 f*α)/(1 - f*α)); (*Effective refractive index, from Maxwell-Garnett's
     theory*)

n1 = n[0.45];  (*Chitin filling fraction in the white beetle, from Wilts et al.*)
n2 = 1;
```

```
Rs[θ_] = Abs[(n1*Cos[θ] - n2*√(1 - (n1/n2*Sin[θ])^2))/(n1*Cos[θ] +n2*√(1 -
(n1/n2*Sin[θ])^2))]^2; (*Fresnel's coefficients*)

Rp[θ_] = Abs[(-n2*Cos[θ] + n1*√(1 - (n1/n2*Sin[θ])^2))/(n2*Cos[θ] + n1*√(1 -
(n1/n2*Sin[θ])^2))]^2;
R[θ_] = (Rs[θ] + Rp[θ])/2;
Ru[θ_] = (Rs[θ] + Rp[θ])/2;
c1 = NIntegrate[Ru[θ]* Sin[θ]*Cos[θ] , {θ, 0, \[Pi]/2}, MaxRecursion -> 100];
c2 = NIntegrate[Ru[θ]* Sin[θ]*(Cos[θ])^2, {θ, 0, \[Pi]/2}, MaxRecursion -> 100];
Ravg = (3 c2 + 2 c1)/(3 c2 - 2 c1 + 2);
```

Functions used in the main loop to discriminate the photons:

```
doS1[] := ((*Singly-scattered photons. They do not contribute to the CBS effect*)
            indexSingle++;
            Break[];
        );

doS2[] := ( (*Photons scattered more than the scattering order decided*)

            indexWalker++;
            indexOut++;
            Break[];
        );

doRef[] := ( (*Photons that contributes to the CBS: we want to calculate the distance
     between the first and the last scattering positions*)
            lastPoint = oldPoint;
            outPoint = currentPoint;
            \\delta = firstPoint - lastPoint;


            If[
                    firstPoint == lastPoint, Break[],
                    listα[[indexWalker]] = ArcSin[\\delta[[3]]/√[\\delta[[1]]^2 + \\delta
                         [[2]]^2 + \\delta[[3]]^2]];
                    listr[[indexWalker]] = √((firstPoint[[1]] -lastPoint[[1]])^2 + (
                         firstPoint[[2]] - lastPoint[[2]])^2 +(firstPoint[[3]] - lastPoint
                         [[3]])^2);
                    listz[[indexWalker]] = outPoint[[3]];
                    indexWalker++;
                    indexReflected ++;
                    Break[];
                ]
        );

doTra[] := ((*Photons transmitted*)
            lastPoint = oldPoint;
            indexWalker++;
            indexTransmitted ++;
            Break[];
        );

doSpecR[] := ((*Photons reflected at the entrance surface of the
```

```
material (z=0) back in the material*)
                indexBouncedR++;
                lastPoint = oldPoint;
                outPoint = currentPoint;
                \\delta2 = lastPoint - outPoint;
                intercept = RegionCentroid[RegionIntersection[InfiniteLine
                [{lastPoint, outPoint}], InfinitePlane[{{0, 0, 0}, {0, 1, 0},
                {1, 0, 0}}]]];
                rt = ReflectionTransform[{\\delta2[[1]], \\delta2[[2]], 0},intercept];
                specular = rt[lastPoint];
                specular2 = -(γz)*Log[RandomReal[]];
                specularPoint = RegionCentroid[RegionIntersection[InfiniteLine[{intercept,
                     specular}], InfinitePlane[{{0, 0, specular2},{0, 1, specular2}, {1, 0,
                     specular2}}]]];
                currentPoint = specularPoint;

    );

doSpecT[] := ((*Photons reflected at the exit surface of the material (z=thickness) back in
     the material*)
            indexBouncedT++;
            lastPoint = oldPoint;
            outPoint = currentPoint;
            \\delta2 = lastPoint - outPoint;
            intercept =
                RegionCentroid[ RegionIntersection[InfiniteLine[{lastPoint, outPoint}],
                     InfinitePlane[{{0, 0, thickness}, {0, 1, thickness}, {1, 0,thickness
                     }}]]];
            rt = ReflectionTransform[{\delta2[[1]], \delta2[[2]], 0}, intercept];
            specular = rt[lastPoint];
            specular2 = thickness + (γz)*Log[RandomReal[]];
            specularPoint = RegionCentroid[RegionIntersection[InfiniteLine[{intercept,
                 specular}], InfinitePlane[{{0, 0, specular2}, {0, 1, specular2}, {1, 0,
         specular2}}]]];
            currentPoint = specularPoint;
   );
```

Main loop where the random walk is performed:

```
Timing[
    While[
        indexWalker <= nWalkers,
        firstPoint = {0, 0, -(γz)*Log[RandomReal[]]};
        (*Depth of 1st scatter: probability sampled using an inverse sampling techinique*)
        oldPoint = firstPoint;
        currentPoint = {0, 0, 0};
        currentOrder = 1;
        lastPoint = {0, 0, 0};
        Ravg = 0;

    While[True, (*While loop, the conditions to stop it are in the following Ifs*)
        ϕ = Random[Real, {0, \[Pi]}];
        ψ = Random[Real, {0, 2 \[Pi]}];
        δxy = -γ*Log[RandomReal[]];
        δz = a*δxy;
```

```
        randomStep = {δxy*√(1 - Cos[ϕ]^2)*Cos[ψ], δxy*√(1 - Cos[ϕ]^2)*Sin[ψ],δz*Cos[ϕ
             ]};
        currentPoint = {oldPoint[[1]] + randomStep[[1]], oldPoint[[2]] + randomStep[[2]] ,
             oldPoint[[3]] + randomStep[[3]]};

        r = RandomReal[];
        Which[
                currentPoint[[3]] < 0 && currentOrder <= lowerCut , doS1[],
                currentPoint[[3]] < 0 && currentOrder > scatteringOrder, doS2[],
                currentPoint[[3]] < 0 && currentOrder > lowerCut && currentOrder <=
                     scatteringOrder && r > Ravg, doRef[],
                currentPoint[[3]] < 0 && currentOrder > lowerCut && currentOrder <=
                     scatteringOrder && r <= Ravg, doSpecR[],
                currentPoint[[3]] > thickness && r <= Ravg, doSpecT[],
                currentPoint[[3]] > thickness, doTra[]
                ];
        currentOrder++;
        oldPoint = currentPoint;
        ]
    ]
 ]
```

Calculation of the coherent backscattering (CBS) line shape:

```
λ = 0.635;
(*Clearing the zeros that correspond to transmitted photons*)
a = DeleteCases[listr, 0];
b = DeleteCases[listα, 0];
c = DeleteCases[-listz, 0];
(*Coherent term*)
γc[θ_] := Sum[(Exp[(-c[[i]])/γz]*\((1 - Ravg))*Cos[2π/λ]a[[[i]]]*((Sin[b[[[i]]]]
      - Sin[b[[[i]]] + θ]))), {i, 1, indexReflected}];
(*To normalise the CBS it is necessary to perform a simulation for semi-infinite media (we
     used OT=1000). Simulations with different R requires different normalisatinos *)

CBS[θ_] := γc[θ];
```

Exporting the data for further analysis:

```
θmin = 0.0;
θmax = 0.4;
θstep = 0.2/57;

θstepnumber = Ceiling[(θmax - θmin)/θstep];
simulationData = Table[0, {θstepnumber}, {2}];
For[i = 1, i <= θstepnumber, i++,
    simulationData[[i, 1]] = N[θmin + (i - 1)*θstep];
    simulationData[[i, 2]] = CBS[θmin + (i - 1)*θstep];
    ]
```

b

CODE FOR GENERATING 2D DISORDERED STRUCTURES

This *Python* code has been used to generate the ensembles of anistropic particles presented in Chapter 4. Any change to the code will be uploaded to the following repository. The inverse-design code to generate structures with a tailored structure factor is available upon request.

Definition of the simulation parameters:

```
from matplotlib import pyplot as plt
from matplotlib import interactive
from matplotlib.pyplot import figure, show
from shapely.geometry import Polygon
from shapely.geometry.base import BaseGeometry
from shapely.geometry.point import Point
from shapely import affinity
from matplotlib.patches import Polygon
import numpy as np
import pylab as pl
import time
from termcolor import colored, cprint
from scipy.stats import norm
from datetime import datetime
import os

def main():
    bbox=(-2.5,2.5) #sample size ($\mu$m)
    step=7 #number of, statistical identical, random structures to generate
    alphaMean=0 #particles' orientation
    alphaSigma=0 #deviation from the average orientation

    if index<(indexMin+step):
        c=7 #aspect ratio
        r=0.1 #radius of the corresponding (same area) isotropic particle (in $\mu$m)
        rsigma=r*30/100 #polydispersity
        ff=0.60 #filling fraction
```

Main loop where the particles are sequentially added:

```
ellipses=[]
```

```
currentFF=0
particlesToAdd=[]

while currentFF<ff:
    rdd=normDist(r,rsigma)
    particlesToAdd.append(rdd)
    currentFF=currentFF+(rdd*rdd*c*3.1427)/(((bbox[1]-bbox[0])**2))


particlesToAdd=np.array(particlesToAdd)
particlesToAdd=np.flip(np.sort(particlesToAdd),0) #reodered to start adding from the largest
      particles
aOccupied=0

k=0
iteration=0
resampled=0 #checks for eventual size-rejection
aOccupied=0
while k<len(particlesToAdd):
    while(iteration < 20000):
        iteration += 1
        rd=particlesToAdd[k]
        alpha = normDist(alphaMean, alphaSigma)
        center = boxForcing(bbox[0], bbox[1], rd, c, alpha)
        x = center[0][0]
        y = center[0][1]
        ellips = create_ellipse((x, y), rd, (1, c), alpha)
        overlap = pl.array([ellips.intersects(ellipses[i][4]) for i in range(len(ellipses))
             ])

        if all(overlap[i] == False for i in range(len(ellipses))):
            one_row = []
            one_row.extend([x, y, rd, alpha, ellips])
            ellipses.append(one_row)
            aOccupied +=rd*rd*c*3.1427
            cprint(aOccupied/((bbox[1]-bbox[0])**2), 'green')
            k+=1
            iteration=0
            break

        if iteration == 20000:
            cprint('rejected', 'yellow')
            resampled+=1
            break
    else:
        iteration=0
        rd = normDistRejected(r,rd, rsigma) #samples a smaller particle


radDist=[]
for i in range(len(ellipses)):
    radDist.append(ellipses[i][2]*2*c)

(mu, sigma) = norm.fit(radDist)

if 0: #visualize the size distribution
    cprint("Plotting legth distribution","cyan")
```

```
    (mu, sigma) = norm.fit(radDist)
    xmin, xmax = (mu-5*sigma,mu+5*sigma)
    x = pl.linspace(xmin, xmax, 1000)
    pl.hist(radDist,bins=15,normed=True)
    p = norm.pdf(x, mu, sigma)
    pl.plot(x, p, 'k', linewidth=2)
    pl.xlabel('Length ($\mu$m)')
    pl.ylabel('Probability')
    pl.title(r'$\mathrm{Radii\ distribution\:}\ \mu=%.3f,\ \sigma=%.3f$' %(mu, sigma))
    pl.savefig("RadiusDist"+str(index)+".pdf")
    pl.close('all')
    pl.xlim([0,0.4])



if 1: #visualise the final structure
    vertices=pl.array([ellipses[i][4].exterior.coords.xy for i in range(len(ellipses))])
    patches=pl.array([Polygon(vertices[i].T,color = 'black', alpha = 1) for i in range(len(
        ellipses))])
    fig,ax = plt.subplots()
    ax.set_xlim([bbox[0],bbox[1]])

    ax.set_ylim([bbox[0],bbox[1]])
    ax.set_aspect('equal')

    for i in range(len(patches)):
        ax.add_patch(patches[i])

    pl.title("Distribution:("+str(mu)[0:5]+", "+str(sigma)[0:5]+"); Filling Fraction:"+str(
        ff))
    pl.savefig("Ensemble"+str(index)+".pdf")
    pl.close('all')
```

Auxiliary functions:

```
def normDist(r,rsigma): #defines an always positive normal distribution (for very broad size
     distributions)
    x=pl.normal(r,rsigma)
    while x<0:
        x=pl.normal(r,rsigma)
    return x

def normDistRejected(r,rd,rsigma): #looks for smaller particles in case of rejection
    x=pl.normal(r,rsigma)
    while x>rd:
        x=pl.normal(r,rsigma)
    return x

def create_ellipse(center,radius,lengths,angle=0): #creates an ellipse using Shapely
    """
    create a shapely ellipse. adapted from
    https://gis.stackexchange.com/a/243462
    """
```

```
    circ = Point(center).buffer(radius)
    ell = affinity.scale(circ, int(lengths[0]), int(lengths[1]))
    ellr = affinity.rotate(ell, angle)
    return ellr

def boxForcing(bMin,bMax,radius,c,angle): #confines the particles inside the sample

    x=pl.uniform(bMin,bMax)
    y=pl.uniform(bMin,bMax)

    if x<(bMin+c*radius):
        x=x+(radius)*(1+c*pl.absolute(pl.sin(pl.radians(angle))))
        if x>(bMax-c*radius):
            x=bMin+c*radius
    if x>(bMax-c*radius):
        x=x-(radius)*(1+c*pl.absolute(pl.sin (pl.radians(angle))))

        if x<(bMin+c*radius) :
            x=bMax-c*radius

    if y>(bMax-c*radius):
        y=y-(radius)*(1+c*pl.absolute(pl.cos(pl.radians(angle))))
        if y<(bMin+c*radius) :
            y=bMax-c*radius

    if y<(bMin+c*radius):
        y=y+(radius)*(1+c*pl.absolute(pl.cos(pl.radians(angle))))
        if y>(bMax-c*radius):
            y=bMin+c*radius

    center=[]
    center.append([x,y])

    return center

indexMin=1
indext=1
indexMax=2
for i in range(indext,indexMax):
        index=i
        main()
```

C

COLOUR SPACE MAPPING AND WHITENESS

In Chapter 4 a numerical method to optimise scattering in granular media was presented. The degree of optimisation of each different system was classified in terms of their whiteness. This parameter allows to directly relate the spectral response of a medium with how it is perceived by the human eye - therefore resulting crucial for applications.

The whiteness of each system was quantified by mapping the simulated spectra in the CIELAB colourspace. CIELAB is a three-dimensional real number space, where the L coordinate quantifies the brightness of a material, while a^* and b^* are the green-red and blue-yellow coordinates describing the saturation of a colour. Therefore L depends on the scattering strength of a system while a^* and b^* on its spectral dispersion. Importantly, the choice of using the CIELAB colourspace was motivated by its euclidian nature. This property allows an intuitive definition of whiteness (W) as [100, 128]:

$$W = 100 - |\mathbf{X_w} - \mathbf{X_m}| \tag{48}$$

where $|...|$ denotes the three-dimensional euclidian distance, $\mathbf{X_w} = \{100, 0, 0\}$ and $\mathbf{X_m}$ are the CIELAB coordinates of a perfect broadband diffuser (also known as white point) and of the material of interest, respectively.

More in detail, the CIELAB coordinates of a given simulation were calculated in two steps: First, from the simulated spectra, the so-called tristimulus values (XYZ) were estimated using CIE Coordinate Calculator, a Matlab plugin [129]. To calculate XYZ the reflectance curves were multiplied by a CIE standard illuminant and then convoluted with the average human response to wavelengths of light (standard observer). The result of this first conversion step is shown in Figure 31b, where the color coordinates of the spectra in Figure 31a are represented in the xy chromaticity diagram. The xyY space is a widely

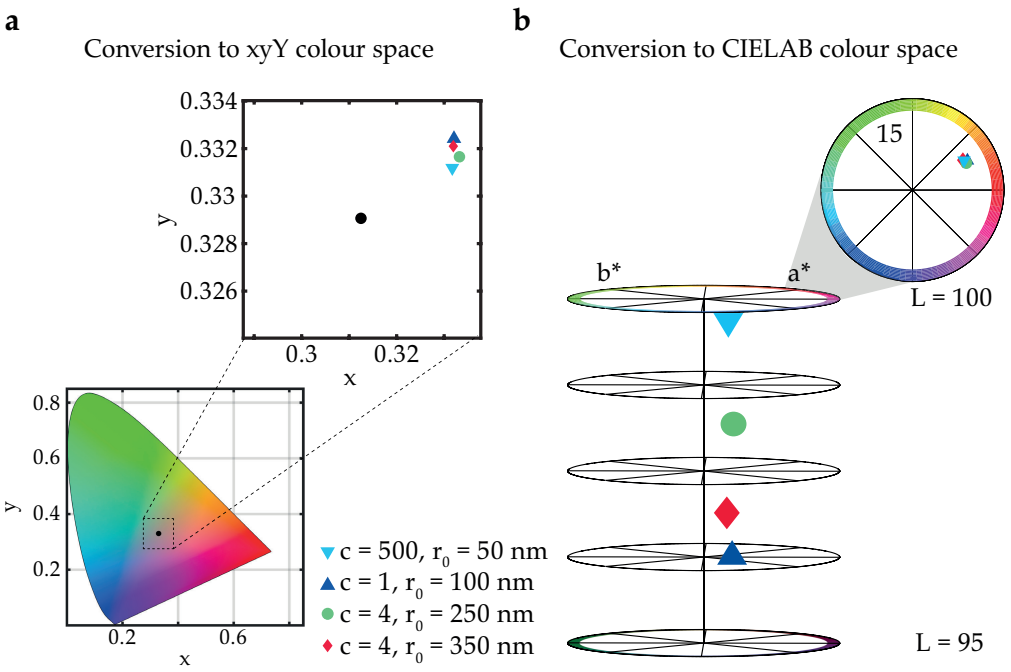

Figure 31 | Procedure to quantify the whiteness of a system. a) xy chromaticity diagram of the spectra in panel Figure 21. **b)** Three-dimensional plot showing the CIELAB coordinates of the spectra in Figure 21.

Note that all conversions reported in this thesis were performed assuming a standard observer (CIE 1931 2°) and a standard illuminant (Daylight D65).

used derivative of XYZ, whose coordinates can be calculated by using the `xyl2xyz`, a built-in Matlab function. Second, the XYZ values were converted in CIELAB coordinates using `xyz2lab`, also a built-in Matlab function. The whiteness values for the spectra in Figure 31a are reported in Appendix c.

n	r_0(nm)	c	ff	W
2.60	50	500	0.4	91
2.60	100	1	0.3	90
2.60	150	6	0.4	89
2.60	250	4	0.5	89
2.60	350	4	0.5	88
2.60	500	4	0.5	88
1.55	150	18	0.3	90

Table 4 | Whiteness comparison for high refractive index media. Parameters which maximise whiteness (W) for ensembles of particles with different sizes (r_0, i.e. the radius at c = 1), refractive index (n), but same thickness (t = 10 µm).

The importance of classifying scattering materials in terms of their whiteness is emphasised by the results in Chapter 4. In particular, it was shown that anisotropic, low refractive index media can obtain a whiteness comparable to their isotropic, high refractive index counterpart thanks to their lower spectral saturation. Notably, a comparison of these two classes of systems only in terms of their scattering efficiency would have

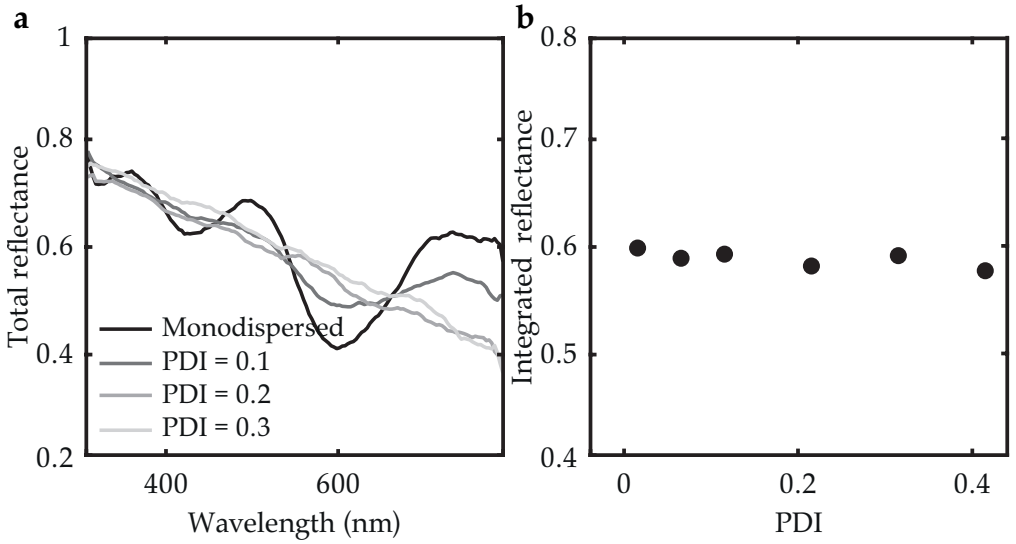

Figure 32 | Simulated optical response for structures with different degrees of polydispersity: a) spectral dependence, **b)** integrated reflectance. All the structures have a thickness of $10\,\mu m$, $ff = 0.3$, and isotropic building blocks with $n = 1.55$ and $r = 250\,nm$.

PDI	n	$r_0(nm)$	c	ff	W
0	1.55	250	1	0.3	81
0.1	1.55	250	1	0.3	81
0.2	1.55	250	1	0.3	82
0.3	1.55	250	1	0.3	82

Table 5 | Effect of polydispersity on the whiteness. Values of whiteness (W) for ensembles of particles with different polydispersity index (PDI).

erroneously concluded that high refractive index media outperform ensembles of anisotropic, low refractive index particles.

The following sections collect the data supporting the optimisation procedure presented in Chapter 4.

C.1 THE EFFECT OF POLYDISPERSITY

The simulations presented in the main text account for a polydispersity in the size of the particles. Increasing the polydispersity cancels out the resonant behaviour of the scattering (Figure 32), but it does not affect the whiteness (Table 5). The polydispersity index (PDI) in Table 5 is defined as the ratio between the standard deviation and the mean value of the size distribution of the particles.

C.2 DETAILS OF THE OPTIMISATION PROCEDURE

The values of aspect ratio (c) and filling fraction (ff) maximising scattering were obtained following the procedure discussed in Section 4.1. Table 6 and Table 7 provides the values of whiteness (W) as a function of the aspect ratio for particles with $n = 1.55$ and $n = 2.60$, respectively.

n	$r_0(nm)$	c	$t(\mu m)$	ff	W
1.55	100	1	10	0.2	69
1.55	100	2	10	0.2	80
1.55	100	4	10	0.2	86
1.55	100	6	10	0.2	87
1.55	100	8	10	0.2	88
1.55	100	10	10	0.2	87
1.55	150	1	10	0.1	70
1.55	150	2	10	0.1	68
1.55	150	4	10	0.1	70
1.55	150	6	10	0.1	76
1.55	150	8	10	0.1	80
1.55	150	10	10	0.1	83
1.55	150	16	10	0.1	84
1.55	150	18	10	0.1	85
1.55	150	20	10	0.1	84
1.55	150	50	10	0.1	79
1.55	150	100	10	0.1	78
1.55	250	1	20	0.05	68
1.55	250	2	20	0.05	64
1.55	250	4	20	0.05	59
1.55	250	6	20	0.05	58
1.55	250	8	20	0.05	60
1.55	250	10	20	0.05	66
1.55	350	1	20	0.08	72
1.55	350	2	20	0.08	73
1.55	350	4	20	0.08	63
1.55	350	6	20	0.08	66
1.55	350	8	20	0.08	68
1.55	350	10	20	0.08	67

Table 6 | Whiteness optimisation for low refractive index systems. For every r_0 systems with same thickness (t) and filling fraction (ff) were compared.

n	r_0(nm)	c	t(µm)	ff	W
2.6	50	1	10	0.2	85
2.6	50	2	10	0.2	87
2.6	50	4	10	0.2	87
2.6	50	6	10	0.2	88
2.6	50	8	10	0.2	88
2.6	50	10	10	0.2	89
2.6	50	20	10	0.2	89
2.6	50	60	10	0.2	90
2.6	50	200	10	0.2	91
2.6	50	500	10	0.2	91
2.6	100	1	10	0.2	89
2.6	100	2	10	0.2	88
2.6	100	4	10	0.2	87
2.6	100	6	10	0.2	87
2.6	100	8	10	0.2	87
2.6	100	10	10	0.2	88
2.6	150	1	10	0.2	86
2.6	150	2	10	0.2	87
2.6	150	4	10	0.2	87
2.6	150	6	10	0.2	88
2.6	150	8	10	0.2	87
2.6	150	10	10	0.2	86
2.6	250	1	10	0.2	87
2.6	250	2	10	0.2	88
2.6	250	4	10	0.2	89
2.6	250	6	10	0.2	88
2.6	250	8	10	0.2	88
2.6	250	10	10	0.2	87
2.6	350	1	10	0.2	83
2.6	350	2	10	0.2	86
2.6	350	4	10	0.2	88
2.6	350	6	10	0.2	87
2.6	350	8	10	0.2	87
2.6	350	10	10	0.2	86
2.6	500	1	10	0.2	81
2.6	500	2	10	0.2	84
2.6	500	4	10	0.2	86
2.6	500	6	10	0.2	87
2.6	500	8	10	0.2	86
2.6	500	10	10	0.2	86

Table 7 | Whiteness optimisation for high refractive index systems. For every r_0 we compared systems with same thickness (t) and filling fraction (ff).

BIBLIOGRAPHY

1. Van de Hulst, H. C. *Light scattering by small particles* (John Wiley and Sons, 1957).
2. Sheng, P. *Introduction to Wave Scattering, Localization and Mesoscopic Phenomena* (Springer, 2009).
3. Ishimaru, A. *Wave Propagation and Scattering in Random Media, Vols. I and II* (Academic Press, 1989).
4. Akkermans, E. & Montambaux, G. *Mesoscopic physics of electrons and photons* (Cambridge University Press, 2007).
5. Bohren, C. F. & Huffman, D. R. *Absorption and scattering of light by small particles* (Wiley-VCH, 2008).
6. Wiersma, D. S. Disordered photonics. *Nature Photonics* **7** (2013).
7. Fraden, S. & Maret, G. Multiple light scattering from concentrated, interacting suspensions. *Physical Review Letters* **65** (1990).
8. Rojas-Ochoa, L. F., Mendez-Alcaraz, J. M., Sáenz, J. J., Schurtenberger, P. & Scheffold, F. Photonic Properties of Strongly Correlated Colloidal Liquids. *Physical Review Letters* **93** (2004).
9. Utel, F., Cortese, L., Wiersma, D. S. & Pattelli, L. Optimized White Reflectance in Photonic-Network Structures. *Advanced Optical Materials* **7** (2019).
10. Yoo, K. M., Liu, F. & Alfano, R. R. When does the diffusion approximation fail to describe photon transport in random media? *Phys. Rev. Lett.* **64** (1990).
11. Elaloufi, R., Carminati, R. & Greffet, J.-J. Diffusive-to-ballistic transition in dynamic light transmission through thin scattering slabs: a radiative transfer approach. *J. Opt. Soc. Am. A* **21** (2004).
12. Mazzamuto, G., Pattelli, L., Toninelli, C. & Wiersma, D. S. Deducing effective light transport parameters in optically thin systems. *New Journal of Physics* **18** (2016).
13. DeVore, J. R. Refractive Indices of Rutile and Sphalerite. *J. Opt. Soc. Am.* **41** (1951).

14. H, B. J. Titanium Dioxide - A Review. *JCT, Journal of coatings technology,* **69** (1997).

15. Weir, A., Westerhoff, P., Fabricius, L., Hristovski, K. & von Goetz, N. Titanium Dioxide Nanoparticles in Food and Personal Care Products. *Environmental Science & Technology* **46** (2012).

16. Bettini, S. *et al.* Food-grade TiO2 impairs intestinal and systemic immune homeostasis, initiates preneoplastic lesions and promotes aberrant crypt development in the rat colon. *Scientific Reports* **7** (2017).

17. Leertouwer, H. L., Wilts, B. D. & Stavenga, D. G. Refractive index and dispersion of butterfly chitin and bird keratin measured by polarizing interference microscopy. *Opt. Express* **19** (2011).

18. Frka-Petesic, B. & Vignolini, S. So much more than paper. *Nature Photonics* **13** (2019).

19. Vukusic, P., Hallam, B. & Noyes, J. Brilliant Whiteness in Ultrathin Beetle Scales. *Science* **315** (2007).

20. Burresi, M., Cortese, L., Pattelli, L., Kolle, M., Vukusic, P., Wiersma, D. S., Steiner, U. & Vignolini, S. Bright-White Beetle Scales Optimise Multiple Scattering of Light. *Scientific Reports* **4** (2014).

21. Cortese, L., Pattelli, L., Utel, F., Vignolini, S., Burresi, M. & Wiersma, D. S. Anisotropic Light Transport in White Beetle Scales. *Advanced Optical Materials* **3** (2015).

22. Wilts, B. D. *et al.* Evolutionary-Optimized Photonic Network Structure in White Beetle Wing Scales. *Advanced materials* **30** (2018).

23. Wheeler, J. A. On the Mathematical Description of Light Nuclei by the Method of Resonating Group Structure. *Phys. Rev.* **52** (1937).

24. Heisenberg, W. Die „beobachtbaren Größen“in der Theorie der Elementarteilchen. *Zeitschrift für Physik* **120** (1943).

25. Cushing, J. T. *Theory Construction and Selection in Modern Physics: The S Matrix* (Cambridge University Press, 1990).

26. Carminati, R., Sáenz, J. J., Greffet, J.-J. & Nieto-Vesperinas, M. Reciprocity, unitarity, and time-reversal symmetry of the S matrix of fields containing evanescent components. *Phys. Rev. A* **62** (2000).

27. Stokes, G. G. On the composition and resolution of streams of polarized light from different sources. *Transactions of the Cambridge Philosophical Society* **399** (1852).

28. Mueller, H. The foundation of optics. *Journal of the Optical Society of America* **661** (1948).

29. Rayleigh, L. X. On the electromagnetic theory of light. *The London, Edinburgh, and Dublin Philosophical Magazine and Journal of Science* **12** (1881).

30. Mie, G. Beiträge zur Optik trüber Medien, speziell kolloidaler Metallösungen. *Annalen der Physik* **330** (1908).

31. Wriedt, T. A review of elastic light scattering theories. *Particle & particle systems characterization* **15** (1998).

32. Joannopoulos, J. D., Johnson, S. G., Winn, J. N. & Meade, R. D. *Photonic Crystals: Molding the Flow of Light* (Princeton University Press, 2011).

33. Kubo, R., Toda, M. & Hashitsume, N. *Statistical physics II: nonequilibrium statistical mechanics* (2012).

34. Lindeberg, J. W. Eine neue Herleitung des Exponentialgesetzes in der Wahrscheinlichkeitsrechnung. *Mathematische Zeitschrift* **1** (1922).

35. Bertolotti, J. *Light transport beyond diffusion* (PhD thesis, Università degli studi di Firenze, 2007).

36. Zhu, J. X., Pine, D. J. & Weitz, D. A. Internal reflection of diffusive light in random media. *Physical Review A* **44** (1991).

37. Garcia, N., Genack, A. & Lisyansky, A. Measurement of the transport mean free path of diffusing photons. *Physical review. B, Condensed matter* **46** (1992).

38. Born, M. & Wolf, E. *Principles of optics: electromagnetic theory of propagation, interference and diffraction of light* (Cambridge University Press, 2013).

39. Soukoulis, C. M., Datta, S. & Economou, E. N. Propagation of classical waves in random media. *Physical Review B* (1994).

40. Vera, M. U. & Durian, D. J. Angular distribution of diffusely transmitted light. *Phys. Rev. E* **53** (1996).

41. Vera, M. U., Lemieux, P. A. & Durian, D. J. Angular distribution of diffusely backscattered light. *JOSA A* (1997).

42. Gómez-Medina, R., Froufe-Pérez, L. S., Yépez, M., Scheffold, F., Nieto-Vesperinas, M. & Sáenz, J. J. Negative scattering asymmetry parameter for dipolar particles: Unusual reduction of the transport mean free path and radiation pressure. *Phys. Rev. A* **85** (2012).

43. Rojas-Ochoa, L. F., Mendez-Alcaraz, J. M., Sáenz, J. J., Schurtenberger, P. & Scheffold, F. Photonic Properties of Strongly Correlated Colloidal Liquids. *Phys. Rev. Lett.* **93** (2004).

44. Ornstein, L. S. & Zernike, F. Accidental deviations of density and opalescence at the critical point of a single substance. *Royal Netherlands Academy of Arts and Sciences (KNAW) Proceedings* **17** (1914).

45. Percus, J. K. & Yevick, G. J. Analysis of Classical Statistical Mechanics by Means of Collective Coordinates. *Phys. Rev.* **110** (1958).

46. Baus, M. & Colot, J. L. Thermodynamics and structure of a fluid of hard rods, disks, spheres, or hyperspheres from rescaled virial expansions. *Phys. Rev. A* **36** (1987).

47. Aubry, G. J., Schertel, L., Chen, M., Weyer, H., Aegerter, C. M., Polarz, S., Cölfen, H. & Maret, G. Resonant transport and near-field effects in photonic glasses. *Phys. Rev. A* **96** (2017).

48. Schertel, L., Wimmer, I., Besirske, P., Aegerter, C. M., Maret, G., Polarz, S. & Aubry, G. J. Tunable high-index photonic glasses. *Phys. Rev. Materials* **3** (2019).

49. Schertel, L., Siedentop, L., Meijer, J.-M., Keim, P., Aegerter, C. M., Aubry, G. J. & Maret, G. The Structural Colors of Photonic Glasses. *Advanced Optical Materials* **7** (2019).

50. García, P. D., Sapienza, R., Blanco, Á. & López, C. Photonic Glass: A Novel Random Material for Light. *Advanced Materials* **19** (2007).

51. Sapienza, R. *Photonic nano materials: anisotropic transport and optical Bloch oscillations* (PhD thesis, Università degli studi di Firenze, 2005).

52. Metzler, R. & Klafter, J. The random walk's guide to anomalous diffusion: a fractional dynamics approach. *Physics Reports* **339** (2000).

53. Klafter, J. & Sokolov, I. M. Anomalous diffusion spreads its wings. *Physics World* **18** (2005).

54. Barthelemy, P., Bertolotti, J. & Wiersma, D. S. A Lévy flight for light. *Nature* **453** (2008).

55. Bertolotti, J., Vynck, K., Pattelli, L., Barthelemy, P., Lepri, S. & Wiersma, D. S. Engineering Disorder in Superdiffusive Lévy Glasses. *Advanced Functional Materials* **20** (2010).

56. Toivonen, M. S., Onelli, O. D., Jacucci, G., Lovikka, V., Rojas, O. J., Ikkala, O. & Vignolini, S. Anomalous-Diffusion-Assisted Brightness in White Cellulose Nanofibril Membranes. *Advanced materials* **30** (2018).

57. Kienle, A. Anisotropic Light Diffusion: An Oxymoron? *Physical Review Letters* **98** (2007).

58. Stark, H. & Lubensky, T. C. Multiple Light Scattering in Nematic Liquid Crystals. *Phys. Rev. Lett.* **77** (1996).

59. Van Tiggelen, B. A., Maynard, R. & Heiderich, A. Anisotropic Light Diffusion in Oriented Nematic Liquid Crystals. *Phys. Rev. Lett.* **77** (1996).

60. Heino, J., Arridge, S., Sikora, J. & Somersalo, E. Anisotropic effects in highly scattering media. *Phys. Rev. E* **68** (2003).

61. Johnson, P. M., Faez, S. & Lagendijk, A. Full characterization of anisotropic diffuse light. *Opt. Express* **16** (2008).

62. Patrick M. Johnson, A. L. Optical anisotropic diffusion: new model systems and theoretical modeling. *Journal of Biomedical Optics* **14** (2009).

63. Alerstam, E. Anisotropic diffusive transport: Connecting microscopic scattering and macroscopic transport properties. *Phys. Rev. E* **89** (2014).

64. Sapienza, R., Mujumdar, S., Cheung, C., Yodh, A. G. & Wiersma, D. Anisotropic Weak Localization of Light. *Physical Review Letters* **92** (2004).

65. Bret, B. P. J. & Lagendijk, A. Anisotropic enhanced backscattering induced by anisotropic diffusion. *Physical Review E* **70** (2004).

66. Wiersma, D. S., Muzzi, A., Colocci, M. & Righini, R. Time-Resolved Anisotropic Multiple Light Scattering in Nematic Liquid Crystals. *Physical Review Letters* **83** (1999).

67. Curry, N., Bondareff, P., Leclercq, M. & Van Hulst, N. F. Direct determination of diffusion properties of random media from speckle contrast. *Optics Express* (2011).

68. Scheffold, F. & Block, I. D. Rapid high resolution imaging of diffusive properties in turbid media. *Optics express* **20** (2012).

69. Van Albada, M. P. & Lagendijk, A. Observation of Weak Localization of Light in a Random Medium. *Physical Review Letters* **55** (1985).

70. Wolf, P.-E. & Maret, G. Weak Localization and Coherent Backscattering of Photons in Disordered Media. *Physical Review Letters* **55** (1985).

71. Akkermans, E., Wolf, P. E. & Maynard, R. Coherent Backscattering of Light by Disordered Media: Analysis of the Peak Line Shape. *Physical Review Letters* **56** (1986).

72. Erbacher, F. A., Lenke, R. & Maret, G. Multiple Light Scattering in Magneto-optically Active Media. *EPL (Europhysics Letters)* **21** (1993).

73. Van der Mark, M. B., van Albada, M. P. & Lagendijk, A. Light scattering in strongly scattering media: Multiple scattering and weak localization. *Physical Review B* **37** (1988).

74. Lambert, J. H. *Photometria, sive De mensura et gradibus luminus, colorum et umbrae* (Eberhardi Klett, 1760).

75. Wiersma, D. S. *Light in strongly scattering and amplifying random media* (PhD Thesis, University of Amsterdam, 1995).

76. Anderson, P. W. The question of classical localization A theory of white paint? *Philosophical Magazine B* **52** (1985).

77. Lagendijk, A., van Tiggelen, B. & Wiersma, D. S. Fifty years of Anderson localization. *Physics Today* **62** (2009).

78. Skipetrov, S. E. & Page, J. H. Red light for Anderson localization. *New Journal of Physics* **18** (2016).

79. Scheffold, F., Lenke, R., Tweer, R. & Maret, G. Localization or classical diffusion of light? *Nature* **398** (1999).

80. Wiersma, D. S., Rivas, J. G., Bartolini, P., Lagendijk, A. & Righini, R. Localization or classical diffusion of light? *Nature* **398** (1999).

81. Van der Beek, T., Barthelemy, P., Johnson, P. M., Wiersma, D. S. & Lagendijk, A. Light transport through disordered layers of dense gallium arsenide submicron particles. *Phys. Rev. B* **85** (2012).

82. Etemad, S., Thompson, R. & Andrejco, M. J. Weak Localization of Photons: Universal Fluctuations and Ensemble Averaging. *Physical Review Letters* **57** (1986).

83. Muskens, O. L. & Lagendijk, A. Method for broadband spectroscopy of light transport through opaque scattering media. *Optics Letters* **34** (2009).

84. Mishchenko, M. I. Enhanced backscattering of polarized light from discrete random media: calculations in exactly the backscattering direction. *JOSA A* **9** (1992).

85. Radosevich, A. J., Rogers, J. D., Turzhitsky, V., Mutyal, N. N., Yi, J., Roy, H. K. & Backman, V. Polarized Enhanced Backscattering Spectroscopy for Characterization of Biological Tissues at Subdiffusion Length Scales. *IEEE Journal of Selected Topics in Quantum Electronics* **18** (2013).

86. Lagendijk, A., Vreeker, R. & De Vries, P. Influence of internal reflection on diffusive transport in strongly scattering media. *Physics letters A* **136** (1989).

87. Contini, D., Martelli, F. & Zaccanti, G. Photon migration through a turbid slab described by a model based on diffusion approximation. I. Theory. *Applied Optics* **36** (1997).

88. James, F. Monte Carlo theory and practice. *Reports on Progress in Physics* **43** (1980).

89. Heino, J., Arridge, S., Sikora, J. & Somersalo, E. Anisotropic effects in highly scattering media. *Phys. Rev. E* **68** (2003).

90. Kienle, A., Forster, F. K. & Hibst, R. Anisotropy of light propagation in biological tissue. *Opt. Lett.* **29** (2004).

91. Kienle, A. Anisotropic Light Diffusion: An Oxymoron? *Phys. Rev. Lett.* **98** (2007).

92. Schäfer, J. & Kienle, A. Scattering of light by multiple dielectric cylinders: comparison of radiative transfer and Maxwell theory. *Opt. Lett.* **33** (2008).

93. Kienle, A., Foschum, F. & Hohmann, A. Light propagation in structural anisotropic media in the steady-state and time domains. *Physics in medicine and biology* **58** (2013).

94. Kienle, A., D'Andrea, C., Foschum, F., Taroni, P. & Pifferi, A. Light propagation in dry and wet softwood. *Opt. Express* **16** (2008).

95. Krauter, P., Zoller, C. & Kienle, A. Double anisotropic coherent backscattering of light. *Opt. Lett.* **43** (2018).

96. Weisstein, E. W. *Sphere Point Picking* `http://mathworld.wolfram.com/SpherePointPicking.html`.

97. Marsaglia, G. Choosing a Point from the Surface of a Sphere. *Ann. Math. Stat.* **43** (1972).

98. Gillies, S. *Shapely: manipulation and analysis of geometric objects* toblerity.org. `https://github.com/Toblerity/Shapely`.

99. Yee, K. Numerical solution of initial boundary value problems involving maxwell's equations in isotropic media. *IEEE Transactions on Antennas and Propagation* **14** (1966).

100. Jacucci, G., Onelli, O. D., De Luca, A., Bertolotti, J., Sapienza, R. & Vignolini, S. Coherent backscattering of light by an anisotropic biological network. *Interface focus* **9** (2019).

101. Luke, S. M., Hallam, B. T. & Vukusic, P. Structural optimization for broadband scattering in several ultra-thin white beetle scales. *Applied Optics* **49** (2010).

102. Pattelli, L., Savo, R., Burresi, M. & Wiersma, D. S. Spatio-temporal visualization of light transport in complex photonic structures. *Light: Science &Amp; Applications* **5** (2016).

103. Bret, B. P. J. & Lagendijk, A. Anisotropic enhanced backscattering induced by anisotropic diffusion. *Physical Review E* **70** (2004).

104. Muskens, O. L., Diedenhofen, S. L., Kaas, B. C., Algra, R. E., Bakkers, E. P. A. M., Gómez Rivas, J. & Lagendijk, A. Large Photonic Strength of Highly Tunable Resonant Nanowire Materials. *Nano Letters* **9** (2009).

105. Labeyrie, G., Delande, D., Müller, C. A., Miniatura, C. & Kaiser, R. Coherent backscattering of light by an inhomogeneous cloud of cold atoms. *Phys. Rev. A* **67** (2003).

106. Wilkowski, D. *et al.* Coherent backscattering of light by resonant atomic dipole transitions. *J. Opt. Soc. Am. B* **21** (2004).

107. Jacucci, G., Bertolotti, J. & Vignolini, S. Role of Anisotropy and Refractive Index in Scattering and Whiteness Optimization. *Advanced Optical Materials* **7** (2019).

108. De Gennes, P. G. & Prost, J. *The Physics of Liquid Crystals* (Oxford University Press, 1995).

109. Burg, S. L. *et al.* Liquid-liquid phase separation morphologies in ultra-white beetle scales and a synthetic equivalent. *Communications Chemistry* (2019).

110. Pattelli, L., Egel, A., Lemmer, U. & Wiersma, D. Role of packing density and spatial correlations in strongly scattering 3D systems. *Optica* **5** (2018).

111. Pendry, J. Symmetry and transport of waves in one-dimensional disordered systems. *Advances in Physics* **43** (1994).

112. Berry, M. & Klein, S. Transparent mirrors: rays, waves and localization. *Eur. J. Phys.* **18** (1996).

113. Hottel, H., Sarofim, A., Dalzell, W. & Vasalos, I. Optical properties of coatings. Effect of pigment concentration. *AIAA J.* **9** (1971).

114. McNeil, L. & French, R. Multiple scattering from rutile TiO_2 particles. *Acta Mater* **48** (2000).

115. Elton, N. & Legrix, A. Spatial point statistics for quantifying TiO2 distribution in paint. *J. Coat. Technol. Res.* **11** (2014).

116. Schertel, L., Wimmer, I., Besirske, P., Aegerter, C. M., Maret, G., Polarz, S. & Aubry, G. J. Tunable high-index photonic glasses. *Phys. Rev. Materials* **3** (2019).

117. Syurik, J., Jacucci, G., Onelli, O. D., Hölscher, H. & Vignolini, S. Bio-inspired Highly Scattering Networks via Polymer Phase Separation. *Advanced Functional Materials* **28** (2018).

118. Wilts, B. D. Nature's functional nanomaterials: Growth or self-assembly? *MRS Bulletin* **44** (2019).

119. De France, K. J., Hoare, T. & Cranston, E. D. Review of Hydrogels and Aerogels Containing Nanocellulose. *Chemistry of Materials* **29** (2017).

120. Mulder, M. *Basic Principles of Membrane Technology* (Springer Science & Business Media, 2012).

121. Daraboina, N. & Madras, G. Kinetics of the ultrasonic degradation of poly (alkyl methacrylates). *Ultrasonics Sonochemistry* **16** (2009).

122. Tan, B., Melius, P. & Ziegler, P. A Simple Gas Chromatographic Method for the Study of Organic Solvents: Moisture Analysis, Hygroscopicity, and Evaporation. *Journal of Chromatographic Science* **20** (1982).

123. Caixeiro, S., Peruzzo, M. & Onelli, O. D. Disordered Cellulose-Based Nanostructures for Enhanced Light Scattering. *ACS Applied Materials & Interfaces* **9** (2017).

124. Parker, R. M., Guidetti, G., Williams, C. A., Zhao, T., Narkevicius, A., Vignolini, S. & Frka-Petesic, B. The Self-Assembly of Cellulose Nanocrystals: Hierarchical Design of Visual Appearance. *Advanced Materials* **30** (2018).

125. Habibi, Y., Lucia, L. A. & Rojas, O. J. Cellulose Nanocrystals: Chemistry, Self-Assembly, and Applications. *Chemical Reviews* **110** (2010).

126. Erlandsson, J., Pettersson, T., Ingverud, T., Granberg, H., Larsson, P. A., Malkoch, M. & Wågberg, L. On the mechanism behind freezing-induced chemical crosslinking in ice-templated cellulose nanofibril aerogels. *J. Mater. Chem. A* **6** (2018).

127. Parker, R. M., Frka-Petesic, B., Guidetti, G., Kamita, G., Consani, G., Abell, C. & Vignolini, S. Hierarchical Self-Assembly of Cellulose Nanocrystals in a Confined Geometry. *ACS Nano* **10** (2016).

128. Joiner, A., Hopkinson, I., Deng, Y. & Westland, S. A review of tooth colour and whiteness. *Journal of Dentistry* **36** (2008).

129. Patil, P. *CIE Coordinate Calculator* `https://uk.mathworks.com/matlabcentral/fileexchange/29620-cie-coordinate-calculator`.

I would like to dedicate
To the scar on my face
All the stars of the globe
The world is yours, Scarface.

— Rakim Mayers

ACKNOWLEDGMENTS

And yes, this is the very end of this journey. The first acknowledgment goes to you that were brave enough to read throughout all my thesis (assuming that you didn't simply use the hyperlink in the ToC).

Conversely to what you might expect to find, these acknowledgments won't - well, almost never - explicitly mention names. I have huge esteem of all the people involved, and I'm sure they will read between the lines.

An enormous thanks go to my supervisor, for trusting me since day zero and for keeping me always motivated. Thank you for all the precious help and suggestions you gave me and for introducing me to amazing scientists and people! This gratitude extends to all the present, past, and honorary members of the BIP group: you made my work lighter and orders of magnitude funnier.

I am grateful to the people that I met more than four years ago when I first moved to Cambridge. I was partly reluctant and scared to move abroad, but you made me feel at home. You will always have a special place in my heart as that legendary Cambridge mug has one on my shelf.

I was fortunate that when our paths diverged, I found a fantastic group of people that defused my sadness and warmly embraced my ENTJ personality. We shared a lot together, and I felt blessed for having had you on my side these years.

Football is an essential part of my life. I was/am grateful to be part of the THFC. We shared the same love for football that held us together through difficult and glorious Sundays. Thank you for welcoming me in this glorious team - to captain you was a huge honour for me.

This acknowledgment naturally extends to my beloved As Roma Club Cambridge. Thanks for all the laughs, hugs, and screams that made every disappointment more bearable.

A huge thanks go to those who have always been part of my life. I am proud of having chosen you as my brothers. When I'm with you, I feel like time has stood still.

The next one goes to my family for all the support and unconditional love you gave me: thank you for believing in me! A special thanks go to my niece for teaching me that the beauty of life is in the small things.

The last, dulcis in fundo, is for you. For making all the tints of my life brighter.